IMPACT OF MICROHEMORRHAGES ON BRAIN CELL FUNCTION

A Dissertation

Presented to the Faculty of the Graduate School

of Cornell University

in Partial Fulfillment of the Requirements for the Degree of

Doctor of Philosophy

by

Flor A. Cianchetti

January 2012

© 2012 Flor A. Cianchetti
ALL RIGHTS RESERVED

IMPACT OF MICROHEMORRHAGES ON BRAIN CELL FUNCTION

Flor A. Cianchetti, Ph.D.

Cornell University 2012

A stroke is defined as abnormal brain functionality due to a disruption in the blood supply produced by a hemorrhage or clot. They can be classified as symptomatic or asymptomatic. In this dissertation I imaged deep into the brains of live rodents using two-photon excited fluorescence microscopy to study hemorrhagic asymptomatic strokes. We focused high-energy lasers on the surface of a particular blood vessel to rupture its endothelium to cause bleeding. The damage was only confined to the focus of the laser ($\sim$1 μm^2). Employing these methods, we investigated two issues that could advance stroke treatments. First, we evaluated the use of blood breaking drugs or anticoagulants on the effect of hemorrhage size. We examined tissue plasminogen activator (tPA), the only FDA approved drug to dissolve blood clots, and the following anticoagulants: dabigatran etexilate (DE), warfarin and heparin. We found that DE and tPA treated mice developed hemorrhages of comparable size than control mice (treated with saline). In contrast, mice treated with warfarin and heparin (anticoagulants) developed larger hemorrhages. It is relevant to characterize the size of brain hemorrhages since it correlates with patient prognosis. The study suggests that tPA and DE do not exacerbate damage from hemorrhaging and they present a lower risk for bleeding complications when compared to warfarin and heparin. In the second part of this dissertation, we analyzed neuronal activity around microhemorrhages to characterize the resulting region of damage. We compared calcium transient responses to a peripheral stimulus from cortical neurons and neuropil. We found that calcium transient responses

obtained after a microhemorrhage were inhibited or had smaller amplitudes than responses obtained before microhemorrhage induction. In addition, the amplitude of the responses is correlated with the distance from the edge of the hemorrhage. Furthermore, calcium transient responses improved over four hours after a hemorrhage, returning to normal responses (i.e. comparable to control experiments) one day after initial onset. This dissertation provides a better understanding of microhemorrhage pathophysiology.

BIOGRAPHICAL SKETCH

Some how, God let me be part of a very stable family, in which work and a spiritual upbringing were the daily tonic to achieve long and short time goals. Ever since I can remember I have been fascinated by the human body and its extreme complexity. Having the opportunities of free education and a supportive family, I pursued two undergraduate degrees simultaneously, one in Bionics Engineering an another one in Chemical engineering at Instituto Politcnico Nacional and Universidad Autonoma Metropolitana, respectively, in Mexico city. After participating in projects studying muscle fatigue and epileptic seizures, I became particularly interested in the nervous system and signal processing. I worked as a programmer in Dendrite Inc. for a year, then I joined the Ph.D. program in Biomedical Engineering at Cornell University.

During my first two years I worked for the Neuromuscular Biomechanics Laboratory under the supervision of Francisco Valero-Cuevas in the area of manipulation and interpretation of the neurological signals that control hand function. Francisco left Cornell and I was too attached to Ithaca to follow, so I joined Chris Schaffer's laboratory where I performed in vivo experiments to characterize damage cause by a brain hemorrhage on neurons. I believe that in order to develop further insight into curing many disorders that people commonly suffer from today, we need to gain a better understanding of how the brain functions.

I finished my PhD at the end of 2011 and moved to Portland, Oregon.

To Laura and Daniel,

the hardest part of this journey was to be far away from you.

ACKNOWLEDGEMENTS

I have to admit that the idea of getting a PhD originally did not come from me. I did not know what it meant to get a doctorate degree or that you could even apply for one without having a master degree first until my dad suggested it. Of course, you always doubt your parents word because for every parent their child is a star. One of my professors at my university, Hector Javier verified what my dad told me and he encouraged me to pursue the idea. I contacted different laboratories where I wanted to work, but none of them felt as supportive and challenging as the lab of Francisco Valero-Cuevas, my first advisor, who believed in me and significantly contributed to my professional development. We had two very productive years of work.

Later, I became part of the Schaffer lab where Chris was great guiding me and keeping me interested in my projects. He is very understanding, smart and fun. He always showed confidence in my skills and interest in my work. Marjolein van der Meulen and Christiane Linster formed part of my thesis committee, they provided me with insightful comments to this project and a detailed review of this dissertation. They are a great example of successful women scientists that are very happy with their life/career choices. The Schaffer lab members were very friendly and helpful. Nozomi, John, Nate, Matt, Puifai, Liz, Poornima and Catherine were always ready to discuss my research topics and they provided comments for this dissertation. Nozomi, John and Nate passed me all their tips on how to do a perfect surgery, set up the two-photon microscope and troubleshoot problems with my experiments. During the last year, I worked with DK and Sally, together we spent good and stressful times. They were full of enthusiasm and they were key elements for my project.

Even though I was far away from home, I always felt all the love from my parents, Norberto and Guadalupe, and siblings, Beto, Dulce, Alex, Laura and Daniel. Daniel helped me with the creation of figures and Laura organizing references for this dissertation. During the past 6 years my parents followed each of my steps and kept me in their prayers, I cannot describe how valuable their help has been throughout my career and specifically when they came to Ithaca. Good friends in Mexico and in the U.S. have also been with me, filling my days with fun, adventures and extra help.

My life changed when I met Mark, long winters and big problems stopped mattering as much to me since we had each other. He helped me correct my writing, presentations and we even engaged in long discussions about how the brain works.

For the mentioned reasons and many others, I am in debt with all these people and I want to give them thanks from the bottom of my heart. Thanks for being an important part of my life.

TABLE OF CONTENTS

LIST OF FIGURES

CHAPTER 1

INTRODUCTION AND ORGANIZATION

In recent years, there has been increased recognition of the heavy toll of strokes on humans. While the consequences from large strokes are well defined, in part because they have high mortality and morbidity rates, less studies exist about strokes of smaller size. This type does not present obvious symptomatology and their impact on human health remains controversial. Strokes can be caused by the rupture of (hemorrhagic stroke) or by an occlusion of (ischemic stroke) a brain vessel.

In this dissertation I studied hemorrhagic strokes, with emphasis on microhemorrhages. I put together current knowledge on brain microhemorrhages, adding findings from my experimental work and interpretations. The main objective of this work is to understand damage caused to human health by these lesions with the end goal of improving treatments. Using an animal model to create hemorrhages, I discerned two main questions. First, whether or not most common used thrombolytic drugs and anticoagulants induce larger brain hemorrhages. Second, whether small hemorrhages damage neural function, and to what extent.

Chapter 2 begins with an explanation of the techniques I used to study microhemorrhages. Using calcium imaging together with two-photon excited fluorescence microscopy (2PEF) I was able to look at neuronal function in live animals. To induce hemorrhages on the brain of rodents, I used femtosecond laser pulses on the vessel wall.

Chapter 3 is a compilation of literature reviews on intracerebral hemorrhage with an emphasis on microhemorrhage. Topics include the definition of microhemorrhages and how they are detected clinically, current models used to study microhemorrhages, activated molecular pathways after hemorrhages, summary of

results from experiments finding cellular damage by hemorrhages and finally association of microhemorrhages in patients with neurological deficits.

Chapter 4 describes experimental work done to characterize the size of hemorrhages induced on mice when they were treated with the following drugs: tissue plasminogen activator, dabigatran etixilate, heparin and warfarin. This chapter contains my work from a collaboration resulting in two manuscripts submitted to peer-reviewed journals.

Chapter 5 contains the results of experiments using live rodents, fluorescent dyes and multiphoton microscopy to characterizes neuronal damage after laser-induced microhemorrhages. I quantifed the response of neurons to a peripheral stimulus and compared the neural responses before and after a microhemorrhage was induced. Acute and chronic experiments were performed to assess where and when neurons recover their ability to respond properly to stimulation.

Chapter 6 describes work done during my first two years in the Ph.D program characterizing electromiographical signals from the index finger muscles during force and movement production in humans. The nervous system uses different strategies to control force and movement. A model is presented to describe the transition between these two strategies. This research was originally published in the Journal of Neurophisiology.

The last chapter is a brief summary of the results presented throughout the dissertation, pointing out future areas of research.

CHAPTER 2

TECHNIQUES

2.1 Calcium Imaging

Examining changes of free calcium ions (Ca^{2+}) in the intracellular concentration of neurons is an alternative to the conventional method which records action potentials with electrodes to study neural activity. When calcium changes expressed as changes in fluorescence and electric activity are monitored simultaneously on neurons, it has been demonstrated that calcium spikes follow very closely to each of the action potentials (figure 2.1) [25, 51, 181, 182]. This section reviews the calcium imaging technique using fluorescent calcium indicators [144].

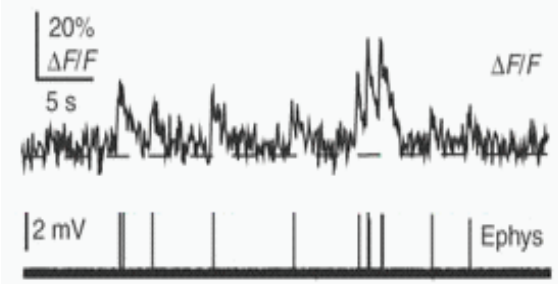

Figure 2.1: Calcium changes correlate with action potentials, adapted from [51].

2.1.1 Advantages and Applications

The main advantage of calcium imaging is that it allows for monitoring of neural activity from multiple cells at the same time with minimal or no disruption of the cell membrane. However, the challenge in calcium imaging is to achieve a reasonable signal to noise ratio and temporal resolution, which mainly depend on the hardware used to excite and record fluorescence. The use of calcium imaging on biological experiments has become widely adopted and it is a valuable tool to study topics such as neuronal networks [30, 42, 43, 78, 113, 140], learning and memory [31, 35, 45, 143], development and death of neurons [93, 106, 128], cells under pathological conditions [28, 32, 164], etc. In this work we used calcium

imaging to study neural response before and after cortical micro-hemorrhages.

2.1.2 Calcium Dynamics in Neurons

When neurons are at rest they have a membrane potential of -60 mV and a low intracellular Ca^{2+} concentration of $\sim$0.1 μM. There is a high Ca^{2+} concetration gradient across neuron cell membranes because the extracellular Ca^{2+} concentration is 1-2 mM [3].

During an action potential, the electrical depolarization of the cell membrane causes voltage-dependent calcium-selective ion channels to open [142], and the cytosolic Ca^{2+} concentration increases to levels of 1 μM or more. Calcium is either sequestered (by the reticulum endoplasmatic, mitochondria, nucleous) or interacts with binding proteins (calmodulin, phospolipades, krumaffin, K^+ channels, and others) inside the cell [4]. Upon binding to proteins that function as receptors on vesicles filled with neurotransmiters, Ca^{2+} signals for protein conformations that will enable the fusing of the vesicles to the presynaptic membrane to deliver their content (neurotransmitters) into the synaptic cleft [61]. The amount of neurotransmitter released is proportional to the number of open calcium channels that occurs within 200 μs of the action potential arriving at the synaptic terminal [135]. Voltage calcium channels are closed at the end of the action potential, and calcium ions left inside the cell return to the extracellular space through the Ca^{2+}-ATPase pump of the cell membrane or by the sodium-calcium exchanger [29, 75]. Figure 2.2 illustrates the simplified steps that occur during the synapses between two neurons.

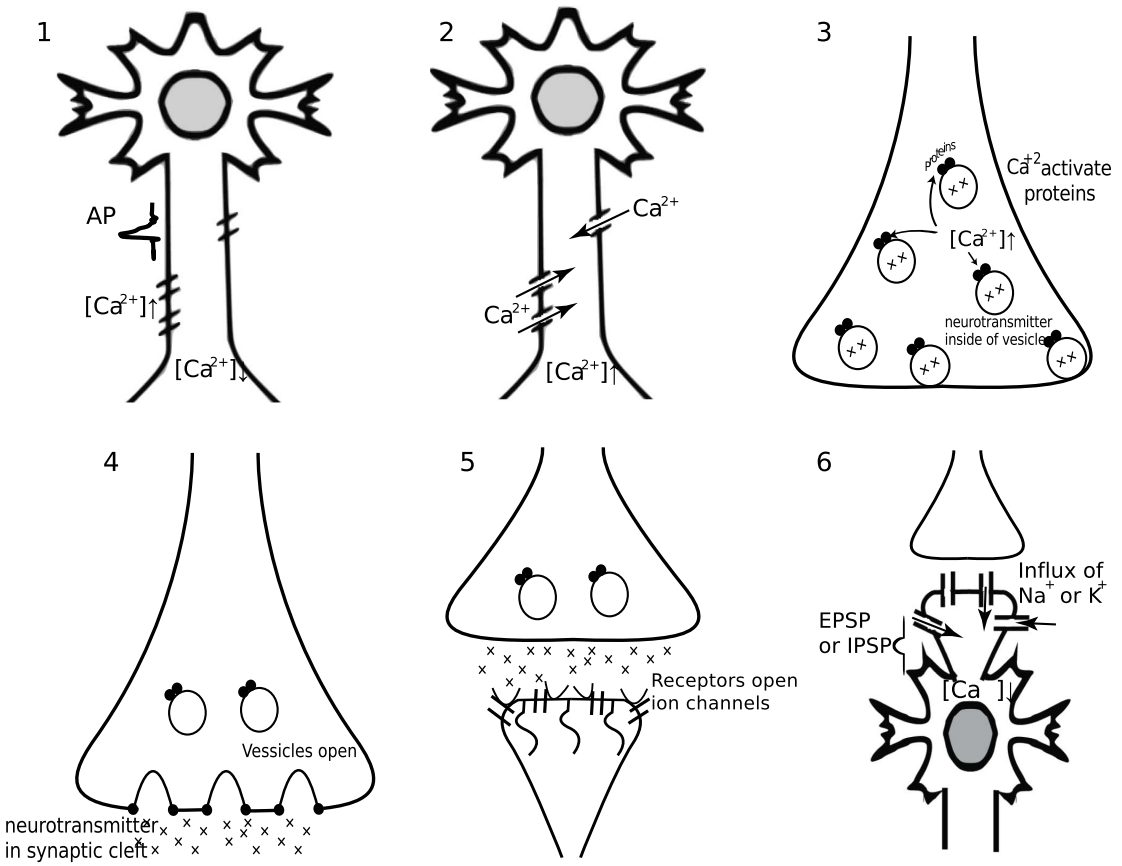

Figure 2.2: Neuronal synapses. 1) Action potential leads to the opening of the calcium channels. 2) Calcium ions rush into the cell. 3) Proteins that enable docking of vesicle get activated with Calcium. 4) Vesicles open, and neurotransmitter is released into the synaptic cleft. 5) Neurotransmitter binds to receptors in postsynaptic neuron or is reabsorbed by presynaptic neuron. 6) Receptors open ion channels resulting in an excitatory or inhibitory postsynaptic potential (EPSP or IPSP).

2.1.3 Types of Dyes

Fluorescent calcium dyes, act as calcium buffers and their emission spectrum are dependent on the calcium concentration of the media (i.e., their fluorescence properties will change when bound to Ca^{2+}). Calcium dyes are able to detect intracellular free calcium ion concentration between the range of <50 nM to >50 μM [114]. They have an EGTA (ethylene glycol tetraacetic acid) or BAPTA (1,2-bis(o-aminophenoxy)ethane-N,N,N',N'-tetraacetic acid) structure (figure 2.3), which will give the high affinity to Ca^{2+} [118].

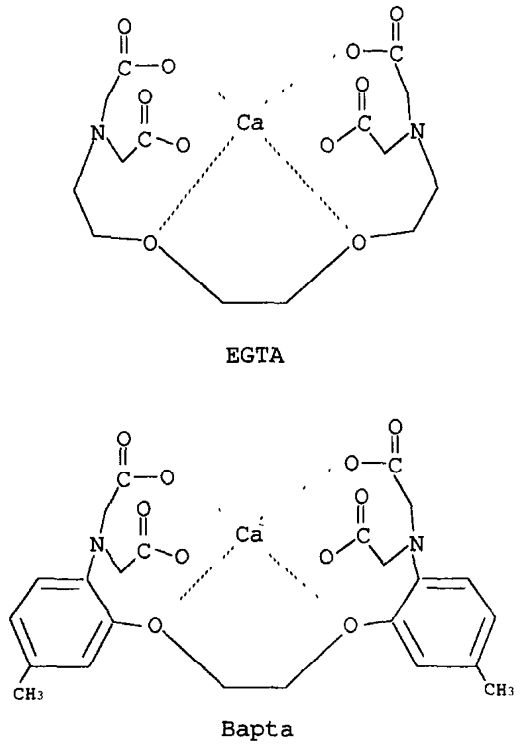

Figure 2.3: The structure of EGTA and BAPTA, taken from [118].

Fluorescent Ca^{2+} dyes are commonly prepared in the form of salts, dextran conjugates or acetoxymethyl (AM) esters [114]. When in the form of salts or dextran conjugates, they need to be deposited directly into the cell membrane by loading methods such as electroporation or intracelullar injections. In contrast, calcium dyes in AM ester form can cross the cell membrane, therefore they need to be loaded in the extracellular space (bulk-loading labeling). This is achieved by injections into the brain of an animal when in-vivo labeling of neurons is desired. Bulk-loading in the extracellular space results in the labeling of multiple cells ($\sim$500 μm^2 area). In this work, a calcium dye in AM ester form, Oregon Green Bapta (OGB), is used. In general, AM ester calcium dyes need to be mixed in a 20% solution of Pluronic F-127 with anhydrous dimethylsulfoxide (DMSO) and further diluted in physiological media to enable permeability into the cell membrane (see details about OGB preparation in the appendix). DMSO prevents the AM ester

from being hydrolyzed until it is in the cytoplasm. Pluronic F-127, a dispersing agent, increases OGB solubility in the physiological media [114, 144].

Calcium dyes in AM ester form are permeable to cell membrane and once inside the cell, the AM groups from the dye bind to intracellular enzymes (esterases) resulting in free dye which is impermeable to membrane and is able to bind to free Ca^{2+} from the cytoplasm. Other products such as formaldehyde and acetate may also be formed in this process (figure 2.4) [52, 147, 118].

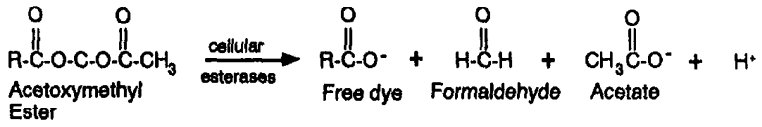

Figure 2.4: Inside the cell, acetoxymethyl esters are cleaved to cellular esterases, taken from [118].

Calcium indicators can be classified into either single wavelength or ratiometric dyes. Ratiometric dyes shift their excitation or emission spectra when bound to calcium (e.g., Fluo3, Calcium Green 1). Single wavelength dyes increase fluorescence intensity without changing wavelength (e.g., Indo1, Fura2). The type of indicator may depend on the length of the experiment and whether total calcium concentrations or changes in the concentrations need to be quantified. Photobleaching, uneven loading and dye hidrolysis are common problems associated with calcium imaging using fluorescent dyes. These problems need to be considered especially when looking at total calcium concentrations where the use of ratiometic dyes is more recommended [114]. Single wavelength dyes allow for a simpler microscope design and the simultaneous use of more fluorescent dyes.

In this work, we examined calcium transients with changes in fluorescence with respect to a baseline (dF/Fo) and compared them to the same cell at different time intervals, thus controlling for uneven dye loading. In addition, photobleaching is limited since we used two-photon excited microscopy(2PEF). The type of dye

chosen was Oregon Green Bapta (OGB), a non-ratiometric dye.

2.1.4 Genetically Encoded Calcium Indicators

Recently, calcium indicators were able to be introduced by gene transfer techniques into live organisms resulting in the fluorescent labeling of intracellular calcium. These types of indicators facilitate long term calcium measurements because they do not metabolize over time and the loading phase is absent. They combine proteins with high affinity to calcium such as Calmodulin or Troponin C with fluorescent proteins [41].

Genetically encoded calcium indicators are being successfully used to image small animals such as worms, fruitflies, zebrafish, and brain sections, however they are not as efficient as the calcium dyes when imaging neurons inside brains of larger animals. Hasan et al. [56] achieved steady expression of flash pericam, IP, CaMP, Cg2, and cameleons indicators in neurons of mice over 12 weeks. Heider et al., [58] recorded activity from the visual cortex of monkeys over a period of 10 months.

Genetically encoded indicators have some flaws, namely;

1. They are not able to detect action potentials with precision [96, 41].
2. They are not bright enough, providing a low signal to noise ratio.
3. The amplitude of the calcium transients *in vivo* are smaller (by a half or more) than the amplitude of calcium transients produced with calcium dyes under the same conditions or *in situ* [167].
4. They can be affected by temperature changes [96].
5. Fluorescent proteins may become nonresponsive [63].

Figure 2.5 shows two regions of the visual cortex of mice where cells were labeled with either OGB-1 (ester dye) or TN-XXL (genetically encoded indicator). Similar

calcium responses to visual stimuli were obtained but neurons labeled with OGB-1 were brighter and had larger amplitudes in their responses [95].

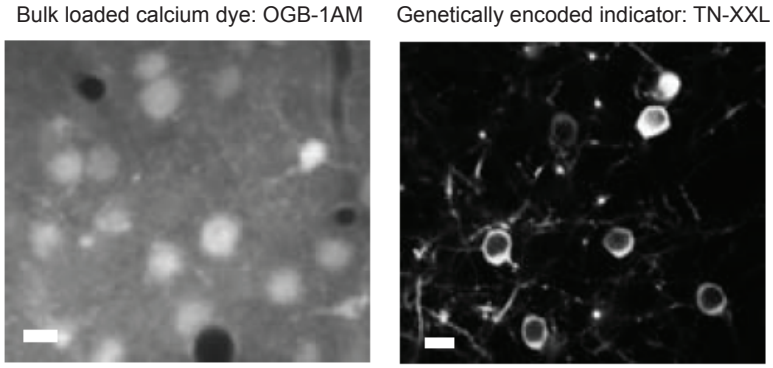

Figure 2.5: Visual cortex of mice where cells were labeled using OGB-1 AM calcium dye or the calcium indicator (TN-XXL) was genetically encoded into the cells, scale bar=10μm, adapted from [95].

Given the above limitations of genetically encoded indicators and the importance to measure the amplitude of calcium transients in the project, we could not employ this technique. Improvement of genetically encoded indicators will enable a simplified way of monitoring neuronal activity in a non-invasive way, and it may be able to replace calcium dyes in the near future.

2.2 Multiphoton Microscopy

Multiphoton microscopy (MPM) is widely used to image deep inside live animals or tissue with submicrometer and millisecond time resolution, non-invasively [186]. In this dissertation I used MPM, in particular two-photon excited fluorescence microscopy to image cells and vasculatory in the cortex of rodents reaching a maximum depth of 300 μm.

2.2.1 Principles of Nonlinear Microscopy

Molecules and atoms may transition from their ground state to an excited state when they absorb enough energy in the form of light for one of the electrons to move to an orbital of higher energy. When the molecule or atom returns to its ground state, it can lose the acquired energy through internal conversion, heat, light or a combination. Molecules that emit light when they return to ground state are known as fluorophores. Emitted photons have less energy than absorbed photons.

Commonly, fluorophores are introduced inside live animals to label structures of interest, however they can also be encountered naturally in some cells. With the use of spectral filters we can use different fluorophores simultaneously to be able to distinguish the light emitted by each of them.

The minimum energy that enables the transition of an electron to a higher electronic excited state (to generate fluorescence) depends on the particular fluorophore, this energy can be given by a single or by multiple photons. The energy of a photon is inversely proportional to its wavelength ($\mathrm{E} = \frac{hc}{\lambda}$, where h is Plancks constant and c and λ are the speed and wavelength of light in vacuum, respectively). Thus, multiple photons of longer wavelengths can provide the same amount of energy as a single photon of shorter wavelength.

In two-photon microscopy, the energy from two photons must be transferred to an electron in a single quantized event (within an interval of about $10E^{-18}$seconds) to bring the molecule to an excited state, see figure 2.6B. The probability of two-photon absorption increases with the square energy of the incident light and only occurs in a high photon density medium. Therefore, only at the laser focus two or more photons can be absorbed by the same electron almost instantaneously. This non linear absorption process makes possible the imaging of single planes ($\sim$1

μm) with depth [24, 146], in contrast with linear absorption where all fluorophores along the laser beam path get excited and generate fluorescence at all planes, see figure 2.6A.

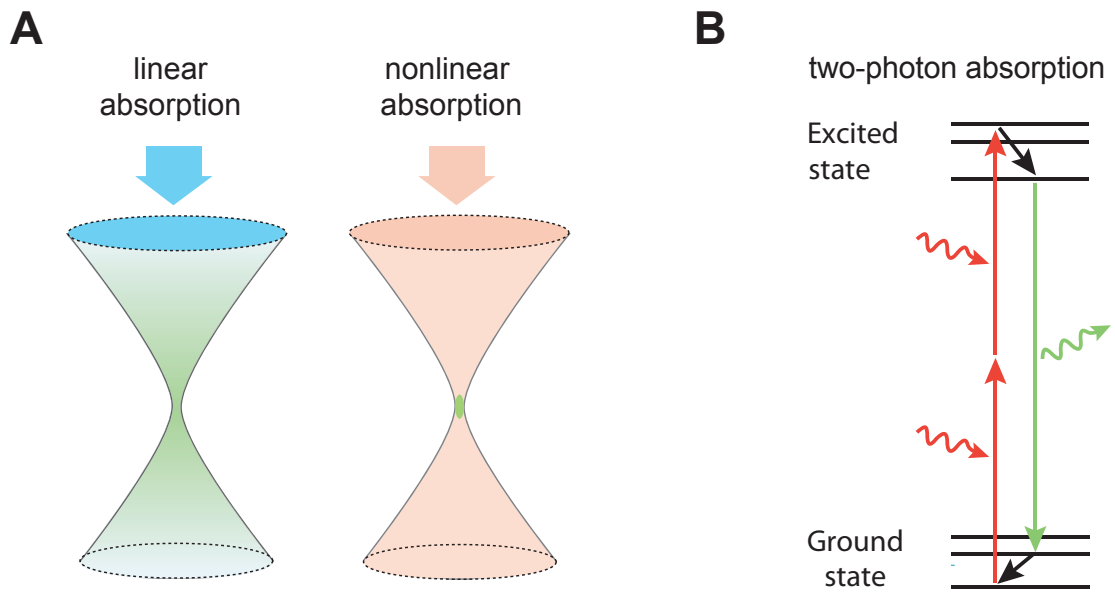

Figure 2.6: Non linear microscopy. A. Linear versus non linear absorption of photons, non linear absorption allows imaging of a single point in a volume. B. Jablonski diagram of two photon absorption by a fluorophore, adapted from [59].

Short pulsed lasers with pulse durations between 50 and 100 fs and high repetition frequency are generally used as the source light for *in vivo* imaging using non-linear microscopy. This procedure reduces thermal damage while providing high peak power and peak intensity with low average power [24]. In this work, we use 100 fs and 300 fs laser pulses with frequencies of 87 MHz and 1 MHz, respectively. The 100 fs pulses are generated by a Ti-sapphire laser which can be tuned from 800 to 900 nm wavelength and the 350 fs pulses by a YB-fiber oscillator/amplifier laser with a fixed wavelength of 1045 nm.

2.2.2 Limitations

The imaging depth into live organisms using two-photon microscopy is limited by the scattering of the excitation and emission light while propagating through the medium. Although excitation photons do not get absorbed by molecules outside the laser focus and longer wavelengths scatter less, excitation light still can get deviated and the number of photons reaching the focus decreases exponentially with depth [44, 138]. Thus, the fluorescence at the focal plane reduces proportionally to the square of the fraction of unscattered excitation photons, $F \sim [P_o exp(-\frac{z}{ls})]^2$ where P_o is the power at the imaging surface and z is the imaging depth [7, 112, 119].

The emitted fluorescence light also scatters, affecting collection efficiency; the amount of scattering depends on imaging depth and field of view. The laser intensity for excitation needs to be optimized to produce maximum fluorescence without saturation, photodamage and photobleaching [25, 81, 66, 115]. In two-photon microscopy, photobleaching and photodamage are limited, permitting longer imaging times as compared to linear microscopy. With current laser powers *in vivo*, two-photon imaging in brain is possible to 1000 μm deep [24, 60, 12].

The use of two-photon imaging can be limited by the existence of fluorophores that target the structures of interest. In addition, some fluorophores may have overlapping emission spectra making it difficult or impossible to distinguish the fluorescence associated with each fluorophore individually.

2.2.3 Two-photon Microscope Design

In a two-photon microscope, the image is formed by detecting the emitted fluorescence when the laser focus is scanned at very fast rates through the sample. Scanning of the laser through the sample is achieved with two mirrors that semiro-

tate. The field of view and image acquisition rate depends, in part, on the degree of rotation of the mirrors and their speeds, respectively. In a conventional two-photon scanning microscope, a trade-off between spatial and temporal resolution exists. Mirrors and lenses are used to resize and guide the laser beam from the laser source to the scanning mirrors and to the back of the objective [146]. A prism compensator may be used to avoid lengthening of the laser pulse, resulting in loss of pulse intensity. Fluorescence from the sample is emitted at all angles and only part of it will be collected by the objective. A high numerical aperture (NA) of the objective improves transmission and collection of light and resolvable distance (R). NA is equal to the refractive index times the sine of half the objective angular aperture (NA=n*sinθ). R depends on NA as R=0.61 $\frac{\lambda}{NA}$ where λ is the illumination wavelength. Fluorescence collected by the objective passes through a dicrohic beam/splitting mirror which blocks the reflected excitation light and separates the fluorescence light. More filters are generally used to further obtain the desired wavelength range. Finally, light from each of the channels pass trough a photomultiplier tube which converts it into voltages. The measured voltages are amplified and digitized. A computer program is used to control the scanning mirrors and to display an image based on the voltages from the photodetector and the position of the mirrors. A schematic of the basic parts of a non-linear microscope is shown in figure 2.7

2.3 Laser Ablation

Non-linear interactions can lead to breakdown of the material that is being irradiated when the energy levels are high enough to cause ionization rather than excitation. Similar to two-photon microscopy, this high energy is achieved only at the focus of an objective, limiting the damage to a single spot of ∼femtoliter

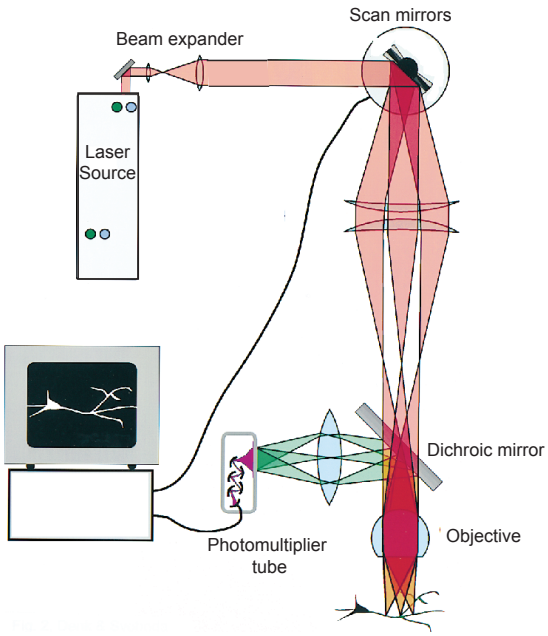

Figure 2.7: Schematic of a multiphoton microscope, adapted from [59].

sized volume (Fig. 2.8). To ionize a molecule, the electrons of the molecule need

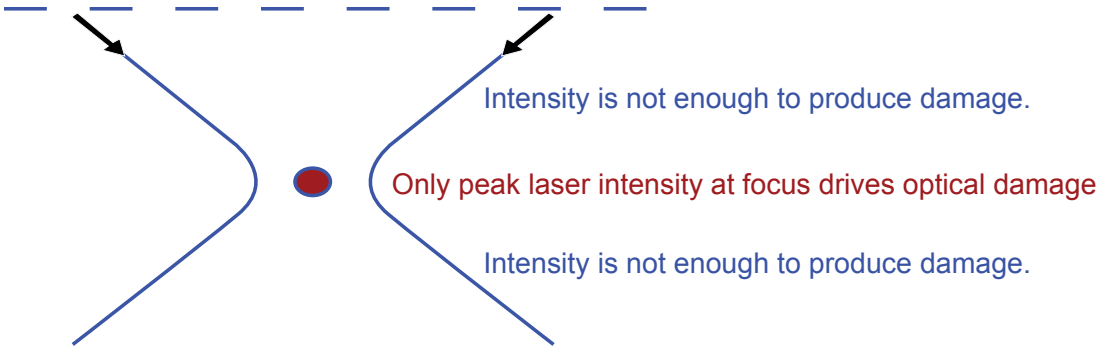

Figure 2.8: Ablation with fs-laser pulses is limited to the laser focus. Outside the focus the energy is below the tissue damage threshold restricting breakout to focus where molecules are ionized.

to be freed from their molecular orbitals, thus the electrons need to receive enough energy to overcome their electron binding energies (mainly bandgap energy) [159]. Photons that have energies less than the band-gap energy may be absorbed or scattered but will not achieve photoionization. In the initial steps of plasma ablation, photoionization occurs via multiphoton absorption or tunnel ionization (interaction

with the electric field of the laser). The electrons that are freed keep increasing their energy by a process known as inverse Bremsstrahlung, in which the electrons absorb photons while colliding with molecules. After several Bremsstrahlung events, the energy of the electrons is high enough to ionize other molecules in ground state by a subsequent collision (impact ionization), resulting in generation of another free electron (the first electron looses some energy but remains free). The electrons undergo the same process repeatedly (Bremsstrahlung and impact ionization) creating an avalanche ionization until all the molecules in the focus are fully ionized (plasma). At the end of the pulse, plasma, free electrons and ionized molecules at the focus recombine and energy from the electrons is transfered to the material resulting in the formation of a cavitation bubble and transformation of the material, see figure 2.9. Sometimes if the cavitation bubble is large, it may extend the damage to the material outside the volume ionized [14, 13, 129, 159].

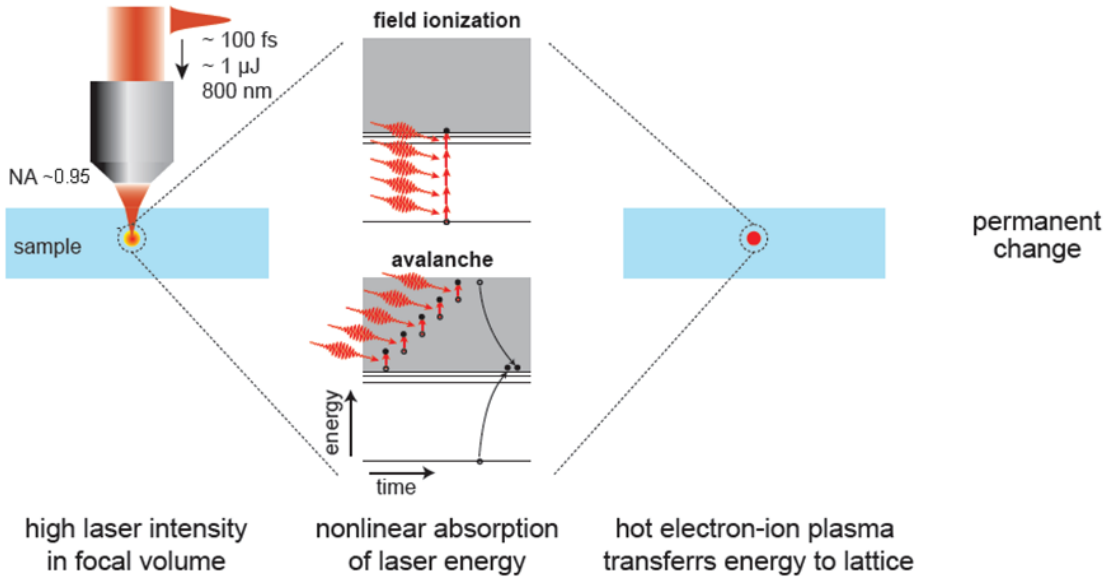

Figure 2.9: Ablation process using high energy femtosecond laser (figure provided by Chris Schaffer)

In the experiments described in this work, similar to [109, 127], we induced laser ablation on brain vessels using 50 fs duration laser pulses at 1 kHz repetition

rate produced by a Ti:Sapphire regenerative amplifier (Legend 1k USP; Coherent), pumped by a Q- switched laser (Evolution 15; Coherent) and seeded by a Ti:Sapphire oscillator (Chinhook; Kapteyn-Murnane Laboratories Inc.) The ablation laser was set up collinearly with the two-photon excitation laser, entering the two-photon microscope after the scan mirrors. This permitted visualization of tissue at the same time that photo disruption is induced.

CHAPTER 3

HEMORRHAGIC STROKE

3.1 Types of Stroke

Strokes can be classified by their cause as either hemorrhagic or ischemic, see figure 3.1, or by their size and symptomatology as either symptomatic (large) or silent (small, <5 mm), see figure 3.2. In the clinical setting, strokes that are small and ischemic are usually referred to as infarcts, while strokes that are small and hemorrhagic are known as microbleeds.

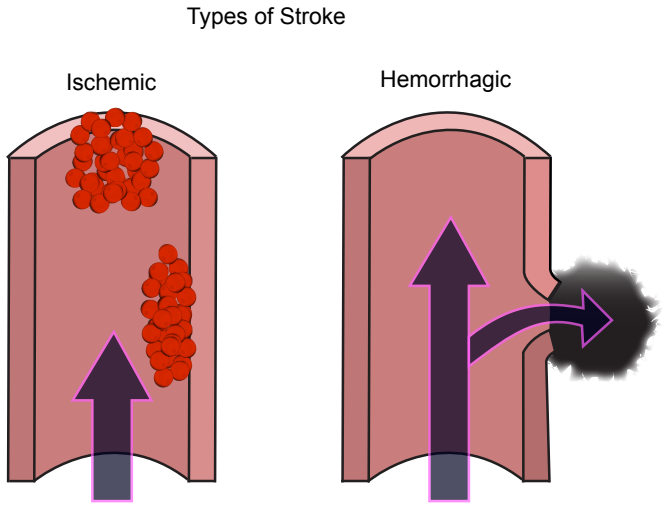

Figure 3.1: Strokes can be either ischemic or hemorrhagic. Ischemic strokes are characterized by a blockage in the blood supply while in hemorrhagic strokes the vessel ruptures and blood spills into the brain.

Hemorrhage location may vary a lot across patients but occurs most commonly in the cortex, subcortex , basal ganglia, thalamus, brain stem, and cerebellum [122]. Some factors have been identified to increase the risk of developing hemorrhages, for example, impaired coagulation, arteriovenous malformation, metatastic tumors, trauma, hypertension, advanced age, cerebral amyloid angiopathy and leukoaraiosis [122]. It has been difficult to distinguish whether some of these factors or hemorrhage locations are associated exclusively to a type of hemorrhage since many clinical studies have found that large hemorrhages sometimes developed in the same location as previous microbleeds [80, 148]. However, repercussions in

human health and mechanisms of injury depend on hemorrhage size.

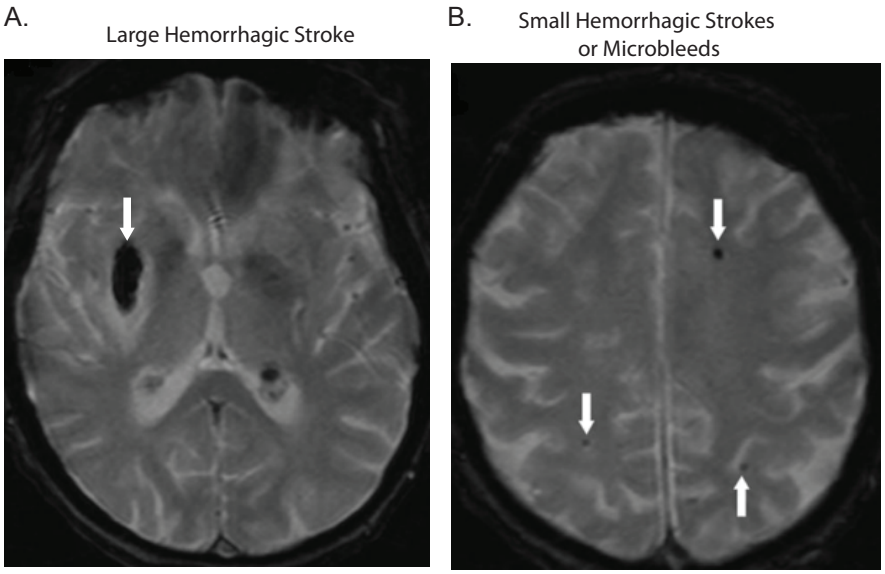

Figure 3.2: MRI of large and small hemorrhages in a 77 year old woman. A.Right putaminal intracerebral hemorrhage. B. Multiple microbleeds in the cortex and subcortex. Figure adapted from [80].

3.2 Symptomatic Hemorrhages (Large)

Symptomatic intracerebral hemorrhages account for 15% of all stroke cases and patients develop symptoms such as confusion, distortion of the speech, paralysis, etc. MRI or CT are usually necessary to differentiate them from ischemic strokes. They have a high index of disability and mortality rate. It is estimated that only 40% of patients survived more than a year after hemorrhage onset [121, 37] and many of the patients remain with motor and behavioral deficits. Figure 3.3 enlists the clinical impact of large hemorrhages on human health.

During a large brain hemorrhage, the intracranial pressure increases, resulting in tissue displacement, compression of the thalamus and brain stem, edema formation, brain herniation and death of the patient [175, 2]. Besides mass effects, other mechanisms of injury are associated with the disruption of the blood brain barrier.

Blood is highly toxic to brain cells; for example, high levels of glutamate from blood in the extracellular medium results in excitotoxicity, lactic acidosis and cell death. Blood components alone have been proven to cause apoptosis and necrosis in neurons (figure 3.6).

Consequence on human health	Type of Hemorrhage (by size)
brain herniation	L
death	L
motor deficits	L
behavioral deficits	L
Alzheimer disease	MB, MH
microangiopathy	MB, MH
vascular dementia	MB, MH
cognitive dysfunction	L, MB, MH
processing speed	L, MB
executive function	L,MB
memory	L,MB
attention	L,MB

L=Large (>5 mm), MB=Microbleed (<5 mm and >1 mm), MH=Microhemorrhage(<1 mm)

Figure 3.3: Impact of brain hemorrhages on human health.

When the intracranial pressure is controlled, the amount of bleeding into the brain determines the amount of brain damage and outcome of the patients [8, 122, 99], however hemorrhages may expand within one day of onset [2, 76, 178, 9].

3.3 Silent Hemorrhages (Small)

Recently, with advancements in imaging technology, small hemorrhages have been discovered in the brain of humans. These types of hemorrhages result from the rupture of small vessels, they do not present obvious symptoms (silent) and are not life threatening. To be classified as small hemorrhages or microbleedings, their size has to be less than 5 mm [111].

3.3.1 Detection of Silent Hemorrhages

For clinical use, gradient-echo $T2^*$-weighted MRI is the most sensitive current method to detect microbleeds [131]. Blood causes focal dephasing of the MRI signal and hemorrhages appear as dark spots on brain $T2^*$-weighted MRI [111]. White matter changes and clots have different appearance (brighter) on $T2^*$-weighted scans [125].

The appearance of microbleeds on the MRI range from 2 to 5 mm, however in post-mortem tissue of humans it is also common to find hemorrhages of smaller size. In this dissertation, the term microhemorrhage is used to refer to microbleeds with a diameter of several micrometers (<1 mm). MRI images do not represent the true size of microbleeds, usually they appear larger (∼1.5 times) due to a blooming effect from the MRI [132]. Detection using MRI is not always reliable, furthermore detection of microhemorrhages using $T2^*$-weighted MRI has not been assessed. In studies that correlate MRI with histology examinations, additional bleedings have been found in the histological sections that were not previously detected by MRI, sometimes contrarily, microbleeds detected with MRI could not be confirmed by histology [38]. Figure 3.4 shows a hemorrhage of ∼150μm diameter found in a post-mortem human brain.

3.3.2 Effects of small hemorrhages on Human Health

Microbleedings have been detected in healthy people with no evidence of symptoms, Roob et al. found that in a sample of healthy individuals between 44 and 79 years old, 6.4% of them had microbleeds. Since MRI does not reliably detect microbleeds that are smaller than 1 mm, a much greater incidence is expected.

When reviewing the incidence of microbleeds in people that suffer from different disease conditions, microhemorrhages were mostly found in patients that

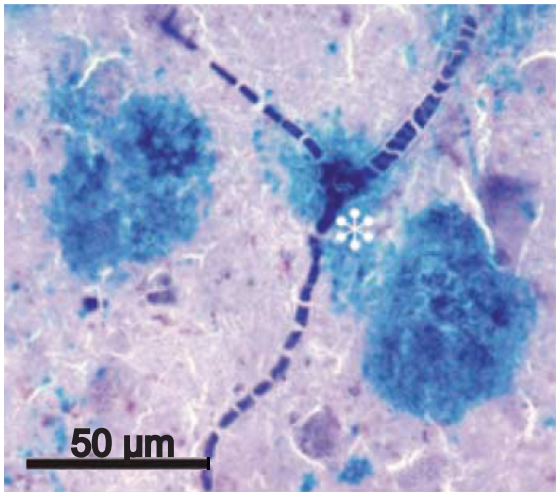

Figure 3.4: Presence of microhemorrhage on postmortem human brain. Figure adapted from [21]

had a previous symptomatic hemorrhage (68%) or people with cerebral microangiopathy (57%). Microbleeds were also found in people with vascular dementia and Alzheimer disease, but 70% of these patients also displayed cerebral microangiopathy [160]. A general agreement exists on the prevalence of microbleeds among patients with Alzheimer disease, in these cases, microbleeds appear to occur more often in the brain cortex and subcortex [55, 103].

In addition to being warnings signs for a major stroke, Alzheimer disease and microangiopathy, microbleeds appear to have repercussions in cognitive function. Several studies have found strong correlation between them and cognitive impairment. It has been shown that processing speed, executive function, memory and attention is worse among patients with microbleeds when they are compared with controls [171, 120, 80]. Location and number of microbleeds are also relevant to the degree of cognitive impairment.

Fewer studies have looked at the incidence of microhemorrhages (microbleeds smaller than 1 mm) in human brains. This is because the only accurate way to localize them is through meticulous examination of finely sliced post-mortem brain

tissue. Similar to larger microbleeds, microhemorrhages have been found in healthy individuals as well as in patients with Alzheimer disease, however they are more abundant on Alzheimer cases [21].

Studying damage caused by microbleeds has many challenges, one of them is that they are frequently accompanied by other types of vascular lesions such as infarcts, that occur with Cerebral Autosomal Dominant Arteriopathy with Subcortical Infarcts and Leukoencephalopathy (CADASIL) patients, or amyloid plaques present in Alzheimer patients. Distinguishing the different pathologies associated with each type of lesion is key to understanding what causes cognitive decline. Figure 3.3 summarizes the clinical impact of small hemorrhages on human health.

3.4 Models to Study Hemorrhages

The four common animal models used to study brain hemorrhage are: injection of blood or its constituents, injection of bacterial collagenase, transgenic animals, and laser ablation of vessel wall.

Different volumes of blood or blood constituents can be injected into the brain of animals in an effort to replicate the effects caused by a hemorrhage. In this type of model the needle will cause damage to the tissue and blood may come back through the needle injection path. Another disadvantage is that the blood vessel is not disrupted; and this may not reproduce some of the molecular pathways involved in hemorrhages. The smallest hemorrhage volume achieved with this type of model is around $\sim$5 μl [10, 104].

Bacterial collagenase, an enzyme that disrupts the basal lamina of blood vessels, can also be injected into the parenchyma of animals to study intracerebral hemorrhage. Injection of collagenase causes bleeding over an extended period of time and deteriorates neighboring tissue usually affecting more than a single vessel.

Another main disadvantage of using collagenase is its neurotoxicity [126, 145, 169]. These types of hemorrhages are very diffuse and the smallest achieved size reported in literature using this model is 1 to 2 mm diameter in transversal area [101]. Hemorrhages created injecting collagenase cause more damage compared to those made by the blood injection intracerebral hemorrhage model (figure 3.5) [94].

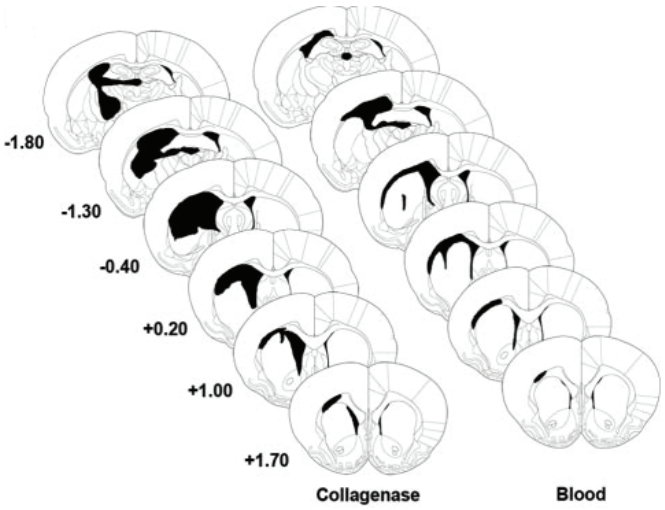

Figure 3.5: Blood and collagenase models. Schematics of hemorrhages induced by either collagenase or blood injection. Hemorrhages had initial similar amount of bleeding, but collagenase injection hemorrhages had greater hematoma size and damage 6 weeks after, taken from [94].

Syndromes characterized by the presence of microbleeds such as hypertension and Cerebral Autosomal Dominant Arteriopathy with Subcortical Infarcts and Leukoencephalopathy (CADASIL) can be induced in mice to produce naturally occurring small hemorrhages including microhemorrhages. Hypertension is caused by disruption of the angiotensin system either by overexpression of angiotensin genes in engineered mice [68, 166] or by administration of Angiotensin in wild type mice [165]. CADASIL mice may also be engineered by mutation of the NOTCH3 gene [73]. The main disadvantages of these genetically created models are that the number and location of microhemorrhages cannot be controlled and other symptoms associated with the syndromes are hard to differentiate from the hemorrhage pathology.

A recent model is the use of two photon microscopy and tightly focused, high energy laser pulses to select and irradiate a specific vessel until it bursts [110]. This model has the advantages of being able to control for the location, quantity and size of hemorrhage. A range in size from very small (no leakage of red blood cells, only plasma) to moderate (a red blood cell area with 500 μm diameter) can be generated by varying the intensity and duration of laser pulses.

3.5 Pathology After a Hemorrhage

Inflammation in the brain tissue has been proven to occur after a hemorrhage, even in those of small size (microhemorrhages). In larger hemorrhages, inflammation occurs in addition to the damage caused by the hematoma mass effects.

When blood extravasates from blood vessels, blood components such as erythrocytes, leukocytes (granulocytes, monocytes, limphocyte), and plasma proteins (thrombin, plasmin, fibrin, etc.), make contact with neurons disrupting the extracellular environment. Thrombin is also produced in the brain immediately after disruption of the vessel wall to initiate coagulation [50].

Thrombin appears to be highly toxic for neurons and astrocytes since in-vitro experiments have shown cell death after thrombin exposure [11, 77]. However, literature findings are controversial since Xi et al. [175] have not found negative effects at low concentrations. Thrombin and extracellular glutamate in the blood may cause excitotoxic cell damage and lactic acidosis formation [47].

The hemoglobin inside the erythrocytes (oxyhemoglobyn) becomes deoxyhemoglobin when erythocytes leave the vessel and one week later change to methemoglobyn. In in-vitro experiments hemoglobin causes death of neurons only after one day of exposure but not before [163]. After a hemorrhage microglia and monocytes (which will differentiate in macrophages) get recruited from surround-

ing areas [137, 23, 100] and participate in degradation and sequestration of blood products. Literature reports a wide range of times for erythrocytes lysis onset, varying from 1 to10 days after a hemorrhage [22, 67, 162]. The heme protein in the hemoglobyn gets degraded into iron, carbon monoxide and biliverdin [163], resulting in an increase of the iron concentration. Microglia, macrophages, neutrophils and iron, all may contribute to cell injury via oxidative stress [54, 141, 67, 163, 184]. Free radical scavengers [174] and iron receptors [163] are also activated to maintain brain homeostasis, however they may not be enough to restrain oxidative stress, therefore the amount of bleeding may be an important factor related to degree of injury.

Pathology reported in literature from animal models and human postmortem tissue	**Type of Hemorrhage (by size)**
intracranial pressure	L
accompanied by ischemia	L
microglia	L, MB, MH
macrophages	L, MB, MH
limphocites	L, MB, MH
hemo-oxigenase	L, MB, MH
metalloproteases	L, MB, MH
oxidative stress	L, MB, MH
neutrophils	L, MB, MH
iron	L, MB
glutamate	L
lactate	L
apoptosis	MB
necrosis	L, MB
caspases	L
cathepsin	L
autophagic vacuoles	L
citocrome C	L

L=Large (>5 mm), MB=Microbleed (<5 mm and >1 mm), MH=Microhemorrhage(<1 mm)

Figure 3.6: Pathology found in brain hemorrhages classified by size.

Over time the hemorrhage is cleared out sometimes leaving hemosiderin deposits (iron storage). While in large hemorrhages it is evident that cell death occurs in neighboring areas via apoptosis and necrosis [176, 49, 37, 98, 97, 122], in

smaller hemorrhages the presence of cell death remains inconclusive. For example, Schrag et al. [132] reports 4% of apoptotic cells in neighboring areas after examining four brain hemorrhages in mice, however the exact size of the hemorrhages examined was not specified, only a wide range in the diameter hemorrhage from 0.2 to 3 mm was given. While 0.2 mm hemorrhage diameters are a good model for mimicking microbleeds, a 3 mm diameter in the brain of a mouse may be too large. Furthermore, caspases [47], nuclear factor-kB complex [62], cytochrome c [105] and autophagic vacuoles [57], which are associated with cell death have been only found in large hemorrhages. Figure 3.6 indicates the pathology found after a brain hemorrhage from different experiments reported in literature using animal models and postmortem human brains.

CHAPTER 4

EFFECTS OF ANTICOAGULANTS ON MICROHEMORRHAGES

This chapter contains my work from a collaboration resulting in two manuscripts:

Arne Lauer, Flor A. Cianchetti, Elizabeth M. Van Cott, Frieder Schlunk, Elena Schulz, Helmuth Steinmetz, Chris B. Schaffer, Eng H. Lo, Christian Foerch. **Anticoagulation with the Oral Direct Thrombin Inhibitor Dabigatran Does Not Enlarge Hematoma Volume in Experimental Intracerebral Hemorrhage**, Circulation, in-press.

Christian Foerch, Nathanael L. Rosidi, Frieder Schlunk, Arne Lauer, Flor A. Cianchetti, Emiri Mandeville, Ken Arai, Kazim Yigitkanli, Klaus van Leyen, Helmuth Steinmetz, Chris B. Schaffer, Eng H. Lo. **Intravenous tPA therapy does not worsen acute intracerebral hemorrhage in mice**, PLoS ONE, in-press.

4.1 Abstract

The early use of anticoagulants as a therapy for ischemic strokes has been limited when there is uncertainty as to the type of stroke that the patient suffers. In addition most anticoagulants may exacerbate the bleeding caused by a brain hemorrhage. However, not all anticoagulants share a similar mechanism and some of them may not further increase bleeding from a brain hemorrhage, but would be beneficial in instances where immediate reperfusion is needed or when blood clotting needs to be continuously inhibited. In particular, this study examine the effects of Tissue plasminogen activator (tPA), direct thrombin inhibitor dabigatran etexilate (DE), warfarin and heparin therapy on microhemorrhage size. Using a laser-induced microhemorrhage model hematoma sizes were compared between the different therapies administerd to mice with respect to controls. Results demonstrated that warfarin and heparin treated mice exhibited larger hemorrhages than controls, however no difference was found between mice treated with DE, tPA and controls. This suggests that some anticoagulants have greater risks of developing brain hemorrhages than others, with similar benefits.

4.2 Introduction

Stroke is a major cause of death and long-term disability in the world [180]. Strokes can be either ischemic or hemorrhagic. Ischemic stroke is nine times more common than hemorrhagic stroke. Anticoagulation therapies with vitamin K antagonists are mainly used for treatment of thrombotic and thrombembolic disorders, and have been highly effective in, for example, reducing the risk of cardioembolic brain infarction in patients with atrial fibrillation. When ischemic strokes can not be prevented, recombinant tissue plasminogen activator [187] is commonly use for

dissolving ischemic clots in the brain.

Some limitations of vitamin k antagonists (warfarin, heparin, etc) are: a narrow therapeutic window, the need for regular coagulation monitoring and critical food and drug interactions [6, 133]. In addition, the risk of developing intracerebral hemorrhage is the most feared complication. Both clinical and experimental studies revealed that anticoagulation associated with intracerebral hemorrhage (ICH) is a devastating type of stroke with short-term mortality rates exceeding 50%, due to increased hematoma volumes and prolonged bleeding [2, 39, 69, 139].

Recently, the search for alternative strategies for long-term anticoagulation has intensified, to overcome the problems associated with vitamin K antagonists [26, 154]. One possibility, is the use of oral direct thrombin inhibitor Dabigatran etexilate (DE) which binds reversibly only to the active site of the thrombin molecule. In a clinical trial (RE-LY trial), DE showed significantly reduced rates of stroke along with a favorable risk-benefit-profile as compared to warfarin in patients with non-valvular atrial fibrillation [18]. In addition, DE has also been evaluated for the prophylaxis of thrombotic complications in patients undergoing total hip replacement [34]. Furthermore, DE is under investigation for the treatment of acute symptomatic venous thromboembolism [133] and long-term secondary prevention of venous thromboembolism [88]. Very limited information is available on the characteristics of ICH occurring during treatment with direct thrombin inhibitors [20]. For both doses of DE used in the RE-LY trial, the incidence of intracranial bleeding was significantly lower than in the warfarin group [18] Still, bleeding risk increased dose-dependently. The influence of DE pretreatment on hematoma expansion and prognosis of ICH in comparison to warfarin remains undetermined.

A diagram of the simplified coagulation cascade and the coagulation factors that are inhibited by different anticoagulants such as heparin, warfarin and DE

are shown in figure 4.1.

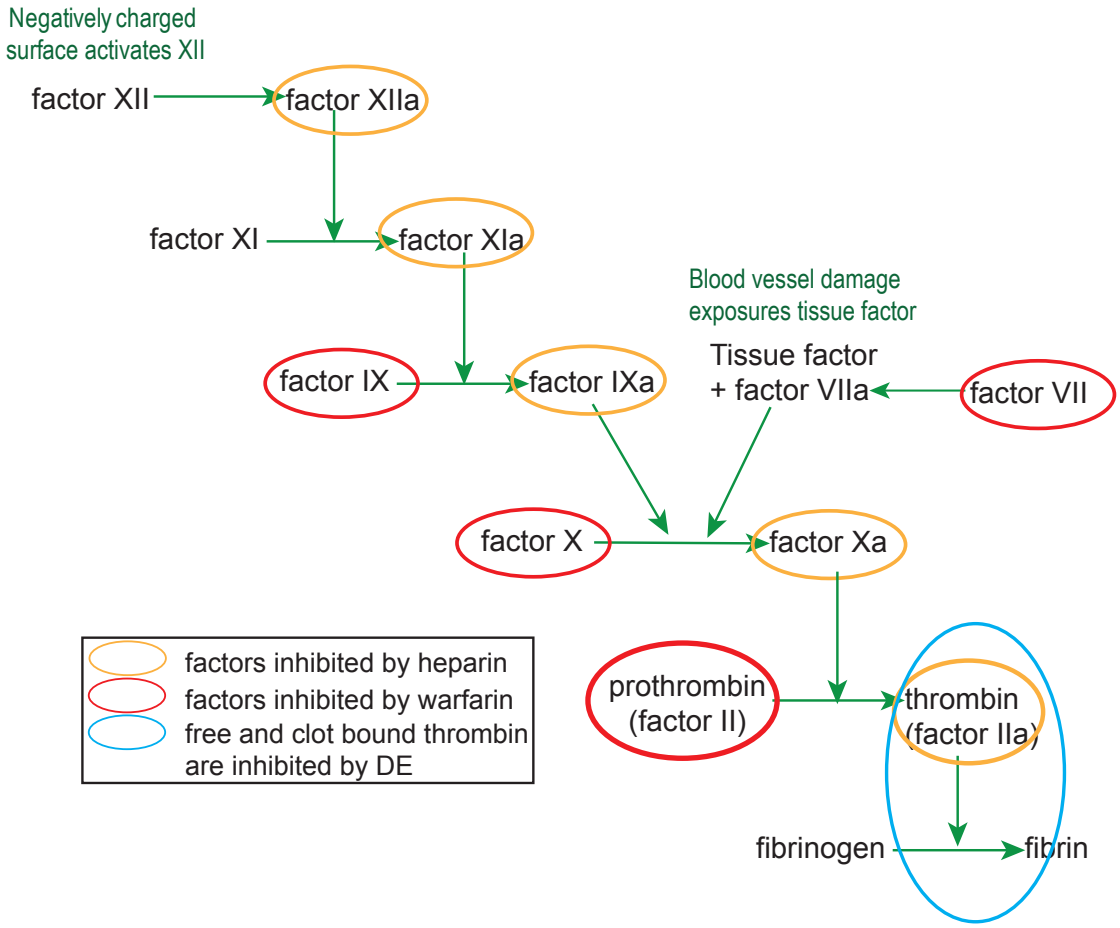

Figure 4.1: Mechanism of anticoagulants on the coagulation cascade. Heparin when bound to antithrombin inhibits free thrombin and activated factors XIIa, XIa, IXa, Xa. Warfarin, inhibits the production of prothrombin and factors IX, X and VII by the liver. DE inhibits free thrombin and clot bounded thrombin.

The main limitation of Tissue plasminogen activator (tPA) application is the need for its rapid use after a clot occurs and the existence of hemorrhagic strokes has to be ruled out. The sooner patients receive tPA and reperfuse, the better the odds ratio for improved outcomes. In current clinical practice, performing a brain scan is considered indispensable prior to tPA therapy, to avoid inadvertent administration of tPA to patients with hemorrhagic instead of ischemic stroke [1]. This induces a substantial time-to-treatment delay, as tPA cannot be administered directly at the patient home or in an ambulance.

Despite obvious advantages of tPA and that it has been approved by the FDA for more than 10 years, its use is still limited to less than 5% of all ischemic strokes due to it being restricted uniquely to cases when ICH has been ruled out. The widespread assumption that tPA therapy would worsen ICH seems intuitive, but lacks scientific validation.

In this chapter, using similar methods, we separately tested the effects of the direct thrombin inhibitor DE and intravenous administration of tPA on hematoma volume after a microhemorrhage was induced in a mouse.

4.3 Methods

4.3.1 Animals

All experiments were conducted in accordance with the National Institute of Healths Guide for the Care and Use of Laboratory Animals and procedures were approved by Cornell University Institutional Animal Care and Use Committee. For the DE study 9 male CD-1 mice aged 12 to 16 weeks (mean body weight 39.6g) were used. For the tPA study 11 male and female C57BL/6J mice aged 10-12 weeks (mean body weight 30 g) were used. Bilateral chronic cranial windows (∼3 mm radius with center at stereotactic coordinates in relation to bregma: 3 mm posterior, 0 mm lateral) were implanted in all mice using previously reported methods [110, 130].

4.3.2 Drug Administration

DE Study

Ten days after surgery, animals were blindly and randomly assigned to receive pretreatment with DE (dosage 75mg/kg, n=3), warfarin(n=3) or PBS (control,

n=3).

A DE tablet (110mg, Pradaxa, Boehringer Ingelheim, Ingelheim, Germany) was dissolved with 1% dimethylsulfoxide (DMSO) in saline solution. A solution with a DE concentration of 20mg/ml was prepared. DE mice were fed three times orally using a gastric tube with intervals of eight hours. Each feeding consisted of 0.15 mL of the respective solution resulting in a dose of 75mg/kg body weight per feeding for a 40g mouse. Control mice were fed three times with 0.15 mL PBS following the same modus of application. Warfarin was administered via drinking water following a previously established protocol. For mice with a body weight of 40g, a daily water consumption of 15 mL / 100g provided an estimated warfarin intake of 0.1 mg (2.5 mg/kg) within a 30 hour feeding period.

ICH induction of laser-induced vessel rupture, respectively, was performed 0.5 hours after the last oral gavage of either DE or PBS and at the end of the warfarin feeding period.

tPA Study

Five days after surgery and immediately before the imaging session mice were anesthetized with isofluorane and the right jugular vein was cannulated. After ligating the distal part of the vessel, a PE-10 tube was inserted into the jugular vein and moved forward in the proximal direction, then the tube was fixed and the suture was closed. The animals were placed in a stereotactic frame under the two-photon microscope.

Animals were assigned to receive intravenous saline (500 μl), recombinant human tPA (10 mg/kg, diluted in 500 μl saline) or heparin (100 U/kg, diluted in 500 μl saline). Immediately before laser induction of hemorrhage, a 50 μL bolus injection of saline (n=4), tPA (n=11), or heparin (n=10) was infused through the jugular vein catheter, then after five minutes a constant infusion rate (15 μL/min)

was set using a syringe pump (PHD2000; Harvard Apparatus), i.e. 30 min of drug infusion during and after hemorrhage. The correct intravenous position of the catheter was double-checked by drawing some blood into the tube after the injection.

4.3.3 In Vivo Imaging and Hemorrhage Induction

In preparation to induce ICH, mice were anesthetized with isofluorane (∼2.0%). Body temperature was maintained at 37.5°C with a heat blanket and a thermometer. A retro-orbital i.v. injection of 0.1 mL of 5% (wt/vol) Texas-Red dextran (70 kDa) fluorescent dye in physiological saline was given to label the vasculature. We imaged the brain using in vivo two-photon excited fluorescence microscopy (excitation source: 1045 nm, 1 MHz, 350 fs pulse train from a Yb-fiber oscillator/amplifier system; μJewel FCPA, IMRA America, Inc.; filter: 645/65 nm Chroma filter). Bleeding was induced in two to five targeted penetrating arterioles per mouse by injuring the endothelium with tightly focused femtosecond laser pulses as described in [110]. The laser only causes damage at the focus (∼1 μm^2) leaving the surrounding regions intact(figure 2.8).

Microhemorrhage depth varied between 50 and 120 μm beneath the cortical surface. The bleedings were separated by at least 1mm between each other. Stacks of images were taken at the hemorrhage site every 2 μm from brain surface to 150 μm depth. For the DE study, image stacks were taken before and immediately after (∼5 min) ICH induction while for the tPA study, image stacks were taken before and 30 min after ICH induction. The laser-induced hemorrhages are characterized by a core region filled with red blood cells (RBC) and a surrounding blood plasma region. The RBC core appeared black, while blood plasma is bright, labeled by the Texas Red dye. To determine hemorrhage size, we measured the diameters of

the RBC-filled microhemorrhage core and of the surrounding blood plasma-filled region from a 20 μm z-projection of the stack images centered on the hemorrhage.

4.3.4 Statistical Analysis

Matlab (The mathworks Inc.) and JMP version 8.0 (SAS Institute Inc.) were used for statistical analysis. Lilliefors and Levenes tests were used to analyze data distribution and equality of variances. Diameters of the microhemorrhage regions were compared using Welchs ANOVA and Dunnetts method. Mann-Whitney U tests were used if data was not normally distributed. P-values less than 0.05 were considered statistically significant.

4.3.5 Post-mortem histology

At the end of each imaging session for the tPA study, animals were transcardially perfused with 30 ml of phosphate buffered saline (PBS) (Sigma-Aldrich) and 100-ml of 4% (wt/vol) paraformaldehyde (Fisher Scientific) in PBS. The brain was extracted from the skull and cryoprotected by immersion in 30% (wt/vol) sucrose in PBS for 24 hr and then in 60% sucrose in PBS. Fiducial marks were made in the left corners of the craniotomy window by vertically inserting a 25 gauge needle 2 mm into the brain. The needle was externally tinted with black ink (Parker). The fiducial marks were placed in known locations relative to the microhemorrhage sites. The brain was then frozen and cut into 50 μm thick coronal sections on a cryostat. The sections were mounted onto microscope slides (Superfrost Plus, Fisher Sci.) and incubated for 12 min with diaminobenzadine (DAB) (Peroxidase Substrate kit, Vector labs, no. SK-4100) to stain endogenous peroxidase in RBCs and then rinsed with deionized water. The sections were photographed under brightfield and fluorescence microscopy. Fiducials were mapped and used to iden-

tify the slices and location within slices where microhemorrhages were located. Microhemorrhages were identified on the basis of both DAB stained RBCs and Texas Red dextran fluorescence in the parenchymal space (figure 4.2).

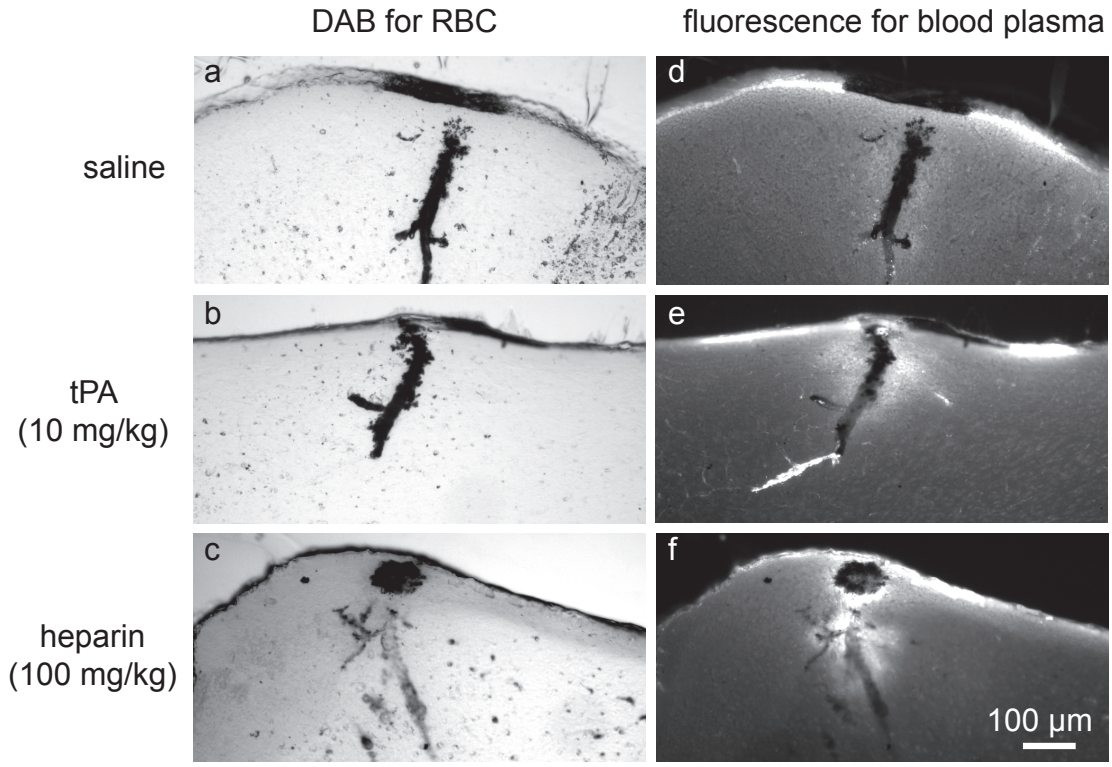

Figure 4.2: Post-mortem histology of laser-induced microhemorrhages. Representative coronal post-mortem tissue sections of microhemorrhages from animals treated with saline (a,d), tPA (b ,e) or heparin (c,f). Panels (a-c) show white-light transmission images treated sections, which show the RBCs that have hemorrhaged into the tissue as black. Panels (d-f) show fluorescence images of extravasated Texas Red-dextran for the same sections as panels (a-c).

4.4 Results

4.4.1 DE Study

A total number of 12 (across 3 control mice), 13 (across 3 DE mice), and 13 (across 3 warfarin mice) microhemorrhages were induced in each group, respectively (figure 4.3). Both the diameter of the RBC core and the diameter of the

blood plasma filled region were larger for warfarin-pretreated mice than for controls and DE-treated animals (mean ± SD; controls: 116.2 ± 38.0 μm and 327.8 ± 80.4 μm; DE mice: 108.1 ± 35.2 μm and 331.6 ± 51.2 μm; warfarin mice: 192.8 ± 101.4 μm and 467.5 ± 113.6 μm, respectively; Figure 4.4). The Welchs ANOVA between group differences for RBC- and blood plasma diameters were significant (p=0.035 and p=0.003, respectively). Post-hoc analysis revealed no differences in RBC- and blood plasma diameters between DE-treated mice and controls (p=0.935 and p=0.991, respectively), but warfarin animals had significantly larger RBC and plasma diameters than both DE mice and controls (warfarin vs. DE: p=0.008 and p<0.001, respectively; warfarin vs. control: p=0.013 and p<0.001, respectively).

4.4.2 tPA Study

A total number of 9(across 4 control mice), 11 (across 4 tPA mice), and 10 (across 3 heparin mice) microhemorrhages were induced in each group, respectively (figure 4.5A). The size of the red blood cell (RBC) filled microhemorrhage core and the surrounding blood plasma filled region were not different between saline and tPA treated mice. In contrast, hemorrhages produced while infusing heparin were significantly larger than saline controls (RBC area, p=0.0025; plasma extravasation area, p=0.025). Figure 4.6 show the correspondent box-plots.

We identified 18 femtosecond laser-induced intracerebral microhemorrhages in post-mortem tissue sections. Across all treatments, we found that RBCs spread vertically along the perivascular space surrounding the targeted penetrating arteriole(figures 4.2A-C). Blood plasma, however, was able to diffuse through the parenchyma tissue and exhibited a more extended spatial pattern (figures 4.2D-F). We consistently observed that heparin treatment led to a larger spherical RBC filled volume compared to saline and tPA treatments(figures 4.2C and 4.2F).

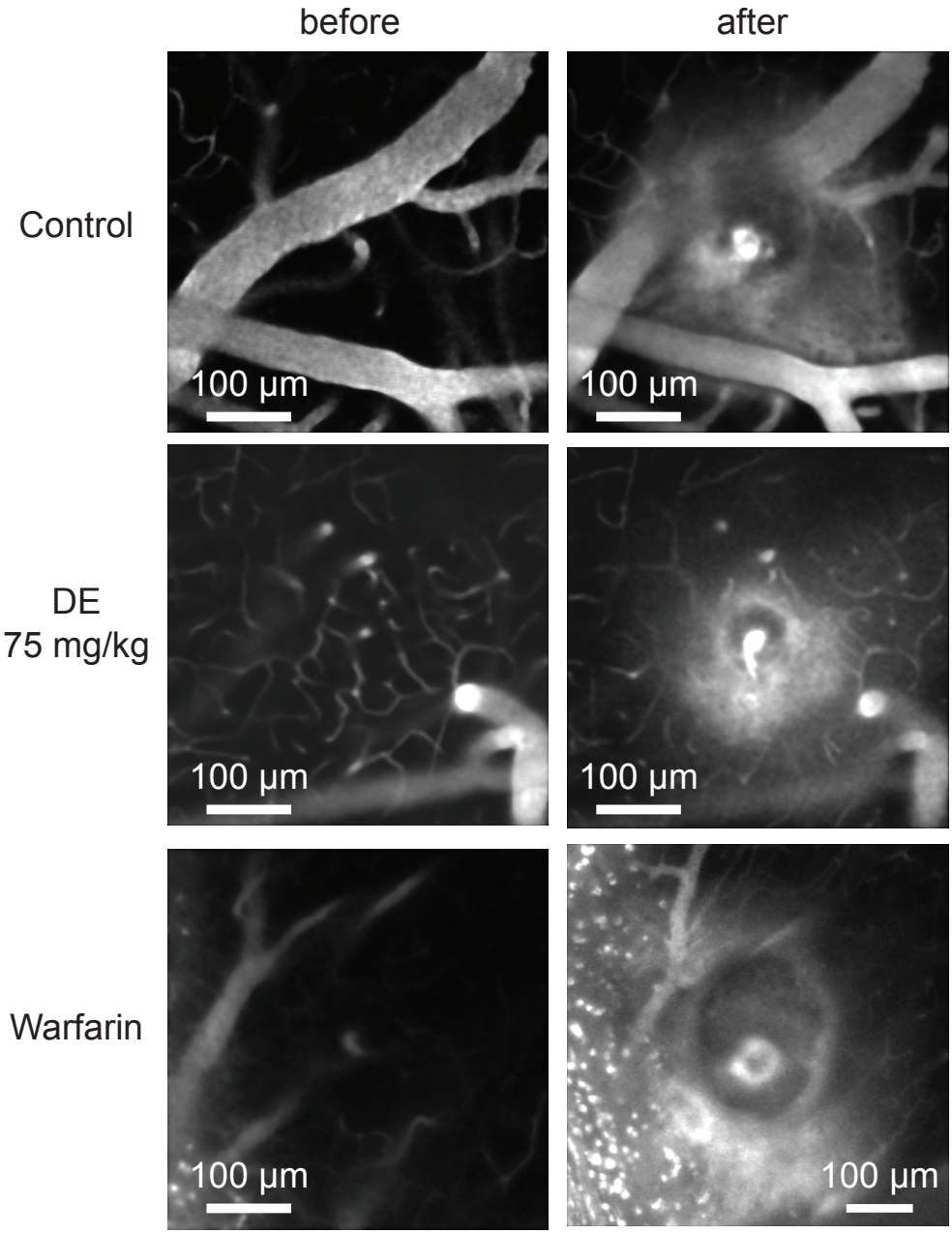

Figure 4.3: In-vivo 2PEF microhemorrhages, DE study. Projections of in-vivo two-photon excited fluorescence image stacks of fluorescently labelled blood plasma spanning a 20 μm depth centered at the hemorrhage origin. Image stacks are shown before and after rupturing the wall of a single penetrating arteriole using tightly focused femtosecond laser pulses. Representative examples from the three differently treated groups (saline-treated controls, DE 75mg/kg, warfarin) are shown. Extravasated plasma is visualized by diffuse fluorescence and can be seen in the post hemorrhage images in a halo surrounding the target vessel. The dark core immediately adjacent to the target vessel is filled with red blood cells.

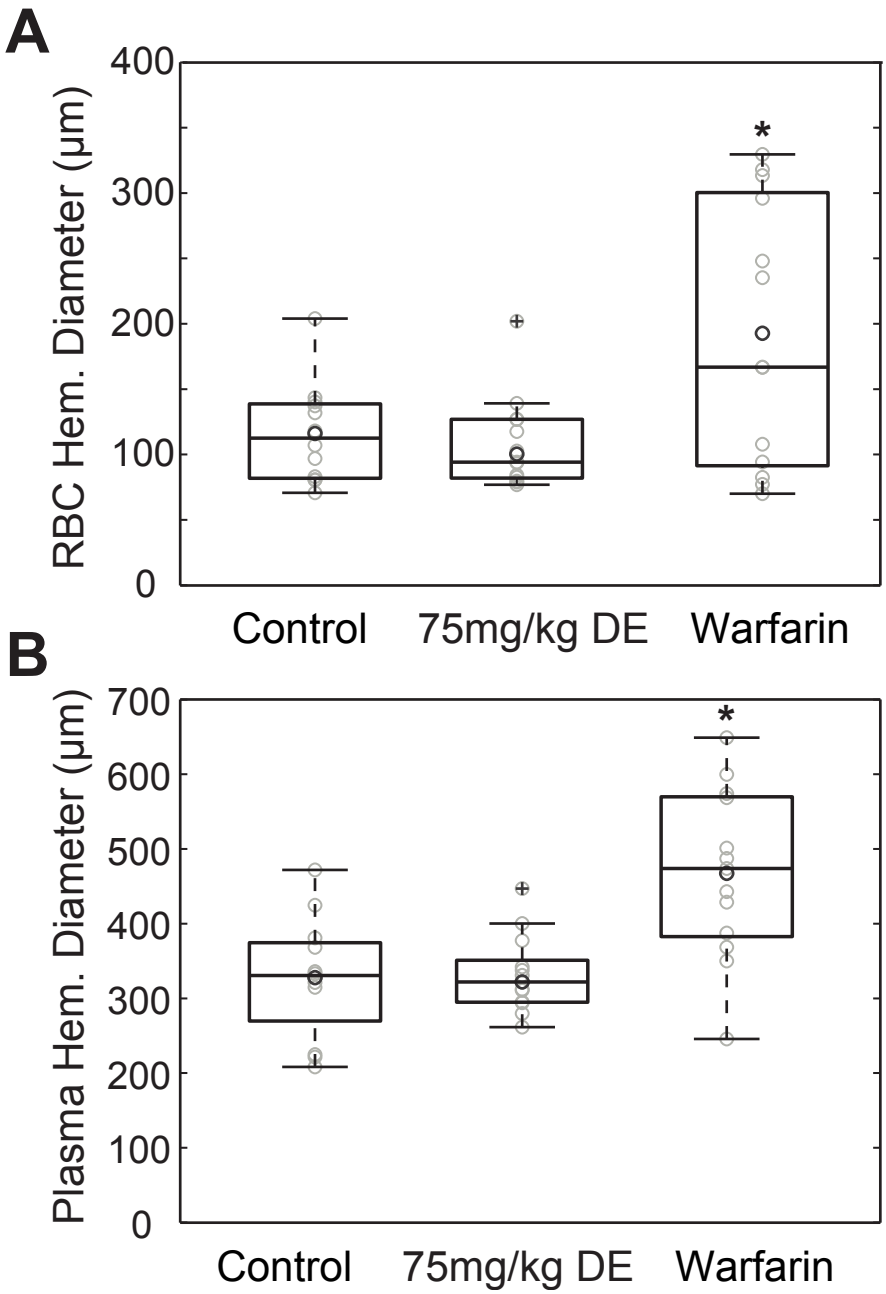

Figure 4.4: Hemorrhage size for DE study. A.Diameter of red blood cell filled core after laser-induced microhemorrhage in controls (C) and in mice pretreated with DE (75mg/kg) or warfarin (n=12-13 microhemorrhages per group). B. Diameter of plasma extravasation volume after laser-induced microhemorrhage for the same lesions shown in A. Data are displayed using box plots with the box indicating the median and the 25th and 75th percentile, respectively. Whiskers extend to the maximum and minimum values that are not outliers. Circles in light grey represent individual data points. Outliers have a cross imbedded in the circle. The dark grey circle represents mean without outliers. $*p < 0.05$ as compared to controls.

4.5 Discussion

We investigated in two different studies, the effects of pretreatment with the direct thrombin inhibitor DE before ICH induction and treatment with tPA administration after ICH induction on hematoma volume. As positive controls, the vitamin-K antagonists warfarin and heparin were used on the DE and tPA studies, respectively. Whereas warfarin and heparin anticoagulation led to largely increased hematoma volumes, hematomas in DE and tPA treated mice did not differ from control animals.

4.5.1 DE Study

Our study suggests that DE anticoagulation has much less devastating effects in case of intracerebral bleeding than warfarin anticoagulation. What might be the reasons why warfarin but not dabigatran anticoagulation leads to enlarged hematoma volumes in case of ICH? In vitro investigations revealed that deficiencies of the coagulation factors II, VII and X cause delayed clot initiation and affect clot propagation and clot strength. However, the presence of a small amount of factor II activity already resulted in clot initiation values similar to those in control plasma, whereas nearly every decrease of the factors VII and X further increased time to clot [107]. Following the propagation phase of coagulation, the secondary thrombin burst leads to the activation of thrombin activatable fibrinolysis inhibitor (TAFI), leading to down-regulation of fibrinolysis. Direct thrombin inhibitors fail to inhibit TAFI generation, while drugs that target factor Xa (fondaparinux, heparin and warfarin) enhance plasma fibrinolytic potential [90]. This may contribute to their increased bleeding potential. Factor II activity by DE mediated univalent, reversible thrombin inhibition may still result in sufficient hemostasis in the scenario of ICH. Our pathophysiological hypothesis is supported by other animal

studies that observed a bleeding time prolongation after DE therapy only at supra therapeutic doses [173]. In addition, a dissociation between antithrombotic efficacy and absence of bleeding time prolongation was reported in studies using different oral thrombin inhibitors [91, 116, 123].

In the RE-LY trial, incidence rates of ICH in DE treated patients were found to be reduced as compared to warfarin treated patients, despite a similar rate of antithrombotic efficiency. This finding might be linked to the decrease of other vitamin K dependent coagulation factors (other than factor II) in case of warfarin anticoagulation and their contribution to hemostasis, while DE does not directly affect parameters other than factor II [18]. Our experimental study investigating the behavior of laser-induced cerebral microbleeds after DE and warfarin pretreatment provides a more detailed insight: microhemorrhages induced in warfarin-treated mice more often expand towards having increased RBC and blood plasma diameters, whereas microbleeds in DE mice do not differ from controls.

The clinical implication of our findings is manifold: Intracerebral bleeding occurring during warfarin treatment is particularly severe, with short-term mortality rates of 50% [2]. Clinical and experimental data have shown that hematoma expansion is prolonged in the case of warfarin anticoagulation, thus leading to larger hematoma volumes and a worse functional outcome [2, 39, 69, 139]. In warfarin associated ICH, measures to rapidly reverse anticoagulation may prevent such prolonged bleeding and may improve functional outcome [2, 139, 40]. Our data suggest that DE anticoagulation does not facilitate ongoing bleeding and extensive hematoma growth. It is likely that this is mirrored by better prognosis as well.

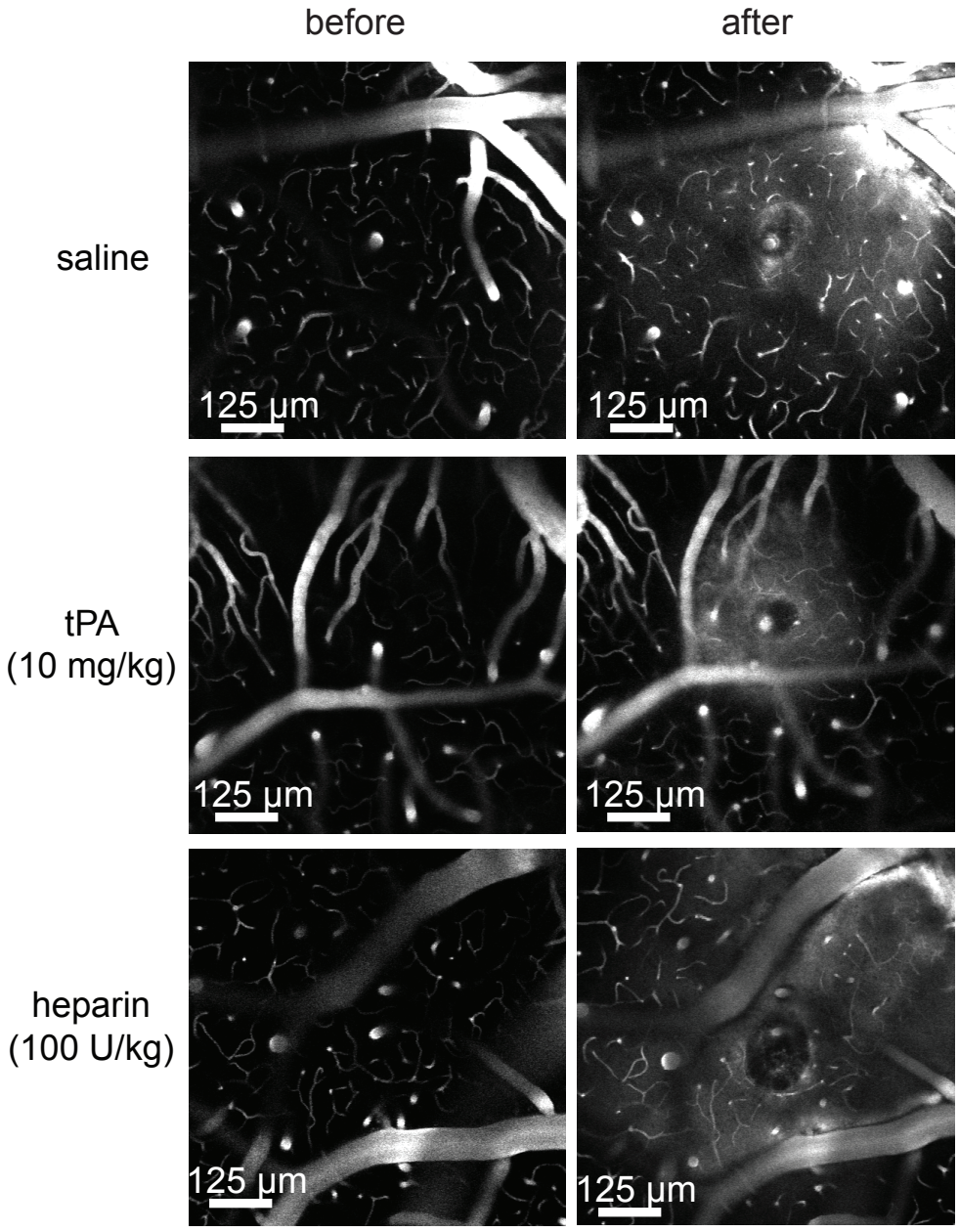

Figure 4.5: In-vivo 2PEF microhemorrhages, tPA study. A.2PEF in vivo image projections of fluorescently-labeled blood plasma spanning a 20μm depth centered at the hemorrhage origin. Image stacks are shown before and after rupturing the wall of the a single penetrating arteriole using tightly focused femtosecond laser pulses. Representative examples from the three different intravenous infusion groups (saline, tPA, heparin) are shown. Extravasated plasma is visualized by diffuse fluorescence and can be seen in the post hemorrhage images in a halo surrounding the target vessel. The dark core immediately adjacent to the target vessel is filled with red blood cells.

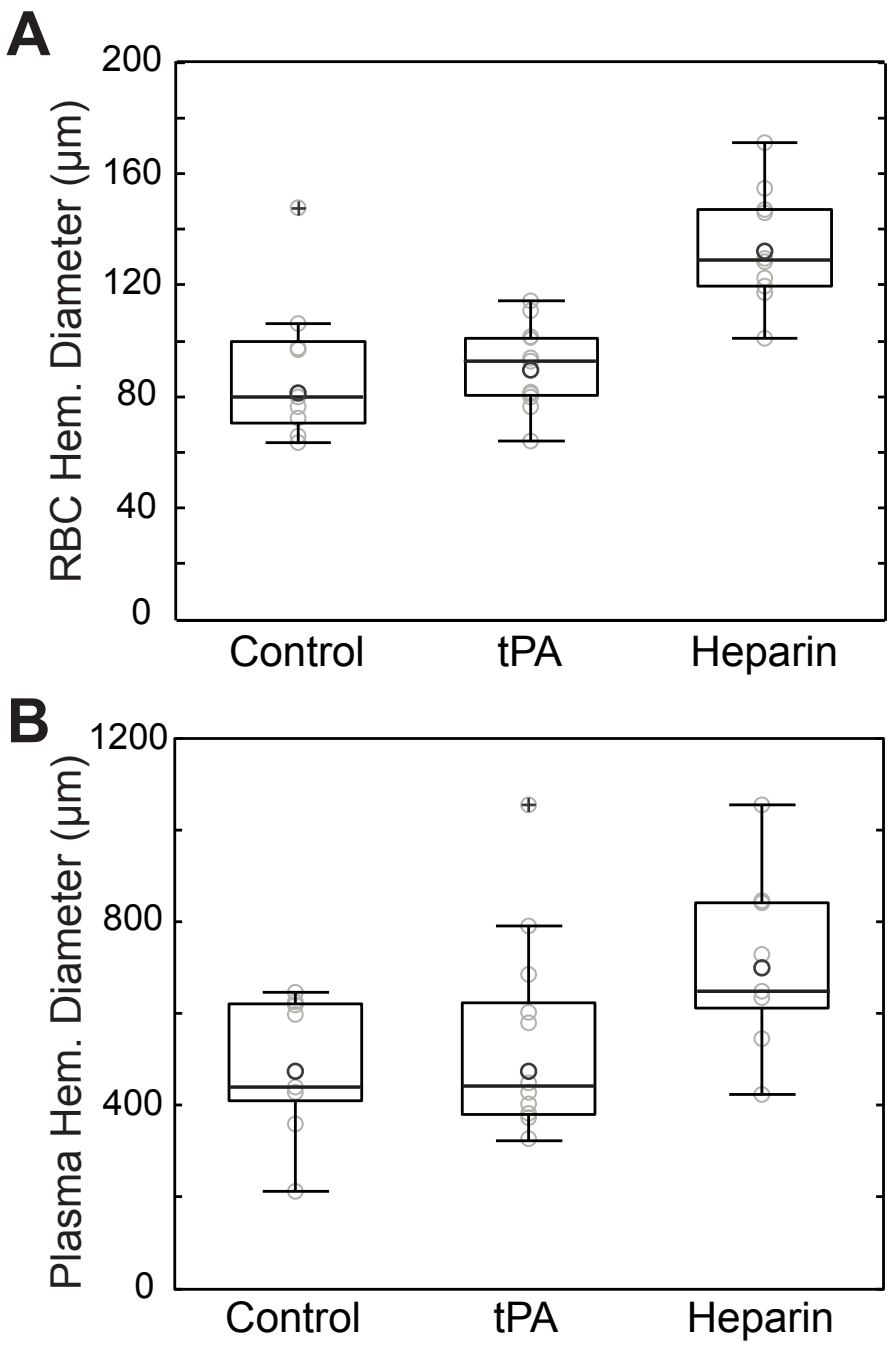

Figure 4.6: Hemorrhage size for tPA study. A.Area of red blood cell filled core after laser-induced microhemorrhage in mice treated with saline, tPA and heparin. B. Diameter of plasma extravasation volume after laser-induced microhemorrhage for the same lesions shown in A. Data are displayed using box plots with the box indicating the median and the 25th and 75th percentile, respectively. Whiskers extend to the maximum and minimum values that are not outliers. Circles in light grey represent individual data points. Outliers have a cross imbedded in the circle. The dark grey circle represents mean without outliers.

4.5.2 tPA Study

Our results stand in sharp contrast to the widespread but so far unproven assumption that tPA would enlarge hematomas if inadvertently given to patients with acute ICH. What might be the reasons why heparin but not tPA administration a leads to enlarged hematoma volumes in case of ICH? From a mechanistic standpoint, our data suggest that tPA does not amplify matrix metalloproteinases that exacerbate neurovascular injury during ICH. But there may be other multifactorial reasons as well. Unlike warfarin and heparin, tPA has no effect on primary hemostasis and does not delay initial coagulation. But as an activator of the fibrinolytic cascade, tPA increases the risk of rebleeding from previously hemostatic-stable areas [102]. So tPA could theoretically worsen intracerebral bleeding. On the other hand, the fibrinolytic activity of tPA is highly dependent on parameters such as clot structure. For example, platelet-rich thrombi are much less susceptible to tPA dissolution compared with erythrocyte-rich thrombi, mainly due to the release of platelet-derived plasminogen activator inhibitor [70]. Intracerebral hematomas consist of whole blood containing large amounts of platelets so it is possible that these structures may be more tPA-resistant. Another possible explanation for our finding is that the ICH clots surrounding ruptured brain blood vessels are heterogeneous and larger than singular intraarterial thrombi in ischemic stroke [126]. Standard doses of tPA may not be able to dissolve significant parts of the coagulated hematoma in order to induce rebleeding. Furthermore, ICH volumes may be stabilized by the counter pressure of surrounding brain tissue, which limits hematoma expansion. Together with parenchymal tissue destruction, elevated pressure in the affected brain areas may prevent systemic intravenously administered tPA from reaching the initial sites of vessel rupture.

The mechanisms involved in primary ICH are different from those that underlie

hemorrhagic transformation and reperfusion injury after ischemia. Hemorrhagic transformation during reperfusion injury are now known to be related to excitotoxic effects of tPA and neurovascular upregulation of MMPs [53, 169, 179], rather than the rebleeding of a previously terminated hematoma. tPA may not worsen ICH, but this is different from potential deleterious effects of tPA during cerebral ischemia and reperfusion. Our present data support this idea. tPA seems to amplify MMPs during cerebral ischemia-reperfusion but not ICH.

4.5.3 Summary

Our DE experimental study suggested that cerebral hemorrhages occurring during DE treatment are smaller and less harmful than those under warfarin anticoagulation. In terms of safety, this may represent a crucial advantage of the direct thrombin inhibitor DE over warfarin. Our tPA study suggested that intravenous tPA does not enlarge hematomas or worsen outcomes in ICH, therefore tPA could be administered at much earlier time points. This may vastly increase the effectiveness of this drug in patients with acute ischemic stroke.

CHAPTER 5

EFFECT OF MICROHEMORRHAGE ON NEURONS

5.1 Abstract

Although microhemorrhages are common in the brain of the elderly, the direct impact of these lesions on neural function remains unclear. In this work, we used femtosecond laser irradiation to rupture the wall of targeted arterioles in the brain of anesthetized rodents, producing a hematoma of ∼100 μm diameter. We studied the impact of these microhemorrhages on neural activity using cell-resolved two-photon imaging of bulk-loaded calcium-sensitive dye. We monitored peripheral sensory stimulus-induced calcium transients from individual neuronal cell bodies and regions of neuropil at different distances from the microhemorrhage before and 0.5, 2, and 4 hours after the creation of the lesion. We found that immediately after the hemorrhage the average amplitude of the stimulus-induced calcium response was reduced to about half within 150 μm from the hematoma. Beyond 300 μm, there was little effect on neural response, with a smooth increase in response amplitude from 150 μm to 300 μm from the lesion. Cortical function gradually improved with time and by four hours after the lesion the neural response had recovered to baseline everywhere but within 150 μm from the hematoma. To assess whether the cells closest to the microhemorrhage recovered over a longer timeframe, we developed a re-openable chronic cranial window preparation that allowed reinjection of calcium-sensitive fluorescent dye. We found that the response largely recovered by one day after the microhemorrhage even within 150 μm from the hematoma. This work suggests that neuronal function is transiently lost near a microhemorrhage, but recovers within one day after the lesion.

5.2 Introduction

Small, acutely asymptomatic, strokes are frequently found in the brain of elderly patients [158]. These lesions range in size from the several millimeter diameter strokes observable in MRI studies [80] to lesions only a few tens of micrometers in size revealed by post-mortem histology [21, 46]. The presence of even the smallest of these lesions has been associated with cognitive decline and dementia [82, 21]. Similar to large strokes, these microstrokes might be caused by occlusion of or bleeding from a microvessel, with microclots and microhemorrhages likely affecting the brain in different ways. Despite the importance of small strokes in neurological health, little is known about the progression of neural dysfunction following these lesions.

Following microclots, dendrite degeneration was observed near the ischemic core and although neural structures remained intact further away, there was an acute loss of neural activity up to 300 μm from the lesion [185]. This suggests that microclots cause cell death and neural dysfunction near the lesion, likely explaining their cognitive impact.

In contrast, it has been difficult to study the pathological consequences of a microhemorrhage due to the lack of good animal models of small vessel bleeds. Current hemorrhage models involve injection of either blood directly into the brain or enzymes that degrade the extracellular matrix, causing bleeding from many vessels [94]. Neural death and inflammation was found in the vicinity of these hemorrhages, however the hematomas created are greater than 1 mm in diameter and the mechanisms that cause cell injury after these lesions may not play the same role in microhemorrhages. Transgenic mice, such as hypertensive or CADASIL (Notch 3 mutation) animals, develop microhemorrhages with diameters of several hundred micrometers throughout the brain, which have been shown to

trigger inflammation [165, 5]. However it is difficult to follow the effects of microhemorrhages on cells in these animals because of the unpredictable timing and location of the lesions. Finally, extravasation of blood plasma into the brain due to a nearby ischemic lesion did not cause dendrite degeneration [185].

Here, we investigated changes in neural function after a single microhemorrhage. We used femtosecond laser pulses to rupture targeted arterioles in the brain of live, anesthetized rodents, creating microhemorrhages of $\sim$100 μm diameter [110]. We used two-photon excited fluorescence (2PEF) microscopy of bulk-loaded calcium-sensitive fluorescent dyes [140] to monitor the resulting changes in neural response to a peripheral stimulus. We found a decrease in neural response in the vicinity of the hematoma immediately after the bleed that recovered toward baseline over time, with regions further from the lesion recovering more quickly. These results show that even the smallest microhemorrhages can lead to transient loss of neural function, but suggest that any long-term impact is not caused by the inability of neurons to respond to input.

5.3 Methods

5.3.1 Acute Rat Preparation

All animal procedures were reviewed and approved by the Cornell University Institutional Care and Use Committee. We used 23 adult male Sprague-Dawley rats (Harlan, Inc.), ranging from 250 to 415 g in weight. Rats were anesthetized using 5% isoflurane (Vet-one, Inc.) and maintained at 1-2% throughout surgery. An intramuscular injection of glycopyrrolate (0.5 mg/kg rat) (Baxter, Inc.) was administered, the head was shaved, and eye ointment applied. The rat was transferred to a custom stereotaxic frame where bupivacaine (0.1mL, 0.125%) (Hospira,

Inc.) was administered subcutaneously on top of the head to provide local anesthesia. A ∼1.5 mm radius circular craniotomy was performed and the dura was removed. In order to access the hind paw somatosensory cortex, the center of the craniotomy was located 2 mm lateral and 1 mm caudal from bregma. After loading fluorescent dyes into the brain (see below), the craniotomy was filled with 1% agarose (A9793, Sigma) in artificial cerebrospinal fluid (ACSF) [79] and then sealed with a glass cover slip (50201, World Precision Instruments) that was glued to the skull using cyanoacrylate and dental cement (Co-Oral-lte Dental Mfg Corp.). One hour prior to in vivo 2PEF imaging, isoflurane anesthesia was gradually decreased to zero, while urethane (U25000, Sigma; diluted in deionized water) was administered intraperitonealy over three injections (final dose: 1.5 g/kg rat). Urethane was used during our studies of changes in stimulus-induced neural response after microhemorrhage because it has been reported to both maintain regulation of cerebral blood flow [149] as well as preserve the neural response to a peripheral stimulus [124]. Throughout surgery and imaging animals breathed oxygen-enriched air, body temperature was maintained at 37.5 °C by a thermostatically regulated heating pad (Harvard Apparatus, Inc.), the blood oxygen saturation and heart rate were monitored using a pulse oximeter (MouseOx, Starr Life Sciences Corp.), and subcutaneous injections of 5% (w/v) glucose in physiological saline (1 ml/kg rat) were applied every hour. Animals were sacrificed at the conclusion of the imaging session.

5.3.2 Chronic Mouse Preparation with Reopenable Cranial Window

We used seven adult C57BL/6 mice (both sexes) ranging from 17 to 32 g in weight. Animals were anesthetized on isoflurane and eye ointment was applied. Next,

intramuscular injections of glycopyrrolate (0.5 mg/kg mouse) and subcutaneous injections of dexamethasone sodium phosphate (0.2 mg/kg mouse) (American Regent, Inc.) and ketoprofen (5 mg/kg mouse) (Fort Dodge) were given. The head was shaved and cleaned with providone iodine and ethanol. After giving local injections of bupivacaine, a ∼1.5 mm radius circular craniotomy was prepared over the hind paw somatosensory cortex (center located at 1.5 mm lateral and 0.3 mm rostral from bregma). The dura was left intact. During all procedures when the mouse was under anesthesia, body temperature was maintained at 37.5 °C by a thermostatically regulated heating pad and 0.1 mL subcutaneous injections of 5% (w/v) glucose in physiological saline were applied every hour. After loading fluorescent dyes into the brain, a thin ring-shaped wall of silicone (Kwik-sil, World Precision Instruments, Inc.) was carefully applied around the edge of the craniotomy and then over the exposed mouse skull. The craniotomy was filled with sterile ACSF and a 5 mm glass cover slip was glued to the silicone using cyanoacrylate and dental cement. This procedure created a chamber that can be removed while causing minimal injury to the brain by gently pulling the silicone away from the skull (figure 5.6A).

After closing the craniotomy, the animal was removed from anesthesia and allowed to recover for one hour. Animals were then re-anesthetized using isoflurane for in vivo 2PEF imaging and hemorrhage production. At the end of imaging session, the mouse was returned to a cage placed on a heating blanket and provided with wet food. We checked the window clarity and mouse behavior every eight hours until the next imaging session. Interruption of anesthesia for an hour between the surgery (2-3 hours) and the initial imaging session (4-6 hours) was found to improve the survival rate. On the next day, the mouse was re-anesthetized, the craniotomy was reopened, and fluorescent dyes were reapplied. The craniotomy

was then filled with sterile ACSF and sealed by gluing a glass coverslip directly to the skull. After the imaging session the animal was sacrificed.

Fluorescent Labeling of Blood Vessels, Astrocytes, and Neurons

Vasculature was labeled with intravenous injection of either 5% (w/v) tetramethylrhodamine isothiocyanatedextran (TRITC) (T1287, Sigma) for rats, or 5% (w/v) Texas Red dextran (D1864; Invitrogen) for mice, each dissolved in physiological saline. We bulk loaded Oregon Green BAPTA (OGB) (06807, Invitrogen) and sulforhodamine 101 (S7635, Sigma) into the hind paw somatosensory region of cortex according to protocols described previously [140, 108]. Briefly, OGB (5 μg) was dissolved in 5 μL solution of 20% pluronic F-127 (P2443, Sigma) in dimethyl sulfoxide (DMSO) (472301,Sigma), then 40 μL of sulforhodamine 101 (50 μM) in ACSF was added. The final solution was microinjected $\sim$300 μm beneath the surface of the brain using a Picospritzer (III, Parker Hannifin Corp.) in three different locations throughout the hind paw representation. OGB is a calcium-sensitive fluorescent dye that labeled all brain cells. Sulforhodamine 101, a red-emitting dye that labels only astrocytes, allowed neurons and astrocytes to be distinguished (figure 5.1B) [108].

5.3.3 Peripheral Stimulus

Electrical stimulation was applied via two 25 G needles inserted underneath the skin of the hind paw contralateral to the imaging region (figure 5.1A). Ten stimulation pulses of 0.5-s duration were applied with an interval of 10 s between successive stimuli. The stimulus current ($\sim$1 mA) was adjusted to elicit a slight movement in the toes of the paw. The average response from the 10 stimuli was used in all analysis.

5.3.4 In Vivo 2PEF Imaging

In vivo imaging was conducted on a locally-designed 2PEF microscope using an 850-nm, 87-MHz, 100-fs pulse train from a Ti:sapphire laser system (MIRA HP; Coherent) pumped by a continuous wave laser (Verdi-V18; Coherent) for excitation. Fluorescence emission was collected in two different channels separated by a 560-nm long-pass dichroic. When imaging rats, emission filters (Chroma, Inc.) transmitting wavelengths between 485 to 550 nm and 570 to 620 nm were used to collect green (OGB) and red fluorescence (sulforhodamine 101 and TRITC), respectively. For mouse imaging, the long wavelength filter was replaced by one that transmits from 610 to 680 nm to visualize sulforhodamine 101 and Texas Red. Although imaged on the same fluorescence channel, blood vessels and astrocytes were easily distinguished based on morphology and location. Laser scanning and data acquisition was controlled by MPScope software (Nguyen et al., 2006).

To create a map of the cortical vasculature and to localize the regions labeled by the dye injections, we acquired a stack of images of the entire cranial window (100 μm depth) using a 0.28 numerical aperture (NA), 4-magnification air objective (Olympus, Inc.). We changed to a 1.0-NA, 20-magnification water-immersion objective (Zeiss, Inc.) for high-resolution imaging. We acquired 256 x 256 pixel frames at a rate of 13 Hz when monitoring calcium transients and 512 x 512 pixel frames at a rate of 3.3 Hz for image stacks.

After selecting the target vessel to be ruptured (see below), we took a high-resolution stack of images centered at the hemorrhage site (figure 5.2B and figure 5.7B). Then we selected between seven and ten non-overlapping 150 μm x 150 μm sites that contained OGB-labeled neurons, located at different distances from the hemorrhage site and at a depth of 50 to 200 μm beneath the brain surface. We monitored stimulus-induced calcium transients at each of these locations (fig-

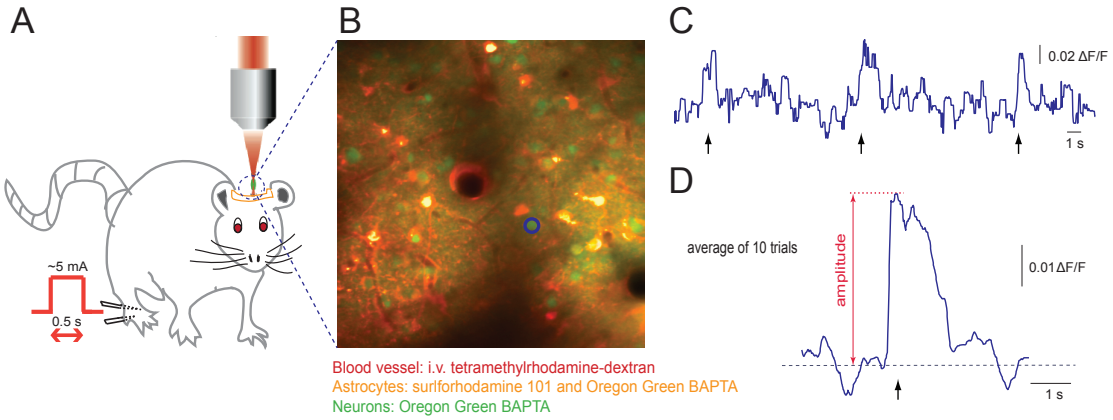

Figure 5.1: Two-photon imaging of stimulus-induced calcium transients in somatosensory cortex. A. Animals received an electrical stimulus to the hind paw while 2PEF microscopy was used to monitor changes in neural activity with calcium-sensitive dyes bulk loaded into the cortex. B. 2PEF image frame taken about 100 μm beneath the cortical surface in a rat. Blood vessels are labeled red (TRITC), neurons are green (OGB), and astrocytes are yellow (OGB and surlforhodamine 101). C. Calcium transients from the neuronal cell body circled in (B). Peripheral stimulus times are indicated by arrows. D. Average amplitude of the calcium transient across ten stimuli for the neuronal cell body circled in (B).

ure 5.3). We then induced a hemorrhage in the target vessel and repeated both the high-resolution image stack (figure 5.2C and figure 5.7B) and the calcium transient measurements at each site (∼30 minutes after the lesion, figure 5.3). In some rats, we repeated the measurement of stimulus-induced calcium transients at two and four hours after the microhemorrhage (figure 5.3). For the chronic experiments using mice we repeated these measurements one day after the lesion (figure 5.7).

5.3.5 Production of Targeted Microhemorrhages

To induce microhemorrhages, we injured the vessel wall of targeted penetrating arterioles using high intensity laser pulses (∼0.8-μJ, 800-nm, 1-kHz, 50-fs pulse train from a Ti:sapphire regenerative amplifier (Legend 1k USP; Coherent) pumped by a Q-switched laser (Evolution 15; Coherent) and seeded by a Ti:sapphire oscillator (ChinhookTi:sapphire laser; Kapteyn-Murnane Laboratories Inc; pumped by Verdi-V6; Coherent, Inc)) [110]. We focused these pulses onto the vessel wall of

penetrating arterioles between 100 and 200 μm beneath the brain surface (figure 5.2A). To induce a microhemorrhage, we first delivered 1 to 5 bursts of 100 pulses from the 1-kHz pulse train with an initial energy estimated to be below the threshold for causing vessel rupture ($\sim$100nJ at about 100 m depth)[110]. The pulse energy was then gradually increased, in 25% increments, until this irradiation lead to sufficient vessel wall damage to cause vessel rupture, allowing blood to push radially out into the brain (figure 5.2D). The vessel wall clotted within seconds after rupture, stopping the bleeding. The size of the red blood cell (RBC) filled hematoma (distinguished by dark cell-sized patches that pushed into the brain and excluded the blood plasma label) was quantified from image stacks taken within 15 minutes of producing the hemorrhage. In addition, in the mice we quantified the size of the region where fluorescently-labeled blood plasma penetrated into the brain. This was more difficult to quantify in rats because the TRITC used to label the blood plasma in these animals was not bright enough to reliably determine the limit of blood plasma penetration. One microhemorrhage was induced in each of fifteen rats and in four mice. In addition, we performed five (three) control experiments in rats (mice), in which the same imaging was performed but without the creation of a hemorrhage, as well as three sham experiments in rats, in which the vessel was targeted using laser pulse energies that were too low to rupture the vessel.

5.3.6 Analysis of Stimulus Evoked Calcium Transients

We implemented custom scripts in Matlab (The Mathworks, Inc.) that enabled us to compare the average amplitude of the calcium response of neuronal cell bodies and regions of neuropil at different time points. For each of the imaged sites, we manually selected neuronal cell bodies and regions of neuropil ($\sim$900 μm2)

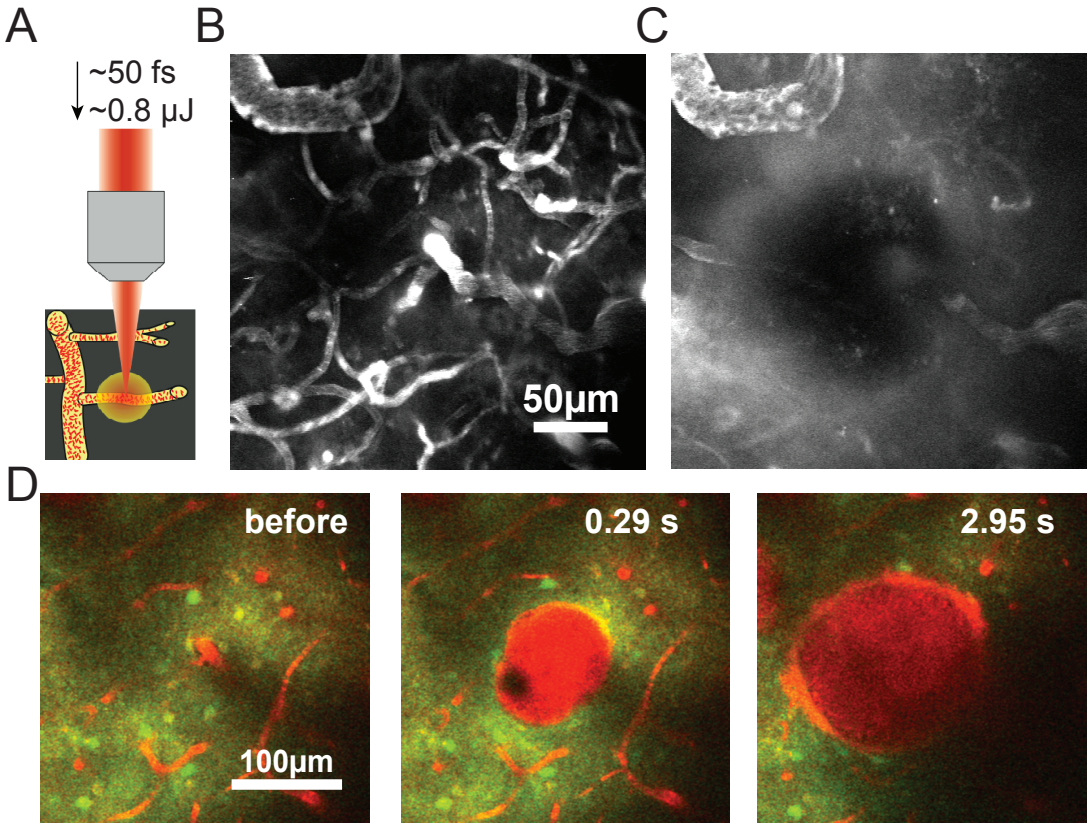

Figure 5.2: Induction of microhemorrhage with femtoseond laser irradiation. A. High energy, femtosecond laser pulses were tightly focused on the wall of the target vessel to rupture the vessel and initiate bleeding. B. Projection of 150-μm deep 2PEF image stack of fluorescently-labeled cortical blood vessels. C. Projection of a 2PEF image stack over the same volume as (B) after a hemorrhage was produced by rupturing the arteriole in the center of the frame. The RBC-filled hematoma core (in black) obstructed imaging, and fluorescently-labeled blood plasma was pushed into the surrounding parenchymal tissue. D. Time course of bleeding after rupturing a vessel about 100 μm beneath the cortical surface. Fluorescently-labeled blood plasma is red, while neurons are green and astrocytes yellow.

that could be identified at all time points before and after the microhemorrhage. For each stimulus, we calculated the normalized fluorescence change (dF/F_o) (figure 5.1C) over a 4 s window around the stimulus, where F_o was taken to be the mean of the lowest 50% of fluorescence values measured during the 10 s before the stimulus and dF was the instantaneous fluorescence, averaged across the neuronal cell body or region of neuropil, minus F_o [78]. This definition of F_o reduces the impact of slow changes in fluorescence due to power drifts or movement artifact. These responses were averaged across all ten stimuli and a moving median filter (50 samples wide) was applied (figure 5.1D). We calculated the amplitude of the averaged calcium response for each cell or region at each time point. We excluded all neuronal cell bodies or regions of neuropil that did not exhibit a stimulus-evoked response at baseline from further analysis. We computed the ratio of the post-hemorrhage (or control/sham) response amplitude to the baseline response for each cell or region. Finally, we classified cells as having a normal post-hemorrhage response amplitude if this ratio was greater than the mean minus one standard deviation of the ratios of control and sham data.

Post-mortem Histology

In three mice, we implanted a chronic cranial window [65] and, after one week of recovery, we triggered three to four microhemorrhages in penetrating arterioles, separated by at least 1 mm. Three days later animals were transcardially perfused with phosphate buffered saline (PBS, Sigma-Aldrich) followed by 4% (wt/vol) paraformaldehyde in PBS. The brain was extracted, soaked in first 30% (wt/vol) then 60% (wt/vol) sucrose in PBS for 24 hours each. Fiducial marks were placed with 30 G needle coated with black ink to indicate the edges of the cranial window and the location of individual microhemorrhages. The tissue was frozen and cut in 20-μm thick sections on a cryostat. Tissue sections were placed on Permafrost

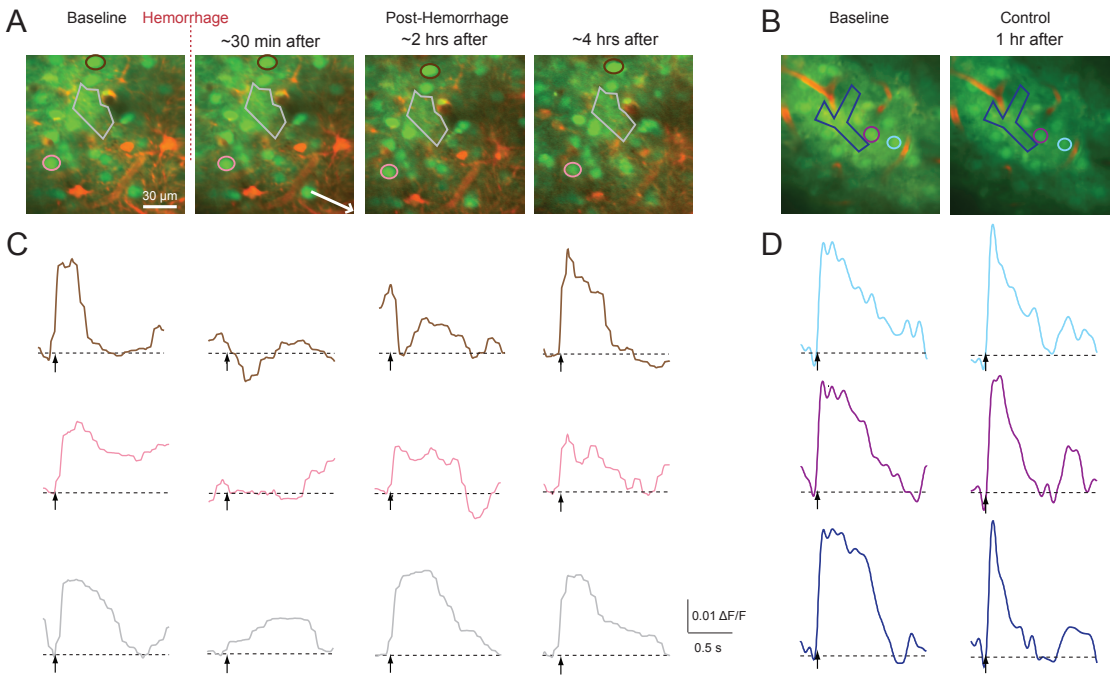

Figure 5.3: Changes in somatosensory calcium responses in neuronal cell bodies and regions of neuropil after a microhemorrhage. A. 2PEF images of cortex (120 μm beneath brain surface; same labeling as figure 1B) before and over time after a microhemorrhage. The arrow in the second panel indicates the direction to the microhemorrhage, located 200 μm away. B. Images from a control experiment. C. Stimulus-induced calcium responses from two neuronal cell bodies and one region of neuropil (indicated by color coded regions in (A)) before and over time after a microhemorrhage. D. Calcium responses from a control experiment.

slides (Superfrost Plus, Fisher Sci.), rehydrated with PBS, and stained with diaminobenzidine (DAB) (peroxidise substrate kit, SK-4100, Vector Labs, Inc.) to label red blood cells. To identify possible apoptotic cells, terminal deoxynucleotidyl transferase dUTP nick end labeling (TUNEL) was completed (11684795910, Roche Applied Scientific, Inc.). Briefly, sections were permeabilized in a 0.1% (wt/vol) Triton X-100, 0.1% (wt/vol) sodium citrate solution in a 4°C refrigerator for 5 min., then washed in PBS twice for 2 min. each, and treated with the TUNEL enzyme/labeling solution. The tissue sections were covered with aluminum foil to exclude light and incubated at 37°C for 3 hours. Sections were then rinsed in PBS twice for 3 min. each and imaged with an epifluorescence microscope. We checked for TUNEL-positive cells in sections that contained a microhemorrhage, as identified both by the location relative to the fiducial marks and the presence of DAB-positive red blood cells in the tissue.

Statistical Analysis

Moving medians of post-hemorrhage response amplitudes and the 95% confidence interval was obtained as a function of distance from the microhemorrhage using a moving window size of 35 and 45 samples for neuronal cell bodies (figure 5.4A) and regions of neuropil (figure 5.4C), respectively (1/10th of the total number of data points). The plots were further smoothed using a 20 sample moving average. Boxplots containing both control and sham data were produced for neurons (figure 5.4B) and neuropil (figure 5.4D), respectively. The edges of the box represent the first and third quartile of data, the red line across the box indicates the median and the whiskers extend to the maximum and minimum amplitude values that are not outliers. Individual data points are shown in green for control and in yellow for sham experiments (figure 5.4B and figure 5.4D).

Bar plots were used to compare the average post-hemorrhage response am-

plitude ratios at different times after the lesion and at different distances from the microhemorrhage (figure 5.5 and figure 5.7). Error bars represent the standard errors of mean. For these data, distributions were found to be non-normal (Shapiro-Wilk W test), so we used rank-based statistical analysis. We performed Wilcoxon signed-rank tests to determine if the response amplitude ratios were less than one.

5.4 Results

We investigated the response of somatosensory neuronal cell bodies and regions of neuropil to a peripheral stimulus using 2PEF imaging of calcium sensitive dyes (figure 5.1) before and after femtosecond laser-induced hemorrhage of a nearby microvessel (figure 5.2). The microhemorrhage consisted of a RBC-filled hematoma core of about 100 +/− 40 μm (mean +/− standard deviation) diameter, on average (18 hemorrhages in 18 rats; 19 hemorrhages in 10 mice). Surrounding this core was a 280 +/− 110 μm diameter region where fluorescently-labeled blood plasma pushed into the brain parenchyma (figure 5.2; 18 hemorrhages in 9 mice). The targeted vessel was observed to be flowing after each hemorrhage. We characterized the changes in stimulus-evoked neural activity as a function of distance from the microhemorrhage and as a function of time after the lesion (figure 5.3), up to one day later.

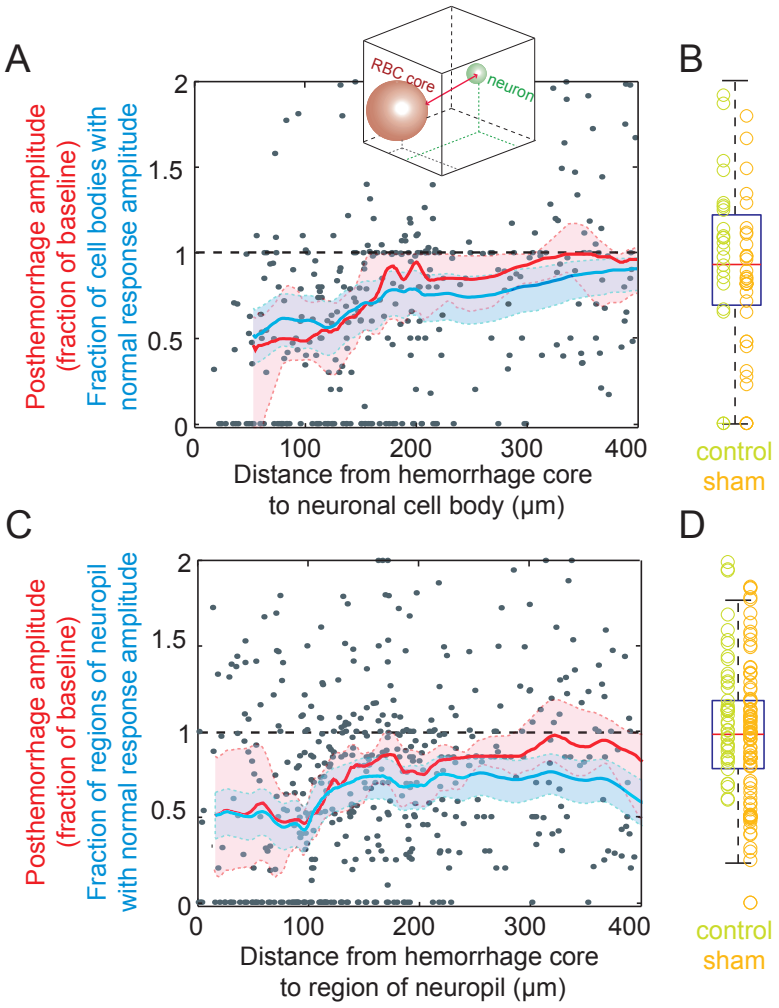

Figure 5.4: Post-hemorrhage neural response as a function of distance from the hematoma. A. Amplitude of the stimulus-induced calcium responses for neuronal cell bodies within 30 minutes after a microhemorrhage, expressed as a fraction of the baseline responses, for cells at different distances from the hematoma core. Grey points represent measurements from individual neuronal cell bodies, while the red line indicates a moving median of the response amplitude. The blue line represents the fraction of neuronal cell bodies that continued to respond normally to the peripheral stimulus after the microhemorrhage (i.e. with a response amplitude ratio that was greater than the mean minus one standard deviation of the amplitude ratio for control and sham data). The red and blue shaded regions represent 95% confidence intervals about the median response amplitude and fraction of cells normally responding, respectively. Distance is defined as the three-dimensional path from the edge of the spherical RBC-filled hematoma core to the center of the neuronal cell body (inset). B. Box plot of the amplitude of the calcium response from neuronal cell bodies, expressed as a fraction of the baseline response, for control and sham experiments. The measurements from individual cells are indicated with green (control) and orange (sham) circles. C. Amplitude of the stimulus-induced calcium responses for regions of neuropil within 30 minutes after a microhemorrhage, expressed as a fraction of the baseline responses, for regions at different distances from the hematoma core. D. Box plot of the amplitude of the calcium response from regions of neuropil, expressed as a fraction of the baseline response, for control and sham experiments.

5.4.1 Average Response Amplitude to a Peripheral Stimulus Decreased Immediately After a Microhemorrhage in Nearby Areas.

We found that within 30 minutes after a microhemorrhage in the acute rat preparation, the amplitude of the neural response either disappeared or decreased in most of the neuronal cell bodies and regions of neuropil located within 150 μm of the edge of the RBC-filled core of the microhemorrhage (figure 5.3 and figure 5.4). In this region, the average ratio of the response amplitude to the baseline response was 0.6 +/- 0.5 (mean +/- standard deviation) and 0.6 +/- 0.6 for neuronal cell bodies (figure 5.4A) and regions of neuropil (figure 5.4C), respectively. Both control and sham experiments showed no decrease in the average response amplitude of neuronal cell bodies (figure 5.4B) and regions of neuropil (figure 5.4D). Further from the microhemorrhage the immediate impact of the lesion on stimulus-evoked response amplitude was more modest, with only a minor decrease in activity from 150 to 300 μm from the RBC-filled hemorrhage core and no decrease in activity further than 300 μm (figure 5.4A and figure 5.4C). Further, we determined the fraction of neuronal cell bodies and regions of neuropil with a stimulus-evoked response amplitude that was similar to the response amplitude in controls (i.e. the post-hemorrhage response was greater than one standard deviation below the mean response in controls). We found that the fraction of neuronal cell bodies and regions of neuropil with normal response amplitude was lowest near the microhemorrhage and recovered with distance from the microhemorrhage with a similar trend to the post-hemorrhage response amplitudes (figure 5.4A and figure 5.4C).

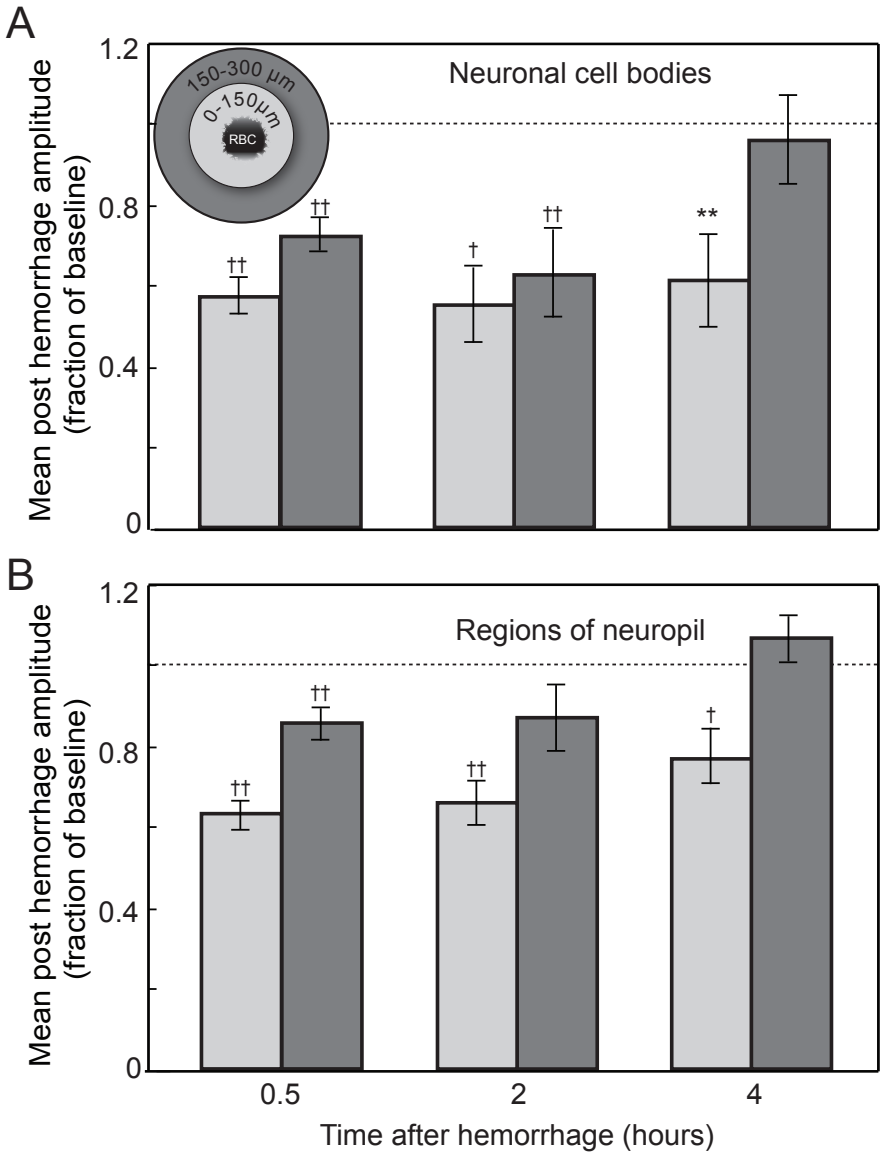

Figure 5.5: Changes in average neuronal response over hours after a microhemorrhage. A. Average of the post-hemorrhage stimulus-induced calcium response amplitudes, expressed as a fraction of the baseline response amplitudes, for neuronal cell bodies at 0.5, 2, and 4 hours after a microhemorrhage and for cells located either within 150 μm (light grey) or between 150 and 300 μm (dark grey) of the RBC-filled hematoma, as indicated in the inset. Error bars represent the standard error of the mean. Dashed line indicates a response amplitude after the microhemorrhage that is equal to the baseline response. B. Average response for regions of neuropil. Levels of significance for differences of the average amplitude ratios from one are indicated by: * $p < 0.05$, ** $p < 0.01$, $p < 0.001$, $p < 0.0001$ (Wilcoxon signed-rank test).

5.4.2 The Response to a Peripheral Stimulus Recovered Toward Baseline with Time After the Microhemorrhage

Over time, we observed a distance-dependent recovery of function in the neuronal cell bodies and regions of neuropil that showed a decreased response immediately after the microhemorrhage. In acute rat experiments, the response amplitude recovered to baseline values by four hours after the microhemorrhage at distances of 150 and 300 μm from the edge of the RBC-filled hematoma. In contrast, activity remained depressed within 150 μm (figure 5.5). Longer duration acute experiments were impractical due to the inability to maintain stable physiology during extended anesthesia.

To investigate whether or not neural response within 150 μm from microhemorrhage recovers over a longer time, we developed a chronic mouse preparation that enabled opening of the craniotomy for re-injection of calcium-sensitive dye (figure 5.6A). Using this preparation, we characterized stimulus-evoked calcium transients 24 hours after a microhemorrhage (figure 5.6B-D). Because of differences in the dye injection and the inclination of the imaging plane, we were able to successfully identify about 66% (62%) of the same neuronal cell bodies (astrocytes) one day after the microhemorrhage. Similarly, in control experiments we were able to identify 74% (66%) of the neuronal cell bodies (astrocytes) after one day. We found that responses in neuronal cell bodies and regions of neuropil within 150 μm of the hematoma recover to near baseline levels by 24 hours after the lesion (figure 5.7).

5.4.3 Microhemorrhages did not Induced Apoptosis in Nearby Brain Cells.

One possible explanation for finding only about two-thirds of the cells after the second calcium dye labeling in the chronic mouse experiments is death of neurons. To rule this out, we checked for apoptotic cells in the vicinity of the microhemorrhage. Across three mice, 12 microhemorrhages were produced in the cortex and seven of these were successfully identified in tissue sections collected three days after the lesion (figure 5.8A-B). We found no TUNEL-positive cells near the microhemorrhages (nor in any other cortical sections) (figure 5.8C and figure 5.8D). As a positive control, we included a section of mouse intestine with each batch of TUNEL staining and consistently observed apopototic epithelial cells (figure 5.8C, inset). In addition, we observed extensive TUNEL-positive cells in the penumbral region of a photothrombotic stroke [170] (data not shown).

5.5 Discussion

Although the presence of brain microhemorrhages have been correlated with cognitive decline in humans [21, 132], the lack of good animal models of microhemorrhage has prevented studies of the impact of these lesions on neural function. Such experiments are necessary to elucidate the mechanistic links between small brain bleeds and neurological dysfunction. Here, we used tightly-focused femtosecond laser pulses to rupture the wall of targeted arterioles located beneath the surface of the brain in rodents to model cortical microhemorrhages [110]. In vivo nonlinear microscopy was used to study changes in peripheral stimulus-induced calcium transients in individual neuronal cell bodies and regions of neuropil due to these microhemorrhages. We showed that neural function is interrupted near

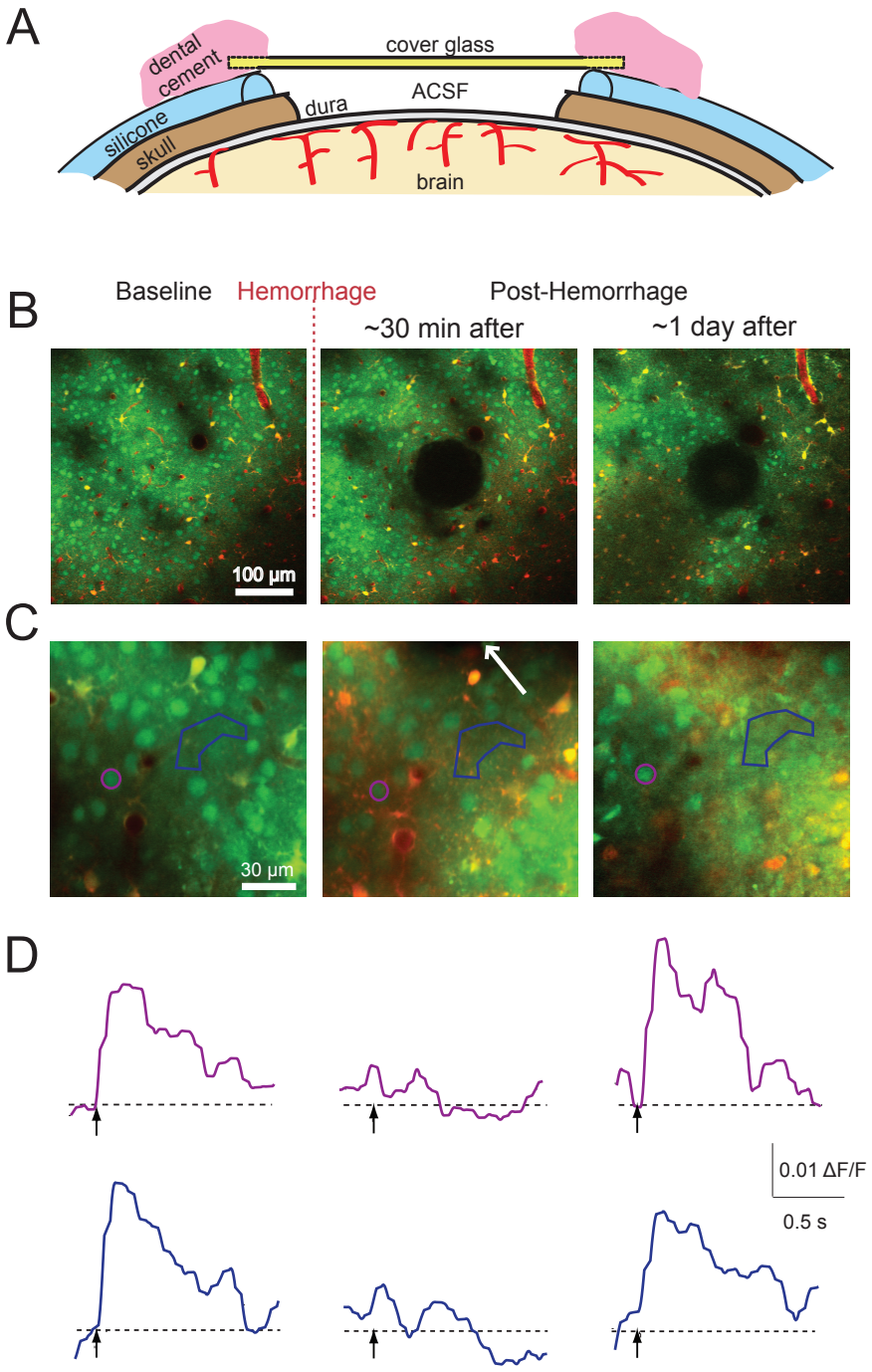

Figure 5.6: Chronic imaging of stimulus-induced calcium transients after a microhemorrhage. A. Schematic of a re-openable chronic cranial window preparation for mouse. A layer of silicone coated the skull around the craniotomy, and the glass was glued to the silicone. The window was reopened by gently detaching the silicone from the skull, enabling reinjection of OGB and sulforhodamine 101 into the cortex. B. Low- and C. high-magnification 2PEF images of the same regions of the brain before, immediately after, and one day after inducing a microhemorrhage. The hematoma is visible in the center of the second and third panels in (B). The arrow in the second panel of (C) indicates the direction to the microhemorrhage, located 40 μm away. D. Stimulus-induced calcium responses from the neuronal cell body and region of neuropil indicated on panel (C) by color coding.

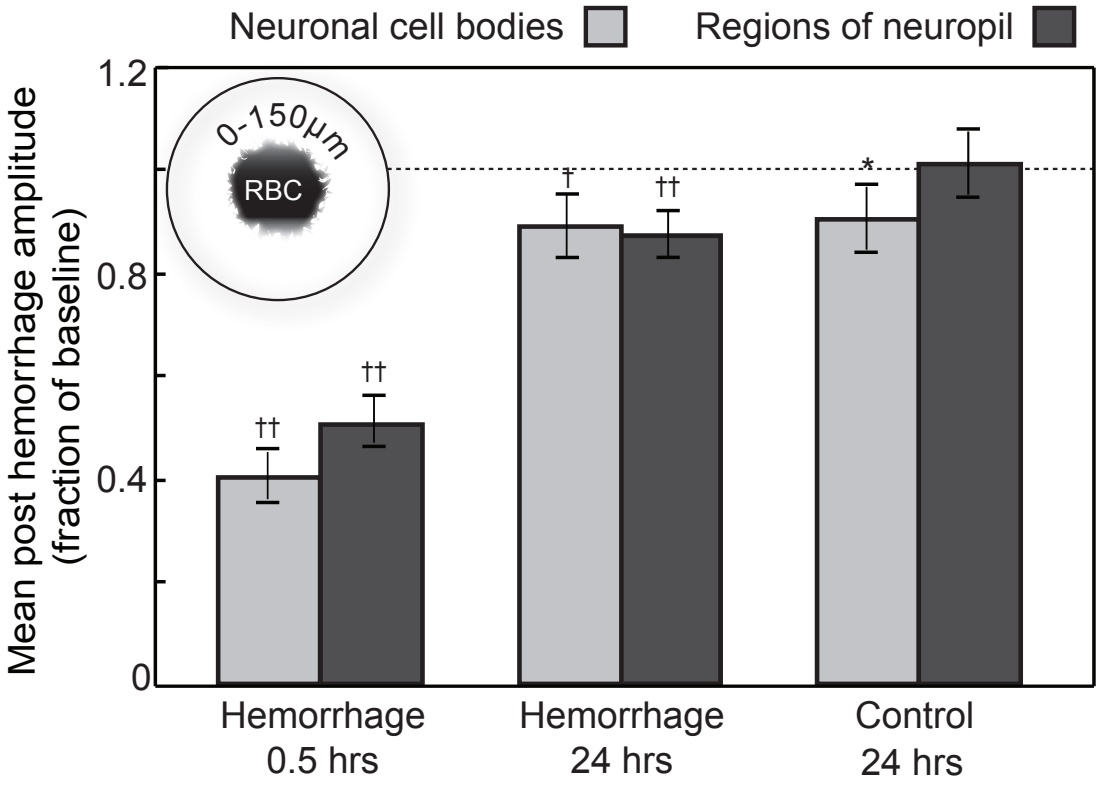

Figure 5.7: Changes in average neuronal response over one day after a microhemorrhage. Average of the post-hemorrhage stimulus-induced calcium response amplitudes, expressed as a fraction of the baseline response amplitudes, at 0.5 and 24 hours after a microhemorrhage (and for controls at 24 hours) for neuronal cell bodies (light grey) and regions of neuropil (dark grey) located within 150 μm of the RBC-filled hematoma, as indicated in the inset. Error bars represent the standard error of the mean. Dashed line indicates a response amplitude after the microhemorrhage that is equal to the baseline response. Levels of significance for differences of the average amplitude ratios from one are indicated by: $*$ $p < 0.05$, $**$ $p < 0.01$, † $p < 0.001$, †† $p < 0.0001$ (Wilcoxon signed-rank test).

the microhemorrhage, but recovers over time after the lesion. Recovery occurred in a distance-dependent manner, with regions closest to the hematoma taking the longest to regain function. These studies provide the first insight into the spatial extent and time course of neural dysfunction (and recovery) after brain microhemorrhage.

In the acute experiments in rats, we followed changes in the response of each individual neuronal cell body and region of neuropil up to four hours after the microhemorrhage. For the chronic experiments in mice, however, we were only

able to identify about two-thirds of the same cells on the second day of imaging, leaving open the possibility that some cells died as a result of the lesion. However, our data suggest this is unlikely because we were able to identify approximately the same number of cells on the second day of imaging in control experiments as after a microhemorrhage. Several factors may contribute to our inability to identify all of the same cells on the second day of imaging. First, the dye injection locations varied slightly between days, potentially leading to differences in which cells were labeled. Second, activated microglia and other inflammatory cells are likely present in the vicinity of the microhemorrhage one day after the lesion [27, 36, 132] and these cells may either scavenge the calcium dye or otherwise interfere with the bulk loading process. Finally, although we consistently identified the same region of brain tissue, we often found small differences in the inclination of the imaging plane due to differences in the mouse position in the stereotax between the two days of imaging. This difference in inclination leads to different cells intersecting the image plane at the edges of the frame, reducing our ability to find the same cells on both days. Further, we found no evidence of apoptotic cells in the vicinity of the microhemorrhage using histology. To give time for cells potentially affected by the microhemorrhage to progress along the apoptotic pathway and thus register as TUNEL positive, the staining was conducted at three days after the lesion. Taken together, this data suggest that the recovery in neural response seen one day after the microhemorrhage is not due to the death of the lowest-responding neurons and preservation of less affected ones, but rather that all neurons recover the ability to respond to a peripheral stimulus within one day after the microhemorrhage.

The impact of bleeding from a brain blood vessel on neural health and function depends critically on the size of the hematoma that is formed. Large intracerebral hemorrhages lead to widespread cell death and are associated with high rates of

mortality and morbidity in patients [8, 121]. This cell death is caused by several factors, including elevations in intracerebral pressure that could cause direct cell injury and crush blood vessels causing ischemia [121], excitotoxic damage from the high levels of glutamate or neurotoxic effects of other blood products, such as thrombin, that enter the brain parenchyma [11, 77, 121, 161], negative effects of the inflammation triggered by the hemorrhage [48, 175, 168], and damage from reactive oxygen species, such as those released by lysed red blood cells a few days after the lesion [121, 163].

The cognitive impact of the microbleeds identified in MRI imaging in patients remains controversial, with some studies reporting minimal effects [38, 125], and others [132, 171, 177] finding an association between microbleeds and cognitive dysfunction. Microbleeds are a frequent consequence of cerebral amyloid angiopathy, and it has been suggested that they may contribute to the cognitive decline in Alzheimers patients[117, 19, 132, 21]. Additionally, the presence of brain microbleeds has been associated with more severe cognitive impacts after head trauma [131]. For these smaller bleeds, many of the mechanisms that lead to cell injury for large hematomas may not play a significant role. For example, there is not a significant increase in intracranial pressure. Post-mortem studies of microbleeds in humans have revealed significant inflammation near the lesion. While there are limited studies of necrotic or apoptotic cell death after microbleeds, the current data suggest that cell death is not widespread.

For the smallest hemorrhages, few clinical studies are available. The presence of microhemorrhages (diameter < 200 μm) is common in advanced Alzheimers disease patients and is correlated with more severe amyloid pathology [21, 132], suggesting a potential link between microhemorrhages and cognitive decline. In patients with CADASIL, there is clear evidence of cognitive dysfunction [89], al-

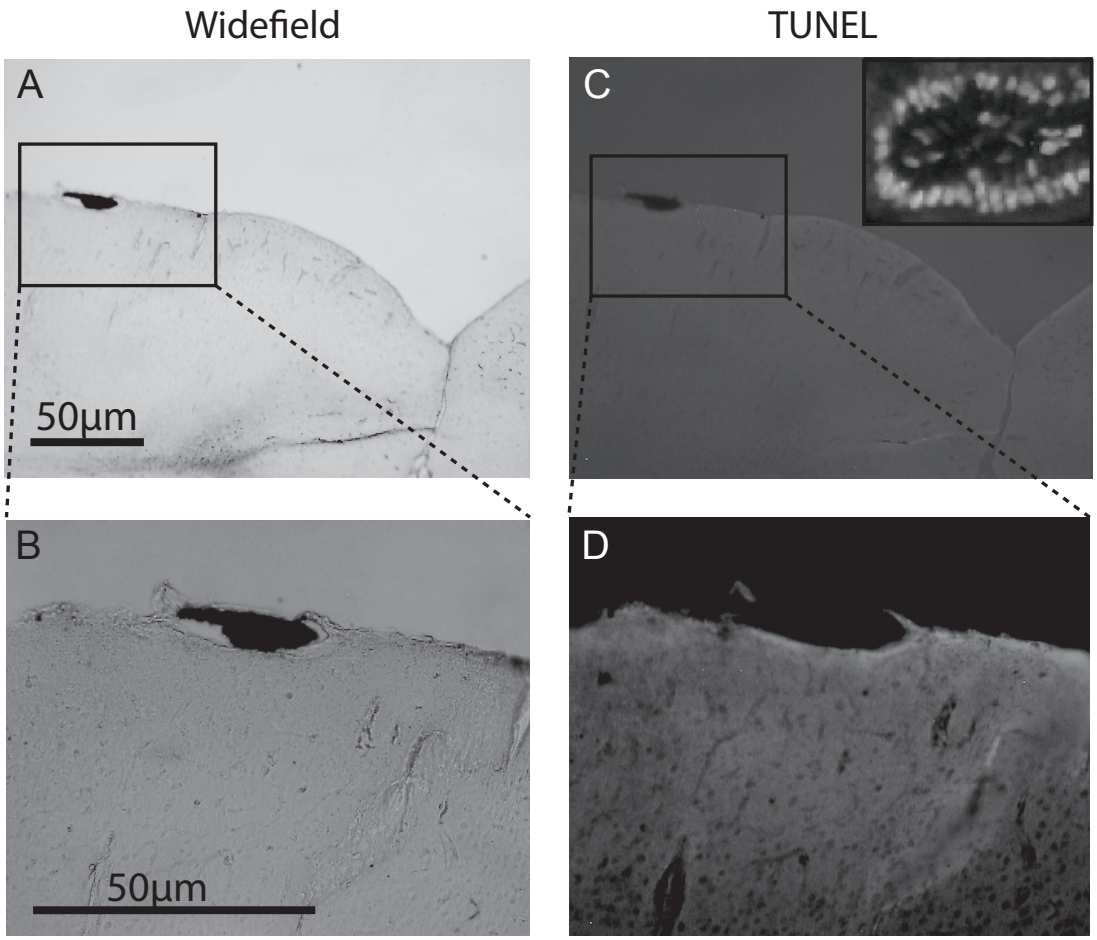

Figure 5.8: Postmortem histology of tissue near microhemorrhages. A. Low- and B. high-magnification widefield images of a tissue section containing a RBC-filled hematoma near the brain surface. RBCs are stained with DAB. C. Low- and D. high-magnification fluorescence images for TUNEL labeling in the same tissue section as in (A) and (B). No TUNEL-positive cells were found. The inset in (C) shows TUNEL-positive epithelial cells from a section of intestine (same scale bar as show in (A)).

though multiple different kinds of brain pathologies in addition to microhemorrhages, such as lacunar infarcts and diffuse white matter changes, are found in these patients [27]. For microhemorrhages, there are signs of inflammation near the lesion, including activation of astrocyte and microglia [165] and invasion of neutrophils and macrophages [27, 36, 132], but no reports have shown evidence of cell death, although the there are only limited studies of these small lesions to date. For these small hemorrhages, it is likely that the amount of blood that enters the brain is small enough that phagocytotic cells and other mechanisms can clean the cellular environment before significant injury is caused. The work we present here suggests that these microhemorrhages do, however, lead to a transient loss of neural function within a few hundred micrometers from the lesion, but that this function largely recovers over time.

Most likely, the transient loss of neural function we observed is caused by the infusion of blood plasma into the intracellular space in the brain. This leads to changes in ion balances and extracellular messengers and to increases in reactive oxygen species, all of which may interfere with the ability of neurons to normally receive synaptic input and fire action potentials. Interestingly, the few hundred micrometer spatial extent of the most severe disruption of neural function we observed correlates well with the distance that blood plasma penetrates into the parenchymal tissue in this microhemorrhage model. The less severe impact and more rapid recovery of neural function in regions further from the microhemorrhage is consistent with a gradient in concentration of blood plasma products that cause dysfunction in the brain tissue.

In this study, we did not investigate the impact of the microhemorrhage on the few neurons that were immediately adjacent to the target vessel (within $\sim$50 μm). These cells were likely displaced by the expanding hematoma or surrounded by

red blood cells. Measurement of calcium transients from these cells was not easily achieved and so we cannot rule out the possibility that these cells are permanently dysfunctional. The lack of apoptotic cells in our histology study, however, suggests that these cells do not die. We also cannot rule out the possibility that lysis of red blood cells a few days after the microhemorrahge leads to additional injury that could compromise neural function later.

The short-term loss of neural function we observed here may not be completely benign. Neurons with decreased input and firing rates may gain and lose synapses at an elevated rate due to homeostatic mechanisms that seek to maintain neural input and firing rate, thereby causing potentially aberrant rewiring of neural circuits. In addition, these hemorrhages may have a more severe impact on neural health and function if combined with disease backgrounds such as hypertension, Alzheimers disease, or if they occur in aged brain. The microhemorrhages we studied were all in cortex, and these lesions may have a different effect in other brain locations.

Recent data has suggested that occlusion of single penetrating arterioles (the same class of vessel that we targeted to produce microhemorrhages) leads to cell death over a several hundred micrometer region [136]. This data suggests, at a minimum, that small hemorrhages have a less severe impact than occlusion of the same class of vessel, implying that clinical management of patients with cardiovascular risk factors may benefit from aggressive anticoagulation even with added risk of bleeding from small vessels.

CHAPTER 6

THE ANTICIPATORY CONTROL OF MOTION-TO-FORCE TRANSITIONS WITH THE FINGERTIPS ADAPTS OPTIMALLY TO TASK DIFFICULTY

The data on this chapter was originally published in the following manuscript: Flor A. Cianchetti, Francisco J. Valero-Cuevas. **Anticipatory control of motion-to-force transitions with the fingertips adapts optimally to task difficulty.** Journal of Neurophysiology 2010. 103(1):108-16.

6.1 Abstract

Moving our fingertips towards objects to produce well-directed forces immediately upon contact is fundamental to dexterous manipulation. This apparently simple motion-to-force transition in fact involves a time-critical, predictive switch in control strategy [156, 157]. Given that dexterous manipulation must accommodate multiple mechanical conditions, we investigated whether and how this transition adapts to task difficulty. Eight adults (19 to 39 years old) produced ramps of isometric vertical fingertip force against a rigid surface immediately following a tapping motion. By changing target surface friction and size we defined an easier (sandpaper, 11 mm in diameter) vs. a more difficult (polished steel, 5 mm in diameter) task. As in prior work, we assembled fine-wire electromyograms from all seven muscles of the index finger into a 7-dimensional vector defining the full muscle coordination patternand quantified its temporal evolution as its alignment with a reference coordination pattern vector for steady-state force production. As predicted by numerical optimizations to neuromuscular delays [157], our empirical and sigmoidal nonlinear regression analyses show that the coordination pattern transitions begin sooner for the more difficult tasks than for the easier tasks ($\sim$120 ms $p < 0.02$ and $\sim$115 ms $p< 0.015$, respectively); and that the coordination pattern transition in alignment is well represented by a sigmoidal trend ($R^2 >0.7$ in most cases). Importantly, the force vector following contact had smaller directional error ($p< 0.02$) for the more difficult task even though the transition in coordination pattern was less stereotypical and uniform than for the easier task. These adaptations of transition strategy to task difficulty are compatible with an optimization to counteract neuromuscular delays and noise to enable this fundamental element of dexterous manipulation.

6.2 Introduction

Dexterous manipulation often requires us to rapidly make contact with objects to produce well-directed fingertip force vectors. For example, quickly grasping small, round or fragile objects like wine glasses, beads, berries, etc. all involve transitioning abruptly from moving the fingertip towards a rigid surface to producing a well-directed fingertip force vector against it. From a mechanical perspective this commonplace task is extremely challenging because the control for accurate finger motion is incompatible with that for well-directed static force. Several authors (e.g., [64, 156, 172]) have demonstrated that this switch in control strategy is unavoidably sensitive to time-delays and errors in planning. In biological systems this control challenge is exacerbated by the inability of the neuromuscular system to switch control strategies and muscle contractions instantaneously or exactly.

Recently we showed that the human nervous system performs this abrupt switch in control strategy via an anticipatory, time-critical, and neurally demanding transition of muscle activations before contact (i.e., from those controlling finger motion to those controlling fingertip force) [156]. In addition to ruling out a passive impedance based strategy to mediate the contact with the surface, we found that the muscle coordination pattern clearly transitions from that for motion to that for isometric force ca. 65 ms before contact. We then used mathematical modeling and analysis to reveal a switch in the underlying control strategy. Importantly, time delays due to muscle activation-contraction dynamics suffice to impose a physical limit on directional accuracy of the fingertip force vector upon contact.

Subsequent numerical simulations [157] show that an anticipatory transition in joint torques (analogous to that seen experimentally for muscle activations) is a necessary control strategy to reach the physical limits of the directional accuracy of force production upon contact. This anticipatory strategy arises in our deter-

ministic model as a means to compensate for neuromuscular time-delays, and not from optimizing for robustness to noise/uncertainties. Importantly, the model also shows that advancing the onset of the transition in joint torques is an optimal response to increased task difficulty (e.g., small, round and fragile objects that are wet vs. dry or rough vs. slippery).

Given the stringent mechanical requirements of the motion-to-force transition, the delays and noise of the neuromuscular system, and the predicted temporal modulation with task difficulty, we hypothesized that the nervous system will adapt the onset of the transition of muscle coordination patterns to task difficulty. We defined the difficulty of the motion-to-force transition by the size and coefficient of friction of the target surface as either easier (rough-large: a high friction, larger diameter target) or more difficult (smooth-small: a low friction, smaller diameter target).

6.3 Methods

The experimental methods are the same as in [156], where the reader can find complete details. In this abridged description we focus on how we varied the difficulty of the task by changing the coefficient of friction and size of the target surface, and on the novel analysis methods.

6.3.1 Experiment

The task consisted of ramping up a fingertip force to a self-selected high magnitude ($\sim$100% MVC) against a flat horizontal target surface after approaching the surface with a downward motion (figure 6.1A). That is, subjects performed an abrupt transition from the production of downward motion with their fingertip

towards the target surface, followed by the production of a large downward static force. Subjects tapped the horizontal surface of two cylindrical pedestals: smooth (polished steel) and small (5 mm diameter) vs. rough (360-grit sandpaper) and large (11 mm diameter). The pedestal was mounted on a 6-axis load cell (model 20E12A-I25, JR3 Inc., Woodland, CA) with a force resolution of 0.01 N. Subjects wore a custom-molded thermoplastic (MaxD, North Coast Medical, Morgan Hill, CA) thimble with a spherical, 4.8 mm diameter, Teflon bead embedded on its distal aspect. This thimble rigorously defined the mechanical task via a unique contact point and friction cone for force direction [150, 153, 156]. The task was performed by eight consenting right handed individuals (avg. age 22.8 yrs range 19-39 yrs.) with no history of neurological or hand pathology or injury. They all read and signed a consent form for this protocol approved by Cornell Universitys Committee on Human Subjects. Two sessions were run on separate days. In the first session, the experimental set-up was adjusted to the dimensions of the subjects hand and the subject became acquainted with and practiced the task. In the second session fingertip force in the three directions and fine-wire EMG were recorded (2000 samples/s) from all muscles of the index finger while performing the task. Fine-wire intramuscular electrodes were placed in the seven muscles of the index finger using previously reported techniques [150, 153, 156]. The muscles of the index finger are: flexor digitorum profundus (FDP), flexor digitorum superficialis (FDS), extensor indicis proprius (EI), extensor digitorum communis (EC), first lumbrical (LUM), first dorsal interosseous (DI), and first palmar interosseous (PI).

Each subject produced three trials per target surface, each of which consisted of 4 brief, preparatory taps, followed by a tap-ramp-and-hold task (figure 6.1 only shows the last tap). We instructed the subjects to ramp-up the magnitude of the

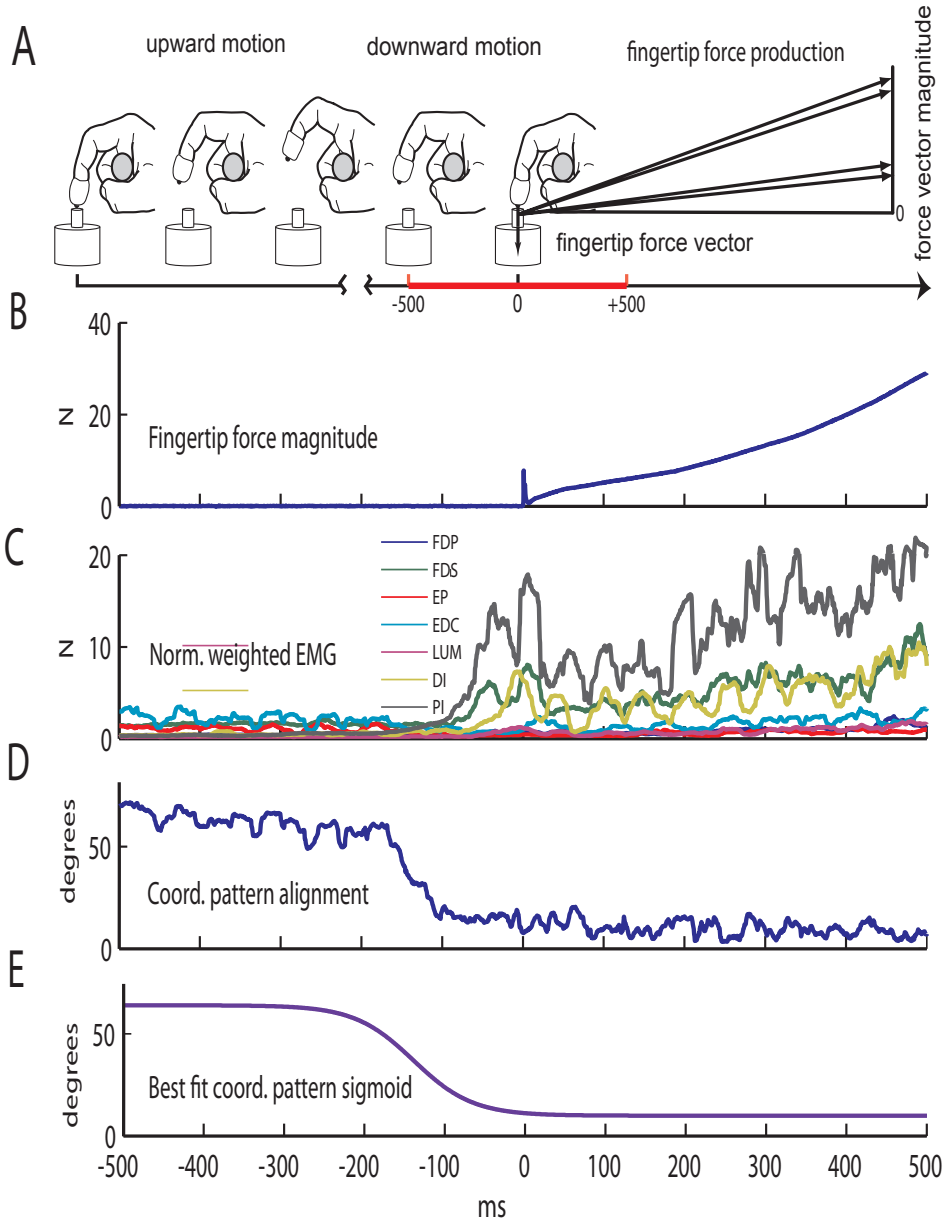

Figure 6.1: Description of experiment. A. Description of the task, following 4 brief preparatory taps over a specified target, the subject executed a last tap where after making contact with the target, the subject ramped up the vertical force applied by his finger to a maximum. The figure shows this last tap. The time of interest was 500 ms before and after contact (red in the time axis). The subject is wearing a custom thimble during the taps, the thimble allowed a unique contact point and friction cone for force direction. B. Fingertip force in the three directions was recorded while performing the task; the figure shows the vertical force magnitude for one trial 500 ms before and after contact. C. Fine-wire EMG from the seven muscles of the index finger was recorded while performing the task. Normalized weighted EMG is obtained after being filtered, full-wave rectified, normalized (by MVC), weighted (by physiological cross sectional areas) and smoothed (50 ms symmetric moving average) the EMG signals. D. The norm weighted EMG for each of the muscles, constitute a component of the muscle coordination pattern 7D vector ($\underline{m}(t)$)The coordination pattern alignment is the angle between the $\underline{m}(t)$ for each interval of time (-500 ms to 500 ms) and the $\underline{m}(t)$ at the time when the vertical force reached its maximum value. E. The best fit that described the evolution of the coordination pattern alignment during the transition from motion to force is a sigmoid.

fingertip force against the surface as quickly as possible, trying the best they could to keep the finger still and the direction of the force vertical. To enable natural task performance, we did not provide direct visual feedback of force magnitude or direction. In our experience and that of others [15] young adults are quite adept at directing forces perpendicular to the surface even in the absence of direct feedback about vector direction. Each trial was followed by a mandatory 30 sec rest period to avoid fatigue. To mitigate learning effects, if any, we randomized the surface used. After the experiments were over, we reviewed the force and motion plots of each trial and discarded those where the subjects either slipped while producing the force; did not produce a uniformly ascending force ramp; or prolonged their last tap and left less than 450 ms to complete tapping motion. The final data consisted of 30 trials, 16 using the smooth-small target and 14 using the rough-large target.

6.3.2 Analysis

As in our prior work, we characterized the muscle coordination pattern ($\underline{m}$(t)) as the time-varying 7-D unit vector of muscle forces estimated from the filtered (band-pass 100Hz to 1000 Hz), and then full-wave rectified, normalized (by MVC), weighted (by physiological cross sectional areas) and smoothed (50 ms symmetric moving average) EMG signals (figure 6.1C), as in [150, 157]. The temporal evolution of the coordination pattern vectors for each trial was quantified by the angle of alignment (θ(t)) of their unit vectors ($\underline{m}$(t)) with respect to the unit vector of the reference coordination pattern ($\underline{m}_{ref}$) defined during 80 ms of peak force for each trial, which occurred roughly 400 ms after contact with the surface [157]. Figure 6.1D shows the evolution of the alignment of one such unit vector from -500 to $+500$ ms before and after contact, respectively, for a sample trial. The onset of force (t=0) was defined at the beginning of the impact spike (figure 6.1B).

We excluded the first 10 ms of data after the onset of force from our analysis because unavoidable high-frequency impact transients in the force sensor polluted the measurement of the force vector magnitude and direction. A perfect alignment $\theta(\mathrm{t}) = 0$ means that the relative activations among muscles are the same as $\underline{m}_{ref}$, thus the same muscle coordination pattern is being used at those two time periods. Likewise, the greater the misalignment $\theta(\mathrm{t}) > 0$, the greater the differences in the muscle coordination patterns being used at those two time periods. Figure 6.2 shows a schematic vector representation of the muscle coordination pattern alignment during 3 different intervals (before contact, after contact, reference) for a 3 dimensional muscle coordination pattern, i.e., if the system only had 3 muscles. From the figure it is observed that the angle between the average unit vector during time interval B and the average unit vector during the reference interval is small compared with the angle between the average unit vectors in the A and reference intervals.

We used both non-parametric (i.e., empirical) and parametric (i.e., nonlinear regression) methods to test for differences in the evolution of coordination pattern alignment across the two levels of difficulty. In this way we guard ourselves against the possibility that apparent differences between tasks may simply reflect the fact that the nonlinear regression is a better model for one dataset than the other. As we present in the results, we find that the results from both analyses agree. For the empirical method we plotted the mean subject data, both raw and low-pass filtered (using a 50 ms symmetrical moving average), as subjects transitioned from producing motion to producing static force in the two levels of difficulty. The second method was to perform least-squares fitting to sigmoids, or logistic regression curves, to the coordination pattern alignment data, $\theta(\mathrm{t})$, because sigmoids are appropriate functions to characterize the general trend for a smooth transition

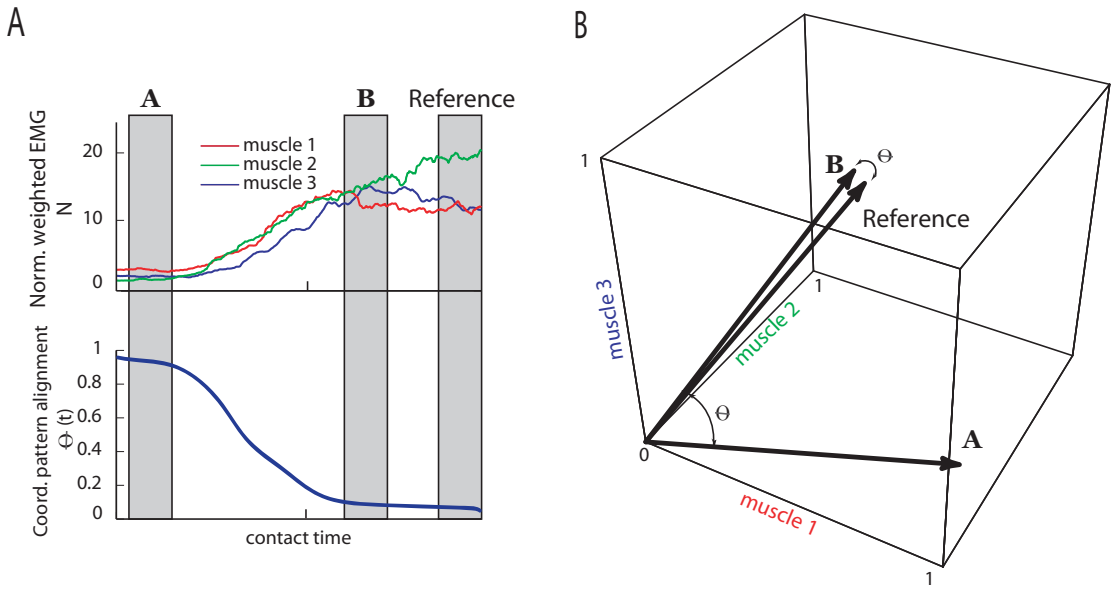

Figure 6.2: Vectorial representation of the coordination pattern. A. Normalized weighted EMG signals from three muscles and its coordination pattern alignment during transition from motion to force. In gray we emphasize 3 specific times (A, B, reference). B. The coordination pattern vectors ($\underline{m}(t)$) for these 3 specific times (A, B, reference). Measuring the alignment between vectors ($\theta(t)$) allows us to make quantitative comparisons, the coordination pattern at time A is further away from the reference than the coordination pattern is at time B. The 3D space is defined by each of the muscles where the EMG signal was acquired.

between two states. Our prior work shows that the nature of our angle time histories (the motor command as represented by the EMG and its analysis) indeed reveals a smooth transition between two states [156], figure 6.1D. Note that we do not mean to imply that the nervous system follows a sigmoidal trend in its latent command to the exclusion of other possible trends, or that the transition of the latent command signal is a sigmoid. We do mean, however, that a sigmoid is an appropriate choice when describing the simple general trend of the motor command when transitioning between two states.

We used MATLAB (Natick, MA) to fit a sigmoid of the following form to the $\theta(t)$ data: $\hat{\theta}(t) = a\frac{1+ue^{-t/\tau}}{1-ve^{-t/\tau}} \quad u, v > 0$

This characterizes the temporal transition of the relative angle between muscle coordination pattern from -500 ms and +500 ms with respect to the contact time.

The initial angle θ between the unit vectors $\underline{m}$(t) and $\underline{m}_{ref}$ is a$\frac{u}{v}$ (i.e., the initial asymptote early in the finger movement) and is the final angle θ between $\underline{m}$(t) with $\underline{m}_{ref}$. (i.e., final asymptote reached during steady state static fingertip force production occurring roughly 400 ms after contact). $\hat{\theta}(t)$ is the best fit to the θ(t) data. After fitting the sigmoid function to each trial, we normalized the sigmoid functions to have initial and final asymptotes of 1 and 0, allowing us to compare the trends in the transitions of muscle coordination pattern across subjects, trials, and levels of difficulty.

We also analyzed the magnitudes of coordination pattern vectors $\underline{m}$(t) during the abrupt transition from motion to force, calculated as the Euclidean norm:

$$|m(t)| = \sqrt{EMG_{FDP}{}^2 + EMG_{FDS}{}^2 + EMG_{EI}{}^2 + EMG_{EC}{}^2 + EMG_{LUM}{}^2 + EMG_{DI}{}^2 + EMG_{PI}{}^2}$$

We did not fit sigmoids to these vector magnitude data because they do not asymptote within the first 500 ms after contact, and thus cannot be represented as switching between two states.

The accuracy of fingertip force production upon contact was quantified by the angular deviation of the force vector from the surface normal (ϕ(t)=0). After low-pass filtering (80 Hz cut-off, 10th order Butterworth digital filter) the force data, the angular deviation of the force vector, ϕ (t), was obtained by the negative arc tangent of the square root of the squares of the force component parallel to the sensor surface (x and y) divided by the normal component (z); $\phi(t) = \arctan \frac{\sqrt{fx^2+fy^2}}{|f_z|}$

We performed a 2 way ANOVA test with subject as a random effect to determine whether task difficulty affects the quality of the fingertip force assessed by the average ϕ from 10 ms to 500 ms and ϕ at 65 ms after contact.

6.4 Results

As in our prior work [157], transitioning between the production of motion to the production of force is accompanied by a transition in muscle coordination patterns ($\underline{m}$(t)), as shown by changes in the alignment of the coordination pattern unit vector, θ(t). Figures 6.3A and B show the changes in alignment and magnitude of the coordination pattern vectors for one representative trial for both task difficulties. Figure 6.3A also contains the best-fit sigmoids that model the alignment data. Figure 6.3C-D show the alignment and magnitude after the data from figure 6.3A-B was normalized and smoothed by a 50 ms wide moving average. Normalization was done in each trial by making the mean of the first and last 200 ms be initial and final values. The normalized θ(t) began at one and ended at zero, and the normalized force magnitudes started at zero and ended at one. Then, we compared across different trials and conditions because the empirical plots had similar start and final values. Figure 6.4A-B shows the average alignment ±SE and average magnitude ±SE transitions (after being normalized and smoothed) from all subjects for each condition.

Figures 6.3 and 6.4 show empirically that the transition of both alignment and magnitude differs across task difficulty (smooth-small or rough-large conditions). We see that switching in magnitude and alignment for the small-smooth condition occurs earlier. For the alignment we found a significant difference in the time of onset between the two conditions (p=0.02), with an average onset value of -330 ms for the smooth-small case and -210 ms for the rough-large case. However, interpreting these empirical trends in alignment can be of limited value because of the naturally high variability of the EMG signals. Fitting a sigmoid to each of the trials (as in figure 6.3A) is arguably a better descriptor of the transition because it captures the general trend. Echoing the empirical trends, we see that

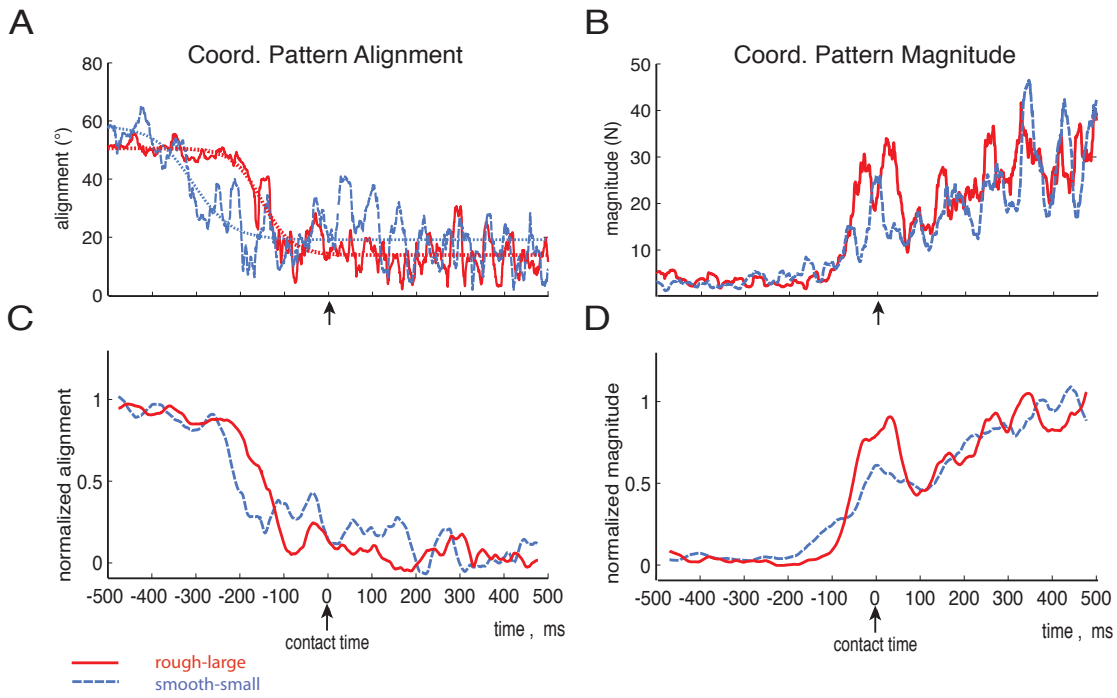

Figure 6.3: Coordination pattern alignment and magnitude of a representative subject. A. Coordination pattern alignment and their sigmoidal fits during transition from motion to force where the surface of contact was either smooth-small (dashed-blue) or rough-large (in red). B. Coordination pattern magnitude during transition from motion to force where the surface of contact was smooth-small (dashed, blue) or rough-large (in red). C. Same as in A after the coordination pattern alignment was normalized and smoothed by a moving average of 50 ms. D. Same as in B after the coordination pattern alignment was normalized and smoothed by a moving average of 50 ms.

the majority of the sigmoids for the more difficult condition have an early onset, whereas only 3 sigmoids do so for the easier condition. Figure 6.5 shows the fitted normalized sigmoids to all alignment trials color-coded by subject: figure 6.5A for a rough-large surface and figure 6.5B for a smooth-small surface. Figure 6.6 shows the transition in alignment for both conditions after averaging across trials ±SE. Averaging the normalized trends for each condition shows that the transition in muscle coordination pattern alignment for the smooth-small case begins ∼115 ms earlier than for the rough-large case (figure 6.4A, figure 6.6). We defined the onset of the transition in coordination pattern alignment when the global mean for all cases drop 20 % from the normalized value of 1 (see horizontal dashed lines in

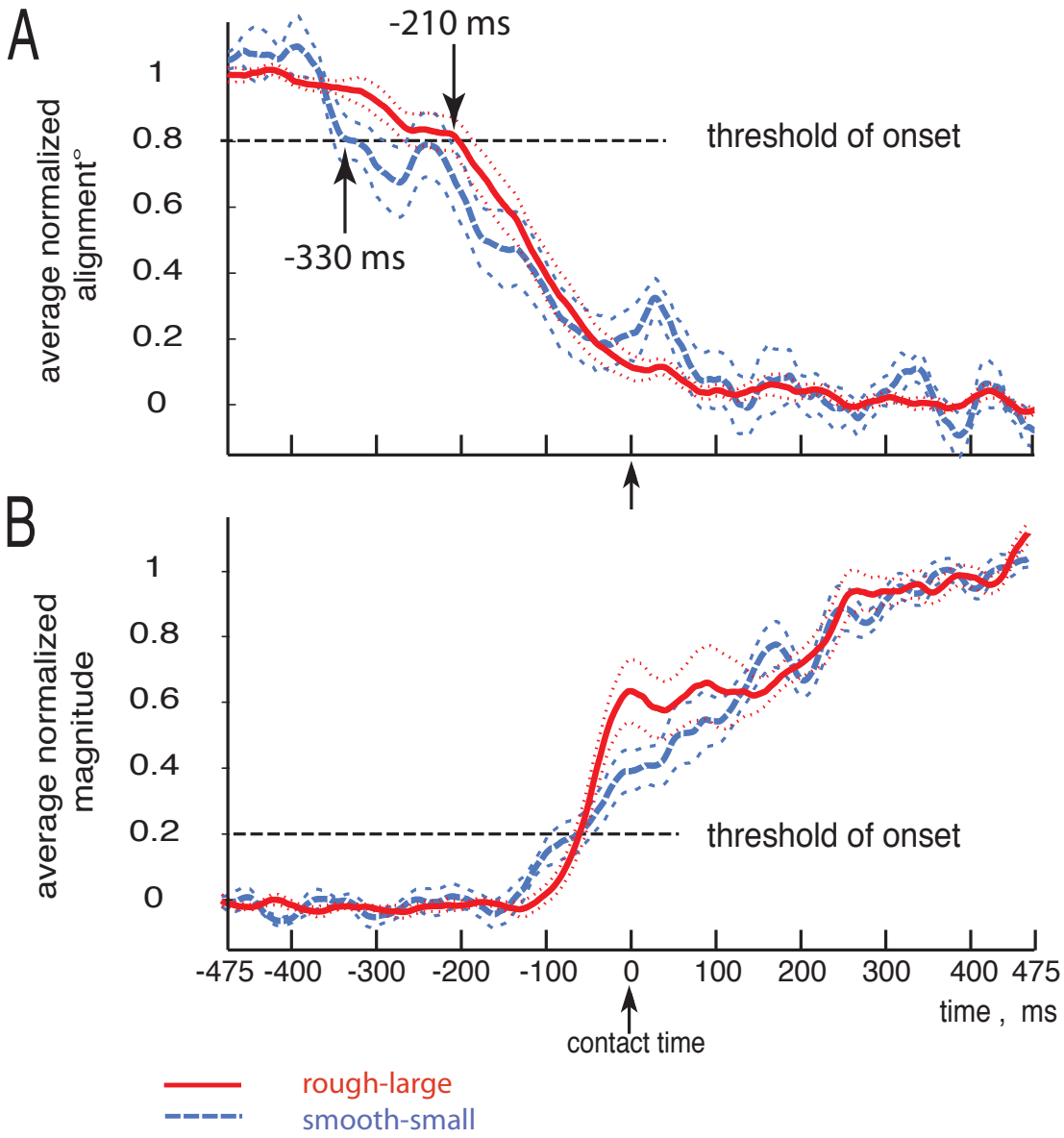

Figure 6.4: Empirical averaged coordination pattern alignment and magnitude. A. Normalized, smoothed coordination pattern alignment after been averaged across all trials separated by task difficulty i.e. smooth-small (dashed, blue) and rough-large (red). The threshold of the transition onset is marked with a horizontal line at 0.8, the coordination pattern for the smooth-small case starts the transition sooner than the coordination pattern for a rough-large case (-330 vs. -210 ms, respectively). The thinner dashed lines represent the coordination pattern alignment plus or minus their standard errors for each condition. B. Normalized, smoothed coordination pattern magnitude after having been averaged across all trials separated by task difficulty i.e. smooth-small (dashed, blue) and rough-large (in red). The threshold of the transition onset is marked with a dashed horizontal line at 0.2, the coordination pattern for smooth-small case starts the transition slightly sooner than the coordination pattern for a rough-large case.

figure 6.6A and figure 6.4A), although any thresholds greater than 10% show the same effect. Importantly, the change in muscle coordination pattern alignment is 90 % complete at the time of contact for both conditions. From figure 6.6 we find that the mean onset of the transition for the smooth-small case was 333 ms and for the rough-large case was 218 ms before contact. Calculating the onset of the transition trial by trial basis, and then averaging them for each condition we obtained mean transition onset values of 273 and 220 ms respectively for smooth-small and rough-large. After transformation to normality (using log10), an ANOVA test was performed with subject as a random effect to evaluate if the difference between transition times of onset was significant for different conditions, we obtained p= 0.015. Without transformation to normality p=0.019 was obtained. Thus both methods of calculating the onset find that the more difficult case has a statistically significant earlier onset.

For the transition in coordination pattern magnitude (figure 6.4B) we found that the smooth-small case begins 30 ms earlier than for the rough-large case. Recall that we did not use a regression analysis for the magnitude data. Moreover, while the sigmoidal function fits closely the trends in the evolution of the alignment of coordination patterns for both difficulties, the sigmoidal function is nevertheless better for the easier condition. The average coefficient of determination ± SE for the least squares fit to the 30 fitted trials was R^2= 0.79±0.037. When separating the data by task difficulty, the sigmoidal model fits the rough-large case significantly better (average R^2 of 0.9±0.02), than the smooth-small case (R^2= 0.7± 0.06), p=0.0008. The statistical significance of the average coefficient of determination was assessed using a 2-way ANOVA test with subject as a random effect. The data were transformed $\left(\frac{1}{\sqrt{-\ln R^2}}\right)$ to achieve a normal distribution to meet the assumptions of these parametric statistical tests given that correlation coefficients

exhibit floor and ceiling effects. Lilliefors tests were used to evaluate normality. For completeness we report that a p=0.0003 was obtained without transformation to normality.

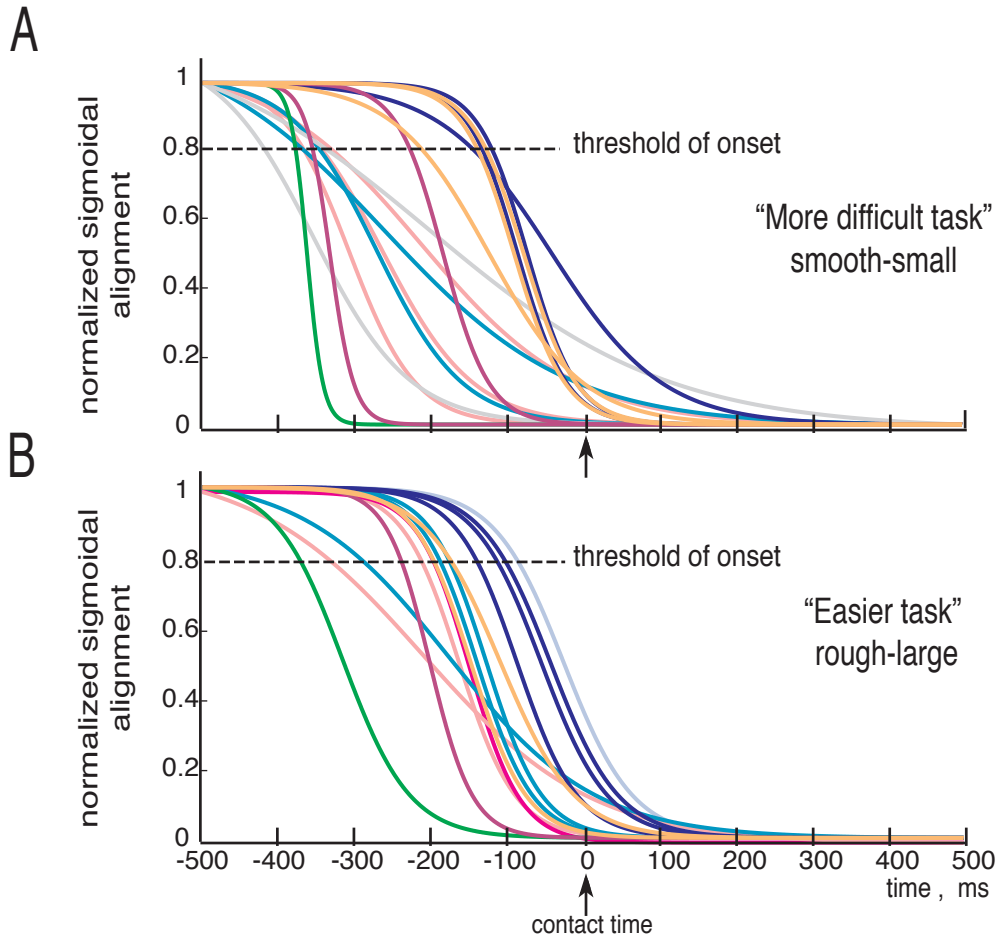

Figure 6.5: Individual fitted sigmoids, color-coded by subject. Normalized best fit sigmoids for each of the trial, when the surface of contact was: A smooth-small or B rough-large. We find that the transition for the easier task occurs later than for the more difficult task (except for one subject).

In a subsequent analysis, we also computed the power spectral density of the residuals to the sigmoidal fit (to discard the frequency spectrum of the sigmoids and account only for the variability about the sigmoidal trend). We see clear differences when we plot the power spectral density (obtained via fft) of the residuals to the normalized sigmoids (figure 6.7). This shows in a quantitative way that the nature

of the variability about the sigmoidal trend differs across conditions, suggestive of more on-line regulation in the case of the more difficult task (see Discussion).

Figure 6.8A shows angular deviation from vertical of the initial fingertip force vector, ϕ, from +10 ms to +500 ms after contact. The plot shows the results from all trials for each condition. A two-way ANOVA test with subject as a random effect indicated that the angular error ϕ at +65 ms (figure 6.8B) and the average ϕ from 10ms to 500ms were significantly lower for the smooth-small case p=0.02 and p<0.0001 respectively. Lilliefors tests showed it was necessary to transform the ϕ data, and we used a log10 transformation. Without transformation the p-value was <0.001. We chose to analyze ϕ at +65 ms because it is a conservative threshold for any corrections of the force vector on the basis of sensory information at contact (see Discussion).

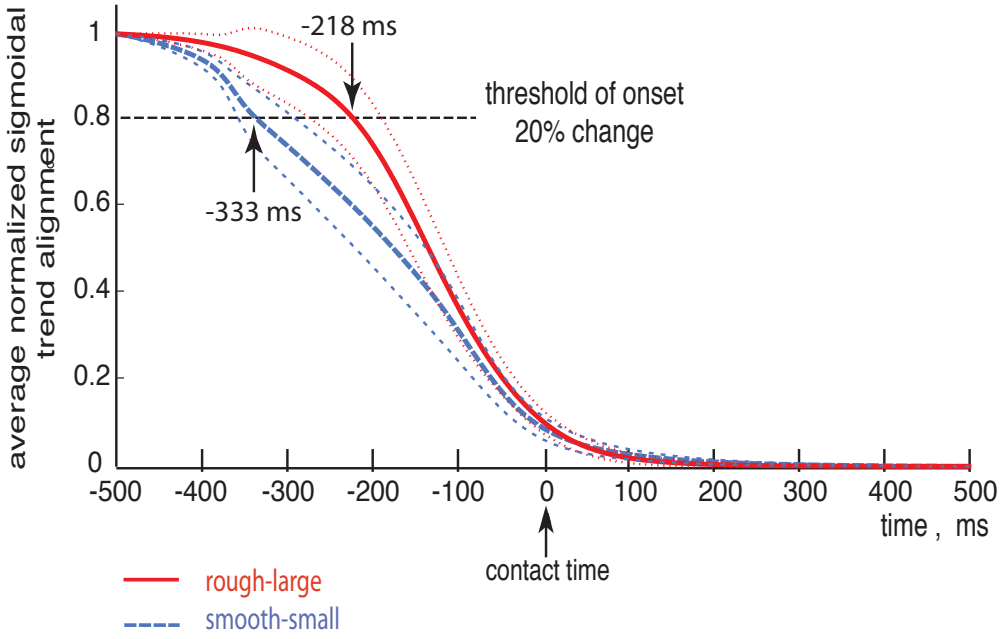

Figure 6.6: Normalized sigmoidal trend alignment. The coordination pattern alignment trend was obtained after having averaged the adjusted sigmoids from all the trials separated by task difficulty i.e. smooth-small (dashed, blue) and rough-large (red). The threshold of the transition onset is marked with a horizontal line at 0.8, the coordination pattern for the smooth-small case starts the transition sooner than the coordination pattern for the rough-large case (-333 vs. -218 ms, respectively). The thinner dashed lines represent the coordination pattern alignment trend plus or minus their standard errors for each condition.

6.5 Discussion

A central limitation of the neuromuscular system is its inability to switch between control strategies instantaneously or exactly due to unavoidable excitation-contraction dynamics and noise. Therefore, as described previously [156], the human nervous system implements an anticipatory, time-critical, and neurally demanding switch in control strategy to effectively perform the abrupt transition from the control of motion to the control of fingertip force. In addition, numerical simulations predicted that tuning the onset of the anticipatory transition to task difficulty is compatible with an optimal strategy that counteracts neuromuscular delays to reach the physical boundaries of performance [157]. We now show experimentally that changes in task difficulty change the temporal features of muscle coordination patterns during motion-to-force transitions with the fingertips. We characterized the temporal features of these anticipatory strategies in humans, and show that the adjustments in transition strategy in response to task difficulty are indeed compatible with that optimal strategy when performing this critical aspect of dexterous manipulation.

As in our prior work [156, 157], we first briefly discuss the relationships of our findings to past work on anticipatory motor control, and the limitations of our approach. Multiple studies have characterized anticipatory control in the limbs of humans and animals, (i) for smooth motion-force tasks for limbs subject to contacting (e.g., manipulanda experiments: [134, 84] and non-contacting (e.g., Coriolis force experiments: [84], and references therein) force fields, (ii) during abrupt postural perturbations associated with catching [86, 85], and (iii) animal studies of posture vs. ground-reaction force control [87] or posture vs. movement control [83]. Our results agree with their findings and conclusions to the extent that the nervous system can and does effectively anticipate changes in task con-

straints. In addition, the timing of the onset of anticipatory changes in EMG of ∼200 ms prior to changes in task constraints is similar to those found previously [86]. However, our work critically extends their and our prior work by being the first, to our knowledge, to record complete muscle coordination patterns from a musculoskeletal system (limb or finger) and full 3D force vectors to investigate whether and how the nervous system adapts the predictive transition of muscle coordination patterns to the difficulty of the task of switching abruptly from motion-to-force production. We believe the limitations of our approach do not challenge the validity of our conclusions. Although the use of a custom-molded thimble may appear unnatural, its potential drawbacks are outweighed by the benefits of a well-defined standardized contact condition across subjects (e.g., fingernail length and shape, skin dryness, friction conditions). This has allowed us to obtain high-fidelity biomechanical recordings that can be well approximated by and compared to computational models [153, 150, 156, 157]. In addition, the use of the thimble does approximate precision pinch acquisition of small or slippery objects. The results here also suggest future studies such as the effect of lengthy practice/learning on the neural strategy, or the inclusion of specialized populations such as microsurgeons or pianists.

The first type of adaptation to task difficulty we see is in the temporal advancement of the transition in coordination pattern vector. The advancement of the transition onset in the vector alignment, $\theta(\mathrm{t})$, of the coordination pattern for task difficulty is compatible with ideas of optimal control. Using both empirical and nonlinear regression analyses, we find that the onset of the transition for the more difficult task occurred sooner than for the easier task. The average onset value of -330 ms for the smooth-small case for the symmetrical moving average; and -210 ms for the rough-large compared with similar average onset times of -333

and -218 ms obtained from the adjusted sigmoids (figures 3, 4 and 6). Therefore, our results and conclusions regarding the temporal advancement of the transition do not depend entirely on the assumptions of sigmoids. When analyzing the sigmoid fits on a subject-by-subject basis (color coded in figure 6.5), we find that the transition for the easier task occurs later than for the more difficult task (except for one subject), in support of the reported mean values we present (figure 6.6). Advancing the onset of the transition can, at the very least, improve performance in the more difficult case because it allows more time to implement the coordination pattern for the production of well-directed force against a slippery surface. More formally, our recent published computational model of motion-to-force transitions [157] shows that advancing the onset of the transition in joint torques is an optimal adaptation to increased task difficulty because of the unavoidable latency of muscle activation-contraction dynamics ($\sim$36 ms [183]). We have also shown that in this experimental paradigm, muscle activation-contraction dynamics remains a rate-limiting process in transitioning to the muscle coordination pattern to produce well-directed isometric force upon contact [156]. Therefore, this advancement of the transition of coordination pattern vector alignment and vector magnitude can be considered an optimal adaptation to task difficulty.

The fact that the change in coordination pattern vector direction precedes the change of vector magnitude in all cases is also in agreement with our prior work where we show that such temporal disparity represents a nonlinear transformation of the coordination pattern [157]. (A linear transformation would involve simultaneous and proportional scaling of both the vector magnitude and direction.) We recently showed in computational simulations that such nonlinear transformations are a task-optimal way to compensate for neuromuscular delays and achieve accuracy of initial force direction [156].

The second important tuning in response to the difficulty of the task is that the transition of vector alignment, θ(t), of the coordination pattern for the easier task was more stereotypical than for the more difficult task, suggesting different planning and implementation of the neural control strategy (figure 6.7). We use the term stereotypical to mean that in one case (the easier task) the coordination pattern more closely follows the general trend of a sigmoid when transitioning between two states. This greater compatibility with the general trend of a sigmoid is quantified by the higher coefficients of determination. The high coefficients of determination for both task difficulties (>0.7 on average) show that the sigmoidal model fits both cases very well. That is, the change in coordination pattern vector alignment with time can be explained as the transition between asymptotes with a single inflexion point. However, the significantly higher average coefficient of determination for the transitions for the easier task (0.9 ± 0.02 vs. 0.70 ± 0.06) shows that a sigmoid model is an even better model for the easier task. Conversely, the transitions for the more difficult task contain features that cannot be captured as well by a stereotypical sigmoid function. This significant difference in the smoothness of the trends in the transition of coordination pattern alignment strongly suggests that there are differences in the planning and implementation of the neural control strategy across conditions. Namely, the easier task seems to be driven predominantly by a more stereotypical feed-forward and predictive motor command that more closely follows the general trend of a sigmoid; and is reminiscent of the kind that is well established in simple reach-to grasp tasks [92] and references therein). Conversely, the departure from a simple sigmoid suggests that the more difficult task is achieved with more adjustments to the motor command. In the subsequent spectral analysis, we see that the variability about the general trend of the sigmoid in the case of the more difficult task has significantly more

power over a greater frequency range. This greater complexity in the transition of coordination pattern alignment for the more difficult case is strongly indicative of more intense on-line regulation of the motor command. Given that in the motion prior to the transitions of coordination pattern alignment covers the 500 ms before contact, there is sufficient time to allow sensory-driven and internal model corrections at all sensory and cortical latencies e.g., from visuomotor to efferent-copy feedback loops [155, 157]; and reference therein) which may be up-regulated to perform the adjustments we see for the more difficult task. In fact, this is an additional benefit to advancing the onset of the transition in coordination pattern alignment for the more difficult case that our computational models did not take into account. Namely, if on-line corrections are up-regulated in the more difficult task, then initiating the transition sooner allows more time to complete on-line corrections in the presence of neuromuscular delays and noise. We have recently shown that such rich, task-optimal, on-line corrections are not only possible, but actually present in the control of accurate fingertip forces [152].

The directional accuracy of the fingertip force vector at contact provides a third line of evidence suggesting different planning and implementations of the neural control strategy with task difficulty. The misdirection of the fingertip force vector error at +65 ms (before any corrections in the force vector can be implemented on the basis of tactile sensory information at contact [17, 72, 33, 74, 71], is significantly lower for the more difficult task (figure 6.8). That is, a less stereotypical and less smooth transition of coordination pattern alignment results in a more accurate initial force direction against the low-friction surface; whereas a more stereotypical and smoother transition of coordination pattern alignment results in a less accurate initial force direction against the high-friction surface. In short, the up-regulation of the sensorimotor corrections of the transition of coordination

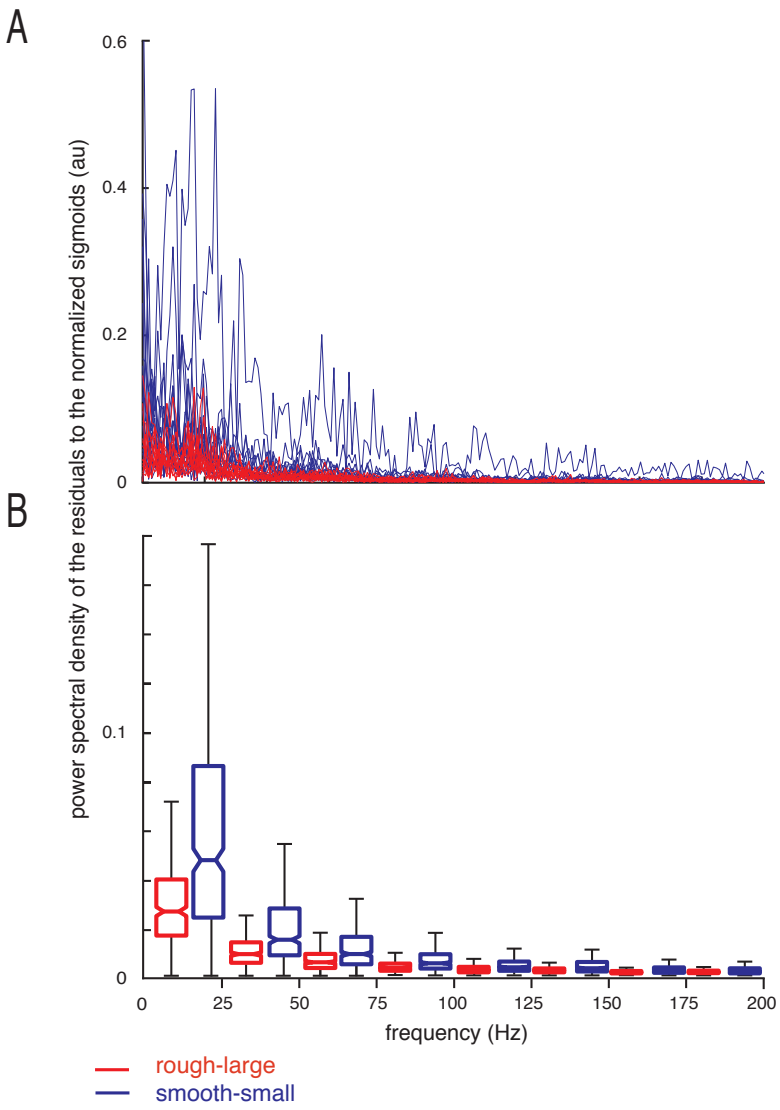

Figure 6.7: Power spectral density of the residuals to the normalized sigmoids. After removing the general trend of a sigmoid, the alignment of the muscle coordination pattern shows significantly more power over a greater frequency range for the more difficult task (blue). A. Fast Fourier transform from 0 to 200 Hz. B. Box plots of average power in bins 25 Hz wide. Non-parametric comparison of medians $\pm$ notches (standard errors) quantifies that the nature of the variability about the sigmoidal trend differs across conditions for frequencies $<$100 Hz where power is non-negligible.

pattern alignment has the functional consequence of improving the accuracy of the force task. This idea of on-line corrections resulting in higher EMG variability and improved performance is compatible with our prior work [152, 151]. We refrain from commenting further on the details of force production beyond +65 ms after contact for several reasons. Firstly, the focus of this work is to explore the trends in muscle coordination during the motion-to-force transition, which saturates and is 90% complete before contact. Secondly, as stated above, any changes in force magnitude and direction beyond +65 ms can be attributed to a large number of possible voluntary and involuntary mechanismsand are thus best studied under specifically designed conditions as in, for example, [153, 152].

How can we interpret this up-regulation in the context of control theory and neuromuscular control? We specifically mean that the more difficult task (smooth-small) displays greater online corrections (i.e., departure from the sigmoidal trend and variability at higher frequencies) in response to variability and disturbances arising from the constraints of the task and noise in the nervous system. We explicitly designed our experiment around two different short-duration tapping tasks, one with tighter constraints on motion and force accuracy than the other. Therefore, optimal control theory would require that the nervous system pre-compute (i.e., learn) control laws and gains tuned to each task (for a review of control theory in the context of neuromuscular control please see [151]. Importantly, for noisy systems such as the sensorimotor system, there is a trade-off between accuracy and sensitivity to noise because tasks that require higher accuracy need to reject perturbations more aggressively. This is exactly what we see in our results. Performing the task with tighter constraints (i.e., on the final position of the fingertip and accuracy of the initial fingertip force) will naturally exhibit more variability than the task with more relaxed constraints because the perturbation-rejection

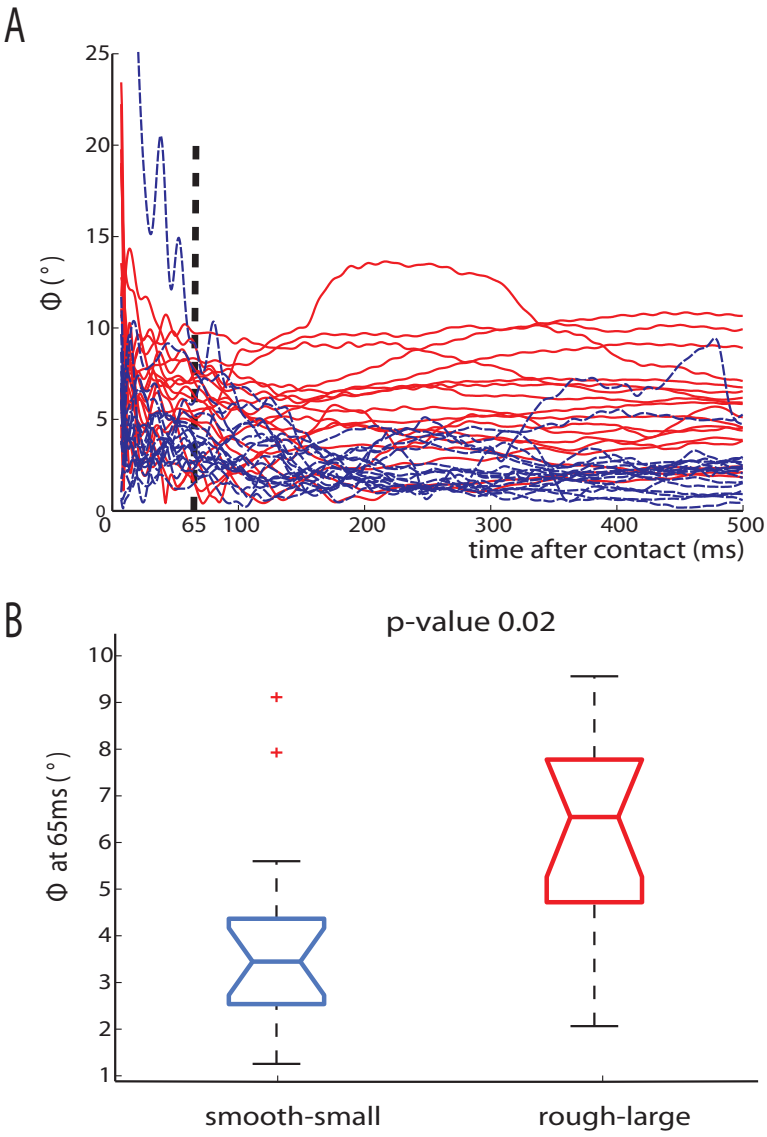

Figure 6.8: Deviation of the fingertip force vector after contact. A Deviation angle of force vector from vertical, ϕ, from all trials for the two conditions: smooth-small (dashed, blue) and rough-large (red). The first 10 ms were excluded for all analyses. The force direction appears to deviate more for the rough-large condition than for the smooth-small condition. B Comparison of the deviation angle at 65ms after contact between smooth-small and rough-large condition. The angle of deviation at 65ms is significantly higher for the rough-large than for the smooth-small condition (p=0.02).

gains need to be higher. In fact, our results provide new critical evidence at the level of muscle commands of real consequences of endogenous noise to sensorimotor control of movement.

Equally importantly, these results showing effective on-line corrections critically modify the common view that grasp acquisition is universally a memory-driven, feed-forward phenomenon [92] and references therein). Surely, the predictive nature of grasp acquisition is undeniable as seen by the onset of the transition in muscle coordination patterns prior to fingertip contactand which in other work is seen as pre-shaping of the fingertips and predictable grip forces [92]. However, our results reveal a previously unseen layer of low-level control at the level of muscle coordination: the up-regulation of on-line corrections to the motor command underlying the predictive trend. These results are compatible with, and add to the significance of, early reports of kinematic adjustments during rapid finger motions [16]. The specific mechanisms for these on-line corrections remain unclear, however, so future work is called for.

This work also allows us to articulate clear paths to improve our understanding of the neural control of dexterous manipulation. For example, the main features of this anticipatory strategy can be explained by deterministic models [156, 157] as an optimal adaptation to neuromuscular time-delays, with no need to consider optimizing for robustness to noise/uncertainties. However, our findings indicating greater variability in the motor command for the more difficult task compel us to consider the extent to which up-regulation of on-line corrections are indeed driven by a need to establish robustness to noise/uncertainties. In addition, our results oblige us to develop computational models and experimental paradigms to systematically interrogate the nervous system to identify the specific sensory and/or feedback and/or efference copy mechanisms responsible for the context-dependent

up-regulation of on-line corrections used to improve performanceand more rigorously establish whether and how optimality principles apply to the control of fingertip forces to enable dexterous manipulation. Lastly, future work is needed to expand the current thinking attributing grasp acquisition to purely feed-forward processes to establish a context-dependent continuum of control strategies. In summary, on the basis of our results and our prior work, we conclude that these three adaptations to task difficulty are all compatible with an optimal strategy to counteract neuromuscular delays to enable this fundamental feature of dexterous manipulation: making rapid contact with the object to produce well-directed forces.

CHAPTER 7

CONCLUSIONS AND FUTURE OUTLOOK

Advances in science have been driven by advances in technology. Nowdays we are able to use methodologies that were impossible some decades ago. For example, the ability to image inside a live brain with micrometer and more recently nanometer resolution, to record neural activity from multiple cells simultaneously and to create genetically engineered mice. These and other tools allow us to design experiments to decode human body function and develope therapies to improve human health. Using cutting edge technology, this dissertation provides a better understanding of the brain focusing on immediate effects of microhemorrhages.

We studied small hemorrhages which were induced in the brain arterioles of rodents using non-linear laser ablation to rupture the wall vessel and 2PEF to simultaneously visualize the creation of hemorrhage and characterize the region of injury. The use of animal models allowed for the induction of multiple brain microhemorrhages and the testing of drugs to reveal pharmacological effects on hemorrhage size. We investigated the use of Tissue Plasminogen Activator (tPA) and Dabigatran Etexilate (DE) in cases where patients had or are at risk for developing hemorrhagic strokes. tPA is the only drug available to dissolve blood clots, while Dabigatran Etexilate (DE) is a blood thinner which is chronically administered to patients to help prevent thrombolytic strokes. Currently, the use of these drugs is limited by fear of possible hemorrhagic complications, however we found that neither tPA or DE administered in mice exacerbated brain hemorrhage size. Mice treated with warfarin or heparin, which are also blood thinners, developed larger brain hemorrhages. Even though, the negative effects of warfarin and heparin on hemorrhagic strokes have been previously discovered, this was the first time that their effects on the size of microhemorrhages have been shown. Heparin and

warfarin were used as positive controls for tPA and DE. The results obtained in the tPA and DE laser-induced microhemorrhage studies were confirmed using a collagenase model by our collaborators. Furthermore, in the case of DE, similar results were obtained with a clinical trial where fewer patients developed hemorrhages under DE therapy than patients under warfarin treatment.

These results, therefore, suggest a change in the protocol for treating patients at risk of stroke with a more generalized used of DE, and the judicious use of warfarin. This study also suggests that the next step for tPA should be a clinical trial of immediate administration of tPA to patients with symptoms of ischemic strokes even before ruling out hemorrhagic stroke. If, as in rodents, tPA does not have undesired effects on hemorrhages, then tPA would be able to save more lives when administered promptly.

We also characterized, on a cellular basis, the effects of a microhemorrhage on neuronal activity using calcium imaging and 2PEF. We compared individual amplitude responses to an external stimulus on neurons and neuropil before and after a microhemorrhage was induced on an arteriole. We monitored cells positioned between the edge of hemorrhage RBC core and 1000 μm away. In addition, we monitored the same cells at different times with respect to hemorrhage induction (immediately, 2hrs, 4hrs, 24hrs after). We found that the amplitude of cell responses with respect their baseline (before hemorrhage) depended on their distance from hemorrhage and the lapsed time between the hemorrhage induction and the recording of response. Responses from cells within 150 μm of the hemorrhage were notably reduced, with a third of the cells not responding at all. In contrast, cells that were more than 300 μm away from the hemorrhage presented an average amplitude similar to control experiments, where we did not induce a hemorrhage but recorded responses at the same time intervals. Amplitudes of cells

located between 150 and 300 μm were also decreased, but not to the extent of proximal cells. Comparing the amplitude of responses obtained at the different times after hemorrhage, we found that cells eventually recover, with proximal cells requiring longer to return to baseline response. This recovery occurred at 4hrs for cells between 150 and 300 μm and 24hrs for cells within 150 μm.

This dissertation shows for the first time the damage caused by a microhemorrhage and that it is reversible. Previous work has suggested a link between patients with microhemorrhages and cognitive dysfunction from clinical studies. Additionally, et. al. Rosidi [127] could not find damage to dendrite structure within a week of post-microhemorrhage observation. It appears that even though neuronal morphology is not affected by a microhemorrhage, functionality gets disturbed temporarily and only in the most proximal region (<300 μm).

To support the claim of non permanent damage to cells after a microhemorrhage, we performed TUNEL labeling on brain slices that had previously induced microhemorrhages to assess apoptosis; results do not show tunnel positive cells near the microhemorrhage. However a more robust ex-vivo study it is suggested. Another experiment to further confirm viability of cells in-vivo would be to use transgenic mouse line that expresses fluorescently labeled interneurons. Interneurons have been shown to be more sensitive to external insults.

Another study should also consider analyzing calcium responses from astrocytes to find out whether their response to stimulus after a hemorrhage changes or remains unaffected at all times, as suggested by a fairly constant Sulforhodamine 101 labeling before and after hemorrhage.

Clinically, people usually present microhemorrhages under different conditions than the ones analyzed in this study, frequently with advanced age. It is possible that the aged brain would employ longer recovery times or it may not recover

at all. There are other high risk factors associated with microhemorrhages such as hypertension, obesity, microangiopathy, etc, that should be included in future studies. Besides the cerebral cortex, microhemorrhages in humans have been found in other regions deep in the brain such as basal ganglia, thalamus, brain stem, and cerebellum. It would be important to investigate whether or not other regions are more sensitive to the effects of microhemorrhages possibly causing cognitive decline. Such study is currently beyond modern technology because 2PEF is not able to access deep brain structures due to scattering of laser light into the tissue. A more viable study is to induce multiple hemorrhages on cortex separated by about 300 μm and observe if cells still can recover or whether there is a cumulative effect.

Comparing amplitude responses on cell by cell basis to study the effects of microhemorrhage on neuronal function is recommended in studies aiming to detect very subtle changes. This is only practical after having assessed intact morphology.

This work provides details that may help to improve therapy for ischemic strokes in the brain and answers main questions on the effects of a single hemorrhage on neurons in a healthy brain; it provides future steps that need to be covered to discern the link between microhemorrhages and cognitive dysfunction.

Appendices

.1 Detailed Protocol for Calcium Dye Preparation

.1.1 Reagents

1 vial (50μg) of Oregon Green 488 BAPTA-1, AM (OGB) (06807, Invitrogen)

Artificial cerebrospinal fluid (ACSF) [79]

50μM solution of Sulforhodamine 101 (S7635, Sigma) in ACSF

Pluronic F-127 (P2443, Sigma)

Dimethyl Sulfoxide (DMSO) (472301, Sigma)

.1.2 Procedure

1. Dissolve 1 g of Pluronic F-127 in 5 ml of DMSO to make a 20% solution.

Notes: The solution dissolves slowly, it can be left overnight on a moving platform, or warmed up prior to mixing for 30min or until the Pluronic F-127 is completely dissolved.

2. Sterilize $\sim$0.5 ml of the Pluronic-DMSO solution, $\sim$0.5 ml of the sulforhodamine 101 solution and $\sim$0.5 ml of ACSF by passing each through a syringe-driven filter (SLGP033RS, Millipore). Place each of the solutions in sterile eppendrof tubes.

Notes: The 20% Pluronic-DMSO solution can be stored at $5°C$ and should be used within 3 days. The Sulforhodamine 101 solution can be stored at $-20°C$.

3. Ensure that all OGB is on the bottom of the vial by lightly tapping on it. Add 5 μl to the vial and centrifuge for at least 15 min or until pale yellow.

4. Add 25 μl each of the sterile sulforhodamine 101 and ACSF solutions to the vial, and centrifuge for 15 min.

Notes: The concentration of the sulforhodamine 101 solution in ACSF($\sim$50 μM) can be roughly adjusted depending of its brightness during imaging.

5. Tightly close the vial and cover it completely with parafilm (01852, SPI).

6. Place the vial on a vortexer for 10 min.

Notes: Use parafilm or tape to attach the vial to the vortexer if necessary.

7. Submerge vial inside a sonicator filled with water. Turn it on for 30 minutes.

8. Remove vial from sonicator, dry and remove parafilm.

9. Place the vial in centrifuge for 5 min to remove bubbles.

10. Cover it with aluminum foil and use immediately.

BIBLIOGRAPHY

[1] Adams, H. P., Del Zoppo, G., Alberts, M. J., Bhatt, D. L., Brass, L., Furlan, A., Grubb, R. L., Higashida, R. T., Jauch, E. C., Kidwell, C., and et al. Guidelines for the early management of adults with ischemic stroke. *Stroke: A Journal of Cerebral Circulation 38*, 5 (2007), 1655–1711.

[2] Aguilar, M., Hart, R., Kase, C., Freeman, W., Hoeben, B., García, R., Ansell, J., Mayer, S., Norrving, B., Rosand, J., et al. Treatment of warfarin-associated intracerebral hemorrhage: literature review and expert opinion. In *Mayo Clinic Proceedings* (2007), vol. 82, pp. 82–92.

[3] Alvarez, M., Sanchez, V., Rosato, S., Cherksey, B., Sugimori, M., Llinas, R., and Uchitel, O. Pharmacological characterization of the voltage-dependent ca2+ channels present in synaptosomes from rat and chicken central nervous system. *Journal of neurochemistry 64*, 6 (1995), 2544.

[4] Augustine, G., Charlton, M., and Smith, S. Calcium action in synaptic transmitter release. *Annual Reviews Neuroscience 10* (1987), 633–693.

[5] Bailey, E., McCulloch, J., Sudlow, C., and Wardlaw, J. Potential animal models of lacunar stroke. *Stroke 40*, 6 (2009), e451–e458.

[6] Barnes, G., and Froehlich, J. Anticoagulation: where we are and where we need to go. *Journal of thrombosis and thrombolysis 28*, 2 (2009), 220–223.

[7] Beaurepaire, E. Ultra-deep two-photon fluorescence excitation in turbid media. *Optics Communications 188*, 1-4 (2001), 25–29.

[8] Broderick, J., Brott, T., Duldner, J., Tomsick, T., and Huster, G. Volume of intracerebral hemorrhage. a powerful and easy-to-use predictor of 30-day mortality. *Stroke 24*, 7 (1993), 987–993.

[9] Brott, T., Broderick, J., Kothari, R., Barsan, W., Tomsick, T., Sauerbeck, L., Spilker, J., Duldner, J., and Khoury, J. Early hemorrhage growth in patients with intracerebral hemorrhage. *Stroke 28*, 1 (1997), 1–5.

[10] Bullock, R., Mendelow, A., Teasdale, G., and Graham, D. Intracranial haemorrhage induced at arterial pressure in the rat. part 1: De-

scription of technique, icp changes and neuropathological findings. *Neurological research 6*, 4 (1984), 184–188.

[11] Castillo, J., Dvalos, A., Alvarez-Sabn, J., Pumar, J. M., Leira, R., Silva, Y., Montaner, J., and Kase, C. S. Molecular signatures of brain injury after intracerebral hemorrhage. *Neurology 58*, 4 (2002), 624–629.

[12] Charpak, S., Mertz, J., Beaurepaire, E., Moreaux, L., and Delaney, K. Odor-evoked calcium signals in dendrites of rat mitral cells. *Proceedings of the National Academy of Sciences of the United States of America 98*, 3 (2001), 1230–1234.

[13] Chichkov, B. N., Momma, C., Nolte, S., Von Alvensleben, F., and Tnnermann, A. Femtosecond, picosecond and nanosecond laser ablation of solids. *Applied Physics A Materials Science Processing 63*, 2 (1996), 109–115.

[14] Chin, S. From multiphoton to tunnel ionization. *Advances in multi-photon processes and spectroscopy 16* (2004), 249–272.

[15] Cole, K. J. Age-related directional bias of fingertip force. *Experimental Brain Research 175*, 2 (2006), 285–291.

[16] Cole, K. J., and Abbs, J. H. Coordination of three-joint digit movements for rapid finger-thumb grasp. *Journal of Neurophysiology 55*, 6 (1986), 1407–1423.

[17] Cole, K. J., and Abbs, J. H. Grip force adjustments evoked by load force perturbations of a grasped object. *Journal of Neurophysiology 60*, 4 (1988), 1513–1522.

[18] Connolly, S. J., Ezekowitz, M. D., Yusuf, S., Eikelboom, J., Oldgren, J., Parekh, A., Pogue, J., Reilly, P. A., Themeles, E., Varrone, J., and et al. Dabigatran versus warfarin in patients with atrial fibrillation. *The New England Journal of Medicine 361*, 12 (2009), 1139–1151.

[19] Cordonnier, C. Brain microbleeds. *Practical Neurology 10*, 2 (2010), 94–100.

[20] Crowther, M. A., and Warkentin, T. E. Managing bleeding in anticoagulated patients with a focus on novel therapeutic agents. *Journal of thrombosis and haemostasis JTH 7 Suppl 1* (2009), 107–110.

[21] Cullen, K. M., Kcsi, Z., and Stone, J. Pericapillary haem-rich deposits: evidence for microhaemorrhages in aging human cerebral cortex. *Journal of cerebral blood flow and metabolism official journal of the International Society of Cerebral Blood Flow and Metabolism 25*, 12 (2005), 1656–1667.

[22] Darrow, V. C., Alvord, E. C., Mack, L. A., and Hodson, W. A. Histologic evolution of the reactions to hemorrhage in the premature human infants brain. a combined ultrasound and autopsy study and a comparison with the reaction in adults. *The American journal of pathology 130*, 1 (1988), 44–58.

[23] Del Bigio, M. R., Yan, H. J., Buist, R., and Peeling, J. Experimental intracerebral hemorrhage in rats. magnetic resonance imaging and histopathological correlates. *Stroke: A Journal of Cerebral Circulation 27*, 12 (1996), 2312–2319; discussion 2319–2320.

[24] Denk, W., and Svoboda, K. Photon upmanship: Techreview why multiphoton imaging is more than a gimmick. *Neuron 18*, 3 (1997), 351–357.

[25] Denk, W., Yuste, R., Svoboda, K., and Tank, D. W. Imaging calcium dynamics in dendritic spines. *Current Opinion in Neurobiology 6*, 3 (1996), 372–378.

[26] Di Nisio, M., Middeldorp, S., and B
"uller, H. Direct thrombin inhibitors. *New England Journal of Medicine 353*, 10 (2005), 1028–1040.

[27] Dichgans, M., Holtmannspotter, M., Herzog, J., Peters, N., Bergmann, M., and Yousry, T. Cerebral microbleeds in cadasil. *Stroke 33*, 1 (2002), 67–71.

[28] Ding, S., Wang, T., Cui, W., and Haydon, P. G. Photothrombosis ischemia stimulates a sustained astrocytic ca2+ signaling in vivo. *Glia 57*, 7 (2009), 767–776.

[29] DiPolo, R., and Beaugé, L. The calcium pump and sodium-calcium exchange in squid axons. *Annual review of physiology 45* (1983), 313–24.

[30] Dombeck, D. A., Graziano, M. S., and Tank, D. W. Functional clustering of neurons in motor cortex determined by cellular resolution imaging in awake behaving mice. *Journal of Neuroscience 29*, 44 (2009), 13751–13760.

[31] Dombeck, D. A., Harvey, C. D., Tian, L., Looger, L. L., and Tank, D. W. Functional imaging of hippocampal place cells at cellular resolution during virtual navigation. *Nature Neuroscience 13*, 11 (2010), 1433–1440.

[32] Eichhoff, G., Busche, M. A., and Garaschuk, O. In vivo calcium imaging of the aging and diseased brain. *European Journal of Nuclear Medicine and Molecular Imaging* (2008), 99–106.

[33] Eliasson, A., Forssberg, H., Ikuta, K., Apel, I., Westling, G., and Johansson, R. Development of human precision grip. *Experimental Brain Research 106*, 3 (1995), 425–433.

[34] Eriksson, B. I., Dahl, O. E., Rosencher, N., Kurth, A. A., Van Dijk, C. N., Frostick, S. P., Prins, M. H., Hettiarachchi, R., Hantel, S., Schnee, J., and et al. Dabigatranetexilate versus enoxaparin for prevention of venous thromboembolism after total hip replacement: a randomised, double-blind, non-inferiority trial. *Lance 370*, 9591 (2007), 949–56.

[35] Faber, T., Joerges, J., and Menzel, R. Associative learning modifies neural representations of odors in the insect brain. *Nature Neuroscience 2*, 1 (1999), 74–78.

[36] Fazekas, F., Kleinert, R., Roob, G., Kleinert, G., Kapeller, P., Schmidt, R., and Hartung, H. Histopathologic analysis of foci of signal loss on gradient-echo t2*-weighted mr images in patients with spontaneous intracerebral hemorrhage: evidence of microangiopathy-related microbleeds. *American journal of neuroradiology 20*, 4 (1999), 637–642.

[37] Felberg, R. A., Grotta, J. C., Shirzadi, A. L., Strong, R., Narayana, P., Hill-Felberg, S. J., and Aronowski, J. Cell death in experimental intracerebral hemorrhage: the black hole model of hemorrhagic damage. *Annals of Neurology 51*, 4 (2002), 517–524.

[38] Fiehler, J. Cerebral microbleeds: old leaks and new haemorrhages. *International journal of stroke official journal of the International Stroke Society 1*, 3 (2006), 122–130.

[39] Foerch, C., Arai, K., Jin, G., Park, K., Pallast, S., van Leyen, K., and Lo, E. Experimental model of warfarin-associated intracerebral hemorrhage. *Stroke 39*, 12 (2008), 3397–3404.

[40] Foerch, C., Arai, K., Van Cott, E. M., Van Leyen, K., and Lo, E. H. Rapid reversal of anticoagulation reduces hemorrhage volume in a mouse model of warfarin-associated intracerebral hemorrhage. *Journal of cerebral blood flow and metabolism official journal of the International Society of Cerebral Blood Flow and Metabolism 29*, 5 (2009), 1015–1021.

[41] Garaschuk, O., and Griesbeck, O. Monitoring calcium levels with genetically encoded indicators. In *Calcium Measurement Methods*, A. Verkhratsky and O. H. Petersen, Eds., vol. 43 of *Neuromethods*. Humana Press, 2010, pp. 101–117.

[42] Garaschuk, O., Milos, R.-I., Grienberger, C., Marandi, N., Adelsberger, H., and Konnerth, A. Optical monitoring of brain function in vivo: from neurons to networks. 385–396.

[43] Gbel, W., and Helmchen, F. In vivo calcium imaging of neural network function. *Physiology Bethesda Md 22*, 6 (2007), 358–365.

[44] Gerritsen, H., and De Grauw, C. Imaging of optically thick specimen using two-photon excitation microscopy. *Microscopy Research and Technique 47*, 3 (1999), 206–209.

[45] Giessel, A. J., and Sabatini, B. L. M1 muscarinic receptors boost synaptic potentials and calcium influx in dendritic spines by inhibiting postsynaptic sk channels. *Neuron 68*, 5 (2010), 936–947.

[46] Gold, G., Kovari, E., Herrmann, F., Canuto, A., Hof, P., Michel, J., Bouras, C., and Giannakopoulos, P. Cognitive consequences of thalamic, basal ganglia, and deep white matter lacunes in brain aging and dementia. *Stroke 36*, 6 (2005), 1184–1188.

[47] Gong, C., Boulis, N., Qian, J., Turner, D. E., Hoff, J. T., and Keep, R. F. Intracerebral hemorrhage-induced neuronal death. *Neurosurgery 48*, 4 (2001), 875–882; discussion 882–883.

[48] Gong, C., Hoff, J., and Keep, R. Acute inflammatory reaction following experimental intracerebral hemorrhage in rat. *Brain research 871*, 1 (2000), 57–65.

[49] Gong, Y., Tian, H., Xi, G., Keep, R., Hoff, J., and Hua, Y. Systemic zinc protoporphyrin administration reduces intracerebral hemorrhage-induced brain injury. *Brain Edema XIII* (2006), 232–236.

[50] Grammas, P., Ottman, T., Reimann-Philipp, U., Larabee, J., and Weigel, P. H. Injured brain endothelial cells release neurotoxic thrombin. *Journal of Alzheimers disease JAD 6*, 3 (2004), 275–281.

[51] Greenberg, D., Houweling, A., and Kerr, J. Population imaging of ongoing neuronal activity in the visual cortex of awake rats. *Nature neuroscience 11*, 7 (2008), 749–751.

[52] Grynkiewicz, G., Poenie, M., Tsien, A. N. D., and A, R. Y. new generation of calcium indicators with greatly improved fluorescence properties. *The Journal of Biological Chemistry 260*, 6 (1985), 3440–3450.

[53] Guo, H., Barrett, T., Zhong, Z., Fernndez, J., Griffin, J., Freeman, R., and Zlokovic, B. Protein s blocks the extrinsic apoptotic cascade in tissue plasminogen activator/n-methyl d-aspartate-treated neurons via tyro3-akt-fkhrl1 signaling pathway. *Molecular Neurodegeneration 6* (2011), 1–12.

[54] Hall, N. C., Packard, B. A., Hall, C. L., De Courten-Myers, G., and Wagner, K. R. Protein oxidation and enzyme susceptibility in white and gray matter with in vitro oxidative stress: relevance to brain injury from intracerebral hemorrhage. *Cellular and molecular biology NoisyleGrand France 46*, 3 (2000), 673–683.

[55] Hanyu, H., Tanaka, Y., Shimizu, S., Takasaki, M., and Abe, K. Cerebral microbleeds in alzheimers disease. *Journal of Neurology 250*, 12 (2003), 1496–1497.

[56] Hasan, M. T., Friedrich, R. W., Euler, T., Larkum, M. E., Giese, G., Both, M., Duebel, J., Waters, J., Bujard, H., Griesbeck, O., and et al. Functional fluorescent ca2+ indicator proteins in transgenic mice under tet control. *PLoS Biology 2*, 6 (2004), e163.

[57] He, Y., Wan, S., Hua, Y., Keep, R. F., and Xi, G. Autophagy after experimental intracerebral hemorrhage. *Journal of cerebral blood flow and metabolism official journal of the International Society of Cerebral Blood Flow and Metabolism 28*, 5 (2008), 897–905.

[58] Heider, B., Nathanson, J., Isacoff, E., Callaway, E., and Siegel, R. Two-photon imaging of calcium in virally transfected striate cortical neurons of behaving monkey. *PloS one 5*, 11 (2010), e13829.

[59] Helmchen, F., and Denk, W. Deep tissue two-photon microscopy. *Nature Methods 2*, 12 (2005), 932–940.

[60] Helmchen, F., Svoboda, K., Denk, W., and Tank, D. W. In vivo dendritic calcium dynamics in deep-layer cortical pyramidal neurons. *Nature Neuroscience 2*, 11 (1999), 989–996.

[61] Heuser, J. E., Reese, T. S., Dennis, M. J., Jan, Y., Jan, L., and Evans, L. Synaptic vesicle exocytosis captured by quick freezing and correlated with quantal transmitter release. *The Journal of Cell Biology 81*, 2 (1979), 275–300.

[62] Hickenbottom, S. L., Grotta, J. C., Strong, R., Denner, L. A., and Aronowski, J. Nuclear factor-kappab and cell death after experimental intracerebral hemorrhage in rats. *Stroke: A Journal of Cerebral Circulation 30*, 11 (1999), 2472–2477.

[63] Hires, S. A., Tian, L., and Looger, L. L. Reporting neural activity with genetically encoded calcium indicators. *Brain cell biology 36*, 1-4 (2008), 69–86.

[64] Hogan, N. The mechanics of multi-joint posture and movement control. *Biological cybernetics 52*, 5 (1985), 315–331.

[65] Holtmaat, A., Bonhoeffer, T., Chow, D., Chuckowree, J., De Paola, V., Hofer, S., Hubener, M., Keck, T., Knott, G., Lee, W., et al. Long-term, high-resolution imaging in the mouse neocortex through a chronic cranial window. *Nature protocols 4*, 8 (2009), 1128–1144.

[66] Hopt, A., and Neher, E. Highly nonlinear photodamage in two-photon fluorescence microscopy. *Biophysical Journal 80*, 4 (2001), 2029–2036.

[67] Huang, F.-P., Xi, G., Keep, R. F., Hua, Y., Nemoianu, A., and Hoff, J. T. Brain edema after experimental intracerebral hemorrhage: role of hemoglobin degradation products. *Journal Of Neurosurgery 96*, 2 (2002), 287–293.

[68] Iida, S., Baumbach, G., Lavoie, J., Faraci, F., Sigmund, C., and Heistad, D. Spontaneous stroke in a genetic model of hypertension in mice. *Stroke 36*, 6 (2005), 1253–1258.

[69] Illanes, S., Zhou, W., Heiland, S., Markus, Z., and Veltkamp, R. Kinetics of hematoma expansion in murine warfarin-associated intracerebral hemorrhage. *Brain research 1320* (2010), 135–142.

[70] Jang, I. K., Gold, H. K., Ziskind, A. A., Fallon, J. T., Holt, R. E., Leinbach, R. C., May, J. W., and Collen, D. Differential sensitivity of erythrocyte-rich and platelet-rich arterial thrombi to lysis with recombinant tissue-type plasminogen activator. a possible explanation for resistance to coronary thrombolysis. *Circulation 79*, 4 (1989), 920–928.

[71] Johansson, R., and Birznieks, I. First spikes in ensembles of human tactile afferents code complex spatial fingertip events. *Nature Neuroscience 7*, 2 (2004), 170–177.

[72] Johansson, R., and Westling, G. Roles of glabrous skin receptors and sensorimotor memory in automatic control of precision grip when lifting rougher or more slippery objects. *Experimental Brain Research 56*, 3 (1984), 550–564.

[73] Joutel, A. Pathogenesis of cadasil. *BioEssays 33*, 1 (2011), 73–80.

[74] Kandel, E., Schwartz, J., and Jessell, T. *Principles of neural science*. McGraw-Hill, Health Professions Division, 2000.

[75] Kass, G. E., and Orrenius, S. Calcium signaling and cytotoxicity. *Environmental Health Perspectives 107*, Suppl 1 (1999), 25–35.

[76] Kazui, S., Naritomi, H., Yamamoto, H., Sawada, T., and Yamaguchi, T. Enlargement of spontaneous intracerebral hemorrhage: incidence and time course. *Stroke 27*, 10 (1996), 1783–1787.

[77] Keep, R. F., Xiang, J., Ennis, S. R., Andjelkovic, A., Hua, Y., Xi, G., and Hoff, J. T. Blood-brain barrier function in intracerebral hemorrhage. *Acta Neurochirurgica Supplement 105* (2008), 73–77.

[78] Kerr, J. N. D., Greenberg, D., and Helmchen, F. Imaging input and output of neocortical networks in vivo. *SciencesNew York 102*, 39 (2005), 14063–14068.

[79] Kleinfeld, D., and Delaney, K. Distributed representation of vibrissa movement in the upper layers of somatosensory cortex revealed with voltage-sensitive dyes. *The Journal of Comparative Neurology 375*, 1 (1996), 89–108.

[80] Koennecke, H.-C. Cerebral microbleeds on mri: prevalence, associations, and potential clinical implications. *Neurology 66*, 2 (2006), 165–171.

[81] Koester, H. J., Baur, D., Uhl, R., and Hell, S. W. Ca2+ fluorescence imaging with pico-and femtosecond two-photon excitation: signal and photodamage. *Biophysical Journal 77*, 4 (1999), 2226–2236.

[82] Kovari, E., Gold, G., Herrmann, F., Canuto, A., Hof, P., Michel, J., Bouras, C., and Giannakopoulos, P. Cortical microinfarcts and demyelination significantly affect cognition in brain aging. *Stroke 35*, 2 (2004), 410–414.

[83] Kurtzer, I., Herter, T., and Scott, S. Random change in cortical load representation suggests distinct control of posture and movement. *Nature neuroscience 8*, 4 (2005), 498–504.

[84] Lackner JR, D. P. Motor control and learning in altered dynamic environments. *Current Opinion in Neurobiology 15*, 6 (2005), 653–659.

[85] Lacquaniti, F. Internal models of limb geometry in the control of hand compliance. *Journal of Neuroscience 12*, 5 (1992), 1750–1762.

[86] Lacquaniti, F., and Maioli, C. The role of preparation in tuning anticipatory and reflex responses during catching. *Journal of Neuroscience 9*, 1 (1989), 134–148.

[87] Lacquaniti, F., and Maioli, C. Independent control of limb position and contact forces in cat posture. *Journal of Neurophysiology 72*, 4 (1994), 1476–1495.

[88] Lee, C. J., Badhwar, G., and Ansell, J. E. Oral iia inhibitors. *Hematologyoncology clinics of North America 24*, 4 (2010), 739–753.

[89] Liem, M., Lesnik Oberstein, S., Haan, J., van der Neut, I., Ferrari, M., van Buchem, M., Middelkoop, H., and van der Grond, J. Mri correlates of cognitive decline in cadasil. *Neurology 72*, 2 (2009), 143–148.

[90] Lisman, T., Adelmeijer, J., Nieuwenhuis, H. K., and De Groot, P. G. Enhancement of fibrinolytic potential in vitro by anticoagulant drugs targeting activated factor x, but not by those inhibiting thrombin or tissue

factor. *Blood coagulation fibrinolysis an international journal in haemostasis and thrombosis 14*, 6 (2003), 557–562.

[91] Lorrain, J., Millet, L., Lechaire, I., Lochot, S., Ferrari, P., Visconte, C., Sainte-Marie, M., Lunven, C., Berry, C. N., Schaeffer, P., and et al. Antithrombotic properties of ssr182289a, a new, orally active thrombin inhibitor. *The Journal of pharmacology and experimental therapeutics 304*, 2 (2003), 567–574.

[92] Lukos, J., Ansuini, C., and Santello, M. Anticipatory control of grasping: independence of sensorimotor memories for kinematics and. *Journal of Neuroscience 28*, 48 (2008), 12765–74.

[93] Luzzati, F., De Marchis, S., Fasolo, A., and Peretto, P. Neurogenesis in the caudate nucleus of the adult rabbit. *Journal of Neuroscience 26*, 2 (2006), 609–621.

[94] MacLellan, C. L., Silasi, G., Auriat, A. M., and Colbourne, F. Rodent models of intracerebral hemorrhage. *Stroke: A Journal of Cerebral Circulation 41*, 10 Suppl (2010), S95–S98.

[95] Mank, M., Santos, A., Direnberger, S., Mrsic-Flogel, T. D., Hofer, S. B., Stein, V., Hendel, T., Reiff, D. F., Levelt, C., Borst, A., Bonhoeffer, T., Hubener, M., and Griesbeck, O. A genetically encoded calcium indicator for chronic in vivo two-photon imaging. *Nature methods 5*, 9 (2008), 805–11.

[96] Mao, T., OConnor, D. H., Scheuss, V., Nakai, J., and Svoboda, K. Characterization and subcellular targeting of gcamp-type genetically-encoded calcium indicators. *PLoS ONE 3*, 3 (2008), e1796.

[97] Masuda, T., Maki, M., Hara, K., Yasuhara, T., Matsukawa, N., Yu, S., Bae, E. C., Tajiri, N., Chheda, S. H., Solomita, M. A., and et al. Peri-hemorrhagic degeneration accompanies stereotaxic collagenase-mediated cortical hemorrhage in mouse. *Brain Research 1355* (2010), 228–239.

[98] Matsushita, K., Meng, W., Wang, X., Asahi, M., Asahi, K., Moskowitz, M. A., and Lo, E. H. Evidence for apoptosis after intercerebral hemorrhage in rat striatum. *Journal of cerebral blood flow and metabolism official journal of the International Society of Cerebral Blood Flow and Metabolism 20*, 2 (2000), 396–404.

[99] Mayer, S., Sacco, R., Shi, T., and Mohr, J. Neurologic deterioration in noncomatose patients with supratentorial intracerebral hemorrhage. *Neurology 44*, 8 (1994), 1379.

[100] Mayne, M., Ni, W., Yan, H., Xue, M., Johnston, J., Del Bigio, M., Peeling, J., Power, C., Feuerstein, G., Ho, S., et al. Antisense oligodeoxynucleotide inhibition of tumor necrosis factor-{{alpha}} expression is neuroprotective after intracerebral hemorrhage editorial comment. *Stroke 32*, 1 (2001), 240–248.

[101] McAuley, G., Schrag, M., Barnes, S., Obenaus, A., Dickson, A., and Kirsch, W. In vivo iron quantification in collagenase-induced microbleeds in rat brain. *Magnetic Resonance in Medicine*.

[102] Murray, V., Norrving, B., Sandercock, P. A., Terent, A., Wardlaw, J. M., and Wester, P. The molecular basis of thrombolysis and its clinical application in stroke. *Journal of Internal Medicine 267*, 2 (2010), 191–208.

[103] Nakata, Y., Shiga, K., Yoshikawa, K., Mizuno, T., Mori, S., Yamada, K., and Nakajima, K. Subclinical brain hemorrhages in alzheimers disease: evaluation by magnetic resonance t2*-weighted images. *Annals Of The New York Academy Of Sciences 977* (2002), 169–172.

[104] Nath, F., Jenkins, A., Mendelow, A., Graham, D., and Teasdale, G. Early hemodynamic changes in experimental intracerebral hemorrhage. *Journal of neurosurgery 65*, 5 (1986), 697–703.

[105] Neame, S. J., Rubin, L. L., and Philpott, K. L. Blocking cytochrome c activity within intact neurons inhibits apoptosis. *The Journal of Cell Biology 142*, 6 (1998), 1583–1593.

[106] Niell, C. M., and Smith, S. J. Functional imaging reveals rapid development of visual response properties in the zebrafish tectum. *Neuron 45*, 6 (2005), 941–951.

[107] Nielsen, V. G., Cohen, B. M., and Cohen, E. Effects of coagulation factor deficiency on plasma coagulation kinetics determined via thrombelastography: critical roles of fibrinogen and factors ii, vii, x and xii. *Acta Anaesthesiologica Scandinavica 49*, 2 (2005), 222–231.

[108] Nimmerjahn, A., Kirchhoff, F., Kerr, J., and Helmchen, F. Sulforhodamine 101 as a specific marker of astroglia in the neocortex in vivo. *Nature methods 1*, 1 (2004), 31–37.

[109] Nishimura, N., Rosidi, N., Iadecola, C., and Schaffer, C. Limitations of collateral flow after occlusion of a single cortical penetrating arteriole. *Journal of Cerebral Blood Flow & Metabolism* (2010).

[110] Nishimura, N., Schaffer, C. B., Friedman, B., Tsai, P. S., Lyden, P. D., and Kleinfeld, D. Targeted insult to subsurface cortical blood vessels using ultrashort laser pulses: three models of stroke. *Nature Methods 3*, 2 (2006), 99–108.

[111] Offenbacher, H., Fazekas, F., Schmidt, R., Koch, M., Fazekas, G., and Kapeller, P. Mri of cerebral abnormalities concomitant with primary intracerebral hematomas. *American journal of neuroradiology 17*, 3 (1996), 573–578.

[112] Oheim, M., Beaurepaire, E., Chaigneau, E., Mertz, J., and Charpak, S. Two-photon microscopy in brain tissue: parameters influencing the imaging depth. *Journal of Neuroscience Methods 111*, 1 (2001), 29–37.

[113] Ohki, K., Chung, S., Chng, Y. H., Kara, P., and Reid, R. C. Functional imaging with cellular resolution reveals precise micro-architecture in visual cortex. *Nature 433*, 7026 (2005), 597–603.

[114] Paredes, R. M., Etzler, J. C., Watts, L. T., Zheng, W., and Lechleiter, J. D. Chemical calcium indicators. *Methods San Diego Calif 46*, 3 (2008), 143–151.

[115] Patterson, G. H., and Piston, D. W. Photobleaching in two-photon excitation microscopy. *Biophysical Journal 78*, 4 (2000), 2159–2162.

[116] Perzborn, E., Strassburger, J., Wilmen, A., Pohlmann, J., Roehrig, S., Schlemmer, K.-H., and Straub, A. In vitro and in vivo studies of the novel antithrombotic agent bay 59-7939–an oral, direct factor xa inhibitor. *Journal of thrombosis and haemostasis JTH 3*, 3 (2005), 514–521.

[117] Pettersen, J., Sathiyamoorthy, G., Gao, F., Szilagyi, G., Nadkarni, N., St George-Hyslop, P., Rogaeva, E., and Black, S.

Microbleed topography, leukoaraiosis, and cognition in probable alzheimer disease from the sunnybrook dementia study. *Archives of neurology 65*, 6 (2008), 790–795.

[118] Poenie, M. Measurement of intracellular calcium with fluorescent calcium indicators. *Neuromethods 20*, 1–39.

[119] Qiao, L., Ni, J., Mao, Z., Wang, C., and Cheng, Y. Two-color two-photon excitation of indole using a femtosecond laser regenerative amplifier. *Optics Communications 282*, 5 (2009), 1056–1061.

[120] Qiu, C., Cotch, M. F., Sigurdsson, S., Jonsson, P. V., Jonsdottir, M. K., Sveinbjrnsdottir, S., Eiriksdottir, G., Klein, R., Harris, T. B., Van Buchem, M. A., and et al. Cerebral microbleeds, retinopathy, and dementia: the ages-reykjavik study. *Neurology 75*, 24 (2010), 2221–2228.

[121] Qureshi, A., Mendelow, A., and Hanley, D. Intracerebral haemorrhage. *The Lancet 373*, 9675 (2009), 1632–1644.

[122] Qureshi, A., Tuhrim, S., Broderick, J., Batjer, H., Hondo, H., and Hanley, D. Spontaneous intracerebral hemorrhage. *New England Journal of Medicine 344*, 19 (2001), 1450–1460.

[123] Rodgers, R. P., and Levin, J. A critical reappraisal of the bleeding time. *Seminars In Thrombosis And Hemostasis 16*, 1 (1990), 1–20.

[124] Rojas, M., Navas, J., and Rector, D. Evoked response potential markers for anesthetic and behavioral states. *American Journal of Physiology-Regulatory, Integrative and Comparative Physiology 291*, 1 (2006), R189–R196.

[125] Roob, G., Schmidt, R., Kapeller, P., Lechner, A., Hartung, H., and Fazekas, F. Mri evidence of past cerebral microbleeds in a healthy elderly population. *Neurology 52*, 5 (1999), 991.

[126] Rosenberg, G., Mun-Bryce, S., Wesley, M., and Kornfeld, M. Collagenase-induced intracerebral hemorrhage in rats. *Stroke 21*, 5 (1990), 801–807.

[127] Rosidi, N., Olbricht, William, L., Nishimura, N., and Schaffer, C. B. Cortical microhemorrhages cause local inflammation but do not trigger dendrite pathology. *In review* (2011).

[128] Roy, S. S., and Hajnczky, G. Calcium, mitochondria and apoptosis studied by fluorescence measurements. *Methods San Diego Calif 46*, 3 (2008), 213–223.

[129] Schaffer, C., Nishimura, N., Glezer, E., Kim, A., and Mazur, E. Dynamics of femtosecond laser-induced breakdown in water from femtoseconds to microseconds. *Optics Express 10*, 3 (2002), 196–203.

[130] Schaffer, C. B., Friedman, B., Nishimura, N., Schroeder, L. F., Tsai, P. S., Ebner, F. F., Lyden, P. D., and Kleinfeld, D. Two-photon imaging of cortical surface microvessels reveals a robust redistribution in blood flow after vascular occlusion. *PLoS Biology 4*, 2 (2006), e22.

[131] Scheid, R., Preul, C., Gruber, O., Wiggins, C., and Von Cramon, D. Diffuse axonal injury associated with chronic traumatic brain injury: evidence from t2*-weighted gradient-echo imaging at 3 t. *American journal of neuroradiology 24*, 6 (2003), 1049–1056.

[132] Schrag, M., McAuley, G., Pomakian, J., Jiffry, A., Tung, S., Mueller, C., Vinters, H., Haacke, E., Holshouser, B., Kido, D., et al. Correlation of hypointensities in susceptibility-weighted images to tissue histology in dementia patients with cerebral amyloid angiopathy: a postmortem mri study. *Acta neuropathologica 119*, 3 (2010), 291–302.

[133] Schulman, S., Kearon, C., Kakkar, A., Mismetti, P., Schellong, S., Eriksson, H., Baanstra, D., Schnee, J., and Goldhaber, S. Dabigatran versus warfarin in the treatment of acute venous thromboembolism. *New England Journal of Medicine 361*, 24 (2009), 2342–2352.

[134] Shadmehr, R., and Mussa-Ivaldi, F. Adaptive representation of dynamics during learning of a motor task. *Journal of Neuroscience 14*, 5.2 (1994), 3208–3224.

[135] Sheng, Z. H., Westenbroek, R. E., and Catterall, W. A. Physical link and functional coupling of presynaptic calcium channels and the synaptic vesicle docking/fusion machinery. *Journal of Bioenergetics and Biomembranes 30*, 4 (1998), 335–345.

[136] Shih, A. Y., Droscoll, J. D., Drew, P. J., Friedman, B., Lyden, P. D., and Kleinfeld, D. One vessel, one stroke - occlusion of a single cortical penetrating venule is more severe than occlusion of a penetrating arteriole. program no. 799.1. In *2010 Neuroscience Meeting Planner, San Diego, CA* (2010), vol. 40 Anual Meeting, Society for Neuroscience.

[137] Simard, A. R., Soulet, D., Gowing, G., Julien, J.-P., and Rivest, S. Bone marrow-derived microglia play a critical role in restricting senile plaque formation in alzheimers disease. *Neuron 49*, 4 (2006), 489–502.

[138] Soeller, C., and Cannell, M. B. Two-photon microscopy: imaging in scattering samples and three-dimensionally resolved flash photolysis. *Microscopy Research and Technique 47*, 3 (1999), 182–195.

[139] Steiner, T., Rosand, J., and Diringer, M. Intracerebral hemorrhage associated with oral anticoagulant therapy: current practices and unresolved questions. *Stroke 37*, 1 (2006), 256–262.

[140] Stosiek, C., Garaschuk, O., Holthoff, K., and Konnerth, A. In vivo two-photon calcium imaging of neuronal networks. *Proceedings of the National Academy of Sciences of the United States of America 100*, 12 (2003), 7319–7324.

[141] SUTTNER, D., and DENNERY, P. Reversal of ho-1 related cytoprotection with increased expression is due to reactive iron. *The FASEB journal 13*, 13 (1999), 1800–1809.

[142] Svoboda, K., Denk, W., Kleinfeld, D., and Tank, D. W. In vivo dendritic calcium dynamics in neocortical pyramidal neurons. *Nature 385*, 6612 (1997), 161–165.

[143] Szyszka, P., Demmler, C., Oemisch, M., Sommer, L., Biergans, S., Birnbach, B., Silbering, A., and CG., G. Mind the gap: Olfactory trace conditioning in honeybees. *The Journal of Neuroscience 31*, 20 (2011), 7229–7239.

[144] Takahashi, A., Camacho, P., Lechleiter, J. D., and Herman, B. Measurement of intracellular calcium. *Physiological Reviews 79*, 4 (1999), 1089–1125.

[145] Tang, J., Liu, J., Zhou, C., Alexander, J., Nanda, A., Granger, D., and Zhang, J. Mmp-9 deficiency enhances collagenase-induced intrac-

erebral hemorrhage and brain injury in mutant mice. *Journal of Cerebral Blood Flow & Metabolism 24*, 10 (2004), 1133–1145.

[146] Tsai, P., Nishimura, N., Yoder, E., Dolnick, E., White, G. A., and Kleinfeld, D. Principles, design, and construction of a two photon laser scanning microscope for in vitro and in vivo brain imaging. *In vivo optical imaging of brain function* (2002), 113–171.

[147] Tsien, R. Y. A non-disruptive technique for loading calcium buffers and indicators into cells. *Nature 290*, 5806 (1981), 527–528.

[148] Tsushima, Y., Aoki, J., and Endo, K. Brain microhemorrhages detected on t2*-weighted gradient-echo mr images. *American journal of neuroradiology 24*, 1 (2003), 88–96.

[149] Tuor, U., and Farrar, J. Pial vessel caliber and cerebral blood flow during hemorrhage and hypercapnia in the rabbit. *American Journal of Physiology-Heart and Circulatory Physiology 247*, 1 (1984), H40–H51.

[150] Valero-Cuevas, F. J. Predictive modulation of muscle coordination pattern magnitude scales fingertip force magnitude over the voluntary range. *Journal of Neurophysiology 83*, 3 (2000), 1469–1479.

[151] Valero-Cuevas, F. J., Hoffmann, H., Kurse, M. U., Kutch, J. J., and Theodorou, E. A. Computational models for neuromuscular function. *IEEE Reviews in Biomedical Engineering 2*, October (2009), 110–135.

[152] Valero-Cuevas, F. J., Venkadesan, M., and Todorov, E. Structured variability of muscle activations supports the minimal intervention principle of motor control. *Journal of Neurophysiology 102*, 1 (2009), 59–68.

[153] Valero-Cuevas, F. J., Zajac, F. E., and Burgar, C. G. Large index-fingertip forces are produced by subject-independent patterns of muscle excitation. *Journal of Biomechanics 31*, 8 (1998), 693–703.

[154] Van Ryn, J., Stangier, J., Haertter, S., Liesenfeld, K., Wienen, W., Feuring, M., and Clemens, A. Dabigatran etexilate–a novel, reversible, oral direct thrombin inhibitor: Interpretation of coagulation assays and reversal of anticoagulant activity. *Thromb Haemost 103*, 6 (2010), 1116–1127.

[155] Venkadesan, M., Guckenheimer, J., and Valero-Cuevas, F. J. Manipulating the edge of instability. *Journal of Biomechanics 40*, 8 (2007), 1653–1661.

[156] Venkadesan, M., and Valero-Cuevas, F. J. Neural control of motion-to-force transitions with the fingertip. *Journal of Neuroscience 28*, 6 (2008), 1366–1373.

[157] Venkadesan, M., and Valero-Cuevas, F. J. Effects of neuromuscular lags on controlling contact transitions. *Philosophical Transactions of the Royal Society - Series A: Mathematical, Physical and Engineering Sciences 367*, 1891 (2009), 1163–1179.

[158] Vermeer, S., Longstreth Jr, W., and Koudstaal, P. Silent brain infarcts: a systematic review. *The Lancet Neurology 6*, 7 (2007), 611–619.

[159] Vogel, A., Noack, J., Httman, G., and Paltauf, G. Mechanisms of femtosecond laser nanosurgery of cells and tissues. *Applied Physics B 81*, 8 (2005), 1015–1047.

[160] Von Kummer, R., and Back, T. *Magnetic resonance imaging in ischemic stroke*. 2006.

[161] Wagner, K. Modeling intracerebal hemorrhage. *Stroke 38*, 2 (2007), 753–758.

[162] Wagner, K., Knight, J., Packard, B., et al. Rapid nuclear factor kappa-b activation and cytokine and heme oxygenase-1 gene expression in edematous white matter after porcine intracerebral hemorrhage. In *Abstracts of the International Stroke Conference* (2001), vol. 32, Am Heart Assoc, p. 327.

[163] Wagner, K. R., Sharp, F. R., Ardizzone, T. D., Lu, A., and Clark, J. F. Heme and iron metabolism: role in cerebral hemorrhage. *Journal of cerebral blood flow and metabolism official journal of the International Society of Cerebral Blood Flow and Metabolism 23*, 6 (2003), 629–652.

[164] Wake, H., Moorhouse, A. J., Jinno, S., Kohsaka, S., and Nabekura, J. Resting microglia directly monitor the functional state of synapses in vivo and determine the fate of ischemic terminals. *Journal of Neuroscience 29*, 13 (2009), 3974–3980.

[165] Wakisaka, Y., Chu, Y., Miller, J. D., Rosenberg, G. A., and Heistad, D. D. Spontaneous intracerebral hemorrhage during acute and chronic hypertension in mice. *Journal of cerebral blood flow and metabolism official journal of the International Society of Cerebral Blood Flow and Metabolism 30*, 1 (2010), 56–69.

[166] Wakisaka, Y., Miller, J., Chu, Y., Baumbach, G., Wilson, S., Faraci, F., Sigmund, C., and Heistad, D. Oxidative stress through activation of nad (p) h oxidase in hypertensive mice with spontaneous intracranial hemorrhage. *Journal of Cerebral Blood Flow & Metabolism 28*, 6 (2008), 1175–1185.

[167] Wallace, D. J., Meyer ZumAltenBorgloh, S., Astori, S., Yang, Y., Bausen, M., Kgler, S., Palmer, A. E., Tsien, R. Y., Sprengel, R., Kerr, J. N. D., and et al. Single-spike detection in vitro and in vivo with a genetic ca2+ sensor. *Nature Methods 5*, 9 (2008), 797–804.

[168] Wang, J., and Dor, S. Inflammation after intracerebral hemorrhage. *Journal of cerebral blood flow and metabolism official journal of the International Society of Cerebral Blood Flow and Metabolism 27*, 5 (2007), 894–908.

[169] Wang, X., Lee, S., Arai, K., Lee, S., Tsuji, K., Rebeck, G., and Lo, E. Lipoprotein receptor–mediated induction of matrix metalloproteinase by tissue plasminogen activator. *Nature medicine 9*, 10 (2003), 1313–1317.

[170] Watson, B., Dietrich, W., Busto, R., Wachtel, M., and Ginsberg, M. Induction of reproducible brain infarction by photochemically initiated thrombosis. *Annals of neurology 17*, 5 (1985), 497–504.

[171] Werring, D., Frazer, D., Coward, L., Losseff, N., Watt, H., Cipolotti, L., Brown, M., and Jager, H. Cognitive dysfunction in patients with cerebral microbleeds on t2*-weighted gradient-echo mri. *Brain 127*, 10 (2004), 2265–2275.

[172] Whitney, D. E. Historical perspective and state of the art in robot force control. *The International Journal of Robotics Research 6*, 1 (1987), 3–14.

[173] Wienen, W., Stassen, J.-M., Priepke, H., Ries, U., and Hauel, N. Effects of the direct thrombin inhibitor dabigatran and its orally active prodrug, dabigatranetexilate, on thrombus formation and bleeding time in rats. *Thrombosis and haemostasis 98*, 2 (2007), 333–338.

[174] Wu, J., Hua, Y., Keep, R., Schallert, T., Hoff, J., and Xi, G. Oxidative brain injury from extravasated erythrocytes after intracerebral hemorrhage. *Brain research 953*, 1-2 (2002), 45–52.

[175] Xi, G., Keep, R. F., and Hoff, J. T. Mechanisms of brain injury after intracerebral haemorrhage. *The Lancet 5*, 1 (2006), 53–63.

[176] Xue, M., and Del Bigio, M. R. Intracerebral injection of autologous whole blood in rats: time course of inflammation and cell death. *Neuroscience Letters 283*, 3 (2000), 230–232.

[177] Yakushiji, Y., Nishiyama, M., Yakushiji, S., Hirotsu, T., Uchino, A., Nakajima, J., Eriguchi, M., Nanri, Y., Hara, M., Horikawa, E., et al. Brain microbleeds and global cognitive function in adults without neurological disorder. *Stroke 39*, 12 (2008), 3323–3328.

[178] Yasaka, M., Minematsu, K., Naritomi, H., Sakata, T., and Yamaguchi, T. Predisposing factors for enlargement of intracerebral hemorrhage in patients treated with warfarin. *Thrombosis and Haemostasis 89*, 2 (2003), 278–283.

[179] Yepes, M., Sandkvist, M., Moore, E. G., Bugge, T. H., Strickland, D. K., and Lawrence, D. A. Tissue-type plasminogen activator induces opening of the blood-brain barrier via the ldl receptor-related protein. *Journal of Clinical Investigation 112*, 10 (2003), 1533–1540.

[180] Yongjun, J., Ning, W., Juehua, Z., Tingting, L., Zhaoyao, C., Gelin, X., and Xinfeng, L. Effects of brain-derived neurotrophic factor on local inflammation in experimental stroke of rat. *Mediators of Inflammation 2010* (2011).

[181] Yuste, R., and Denk, W. Dendritic spines as basic functional units of neuronal integration. *Nature 375*, 6533 (1995), 682–684.

[182] Yuste, R., Majewska, A., Cash, S. S., and Denk, W. Mechanisms of calcium influx into hippocampal spines: heterogeneity among spines, coincidence detection by nmda receptors, and optical quantal analysis. *Journal of Neuroscience 19*, 6 (1999), 1976–1987.

[183] Zajac, F. Muscle and tendon: properties, models, scaling, and application to biomechanics and motor control. *Critical reviews in biomedical engineering 17*, 4 (1989), 359.

[184] Zecca, L., Youdim, M., Riederer, P., Connor, J., and Crichton, R. Iron, brain ageing and neurodegenerative disorders. *Nature Reviews Neuroscience 5*, 11 (2004), 863–873.

[185] Zhang, S., and Murphy, T. Imaging the impact of cortical microcirculation on synaptic structure and sensory-evoked hemodynamic responses in vivo. *PLoS Biology 5*, 5 (2007), e119.

[186] Zipfel, W. R., Williams, R. M., and Webb, W. W. Nonlinear magic: multiphoton microscopy in the biosciences. *Nature Biotechnology 21*, 11 (2003), 1369–1377.

[187] Zivin, J. A., Fisher, M., DeGirolami, U., Hemenway, C. C., and Stashak, J. A. Tissue plasminogen activator reduces neurological damage after cerebral embolism. *Science 230*, 4731 (1985), 1289–1292.